MULTI-FUNCTIONAL EPOXY/GRAPHENE NANOPLATELET COMPOSITES

A thesis submitted to the University of Manchester

for the degree of Doctor of Philosophy

in the Faculty of Engineering and Physical Sciences

2016

Gaoxiang Cao

School of Materials

CONTENTS

List of Tables 6
List of Figures 7
Abstract 13
Declaration 14
Copyright statement 15
Acknowledgement 16

CHAPTER 1 INTRODUCTION AND AIMS 17
References 19

CHAPTER 2 LITERATURE REVIEW 23
2.1 Discovery and Properties of Graphene 23
2.1.1 Synthesis of Graphene 25
2.1.2 Graphene Oxide 26
2.1.3 Chemical Functionalization of Graphene 28
2.2 Characterisation of Graphene 31
2.2.1 Raman Spectroscopy 31
2.2.2 Atomic Force Microscopy 34
2.2.3 X-ray Diffraction 34
2.2.4 Transmission Electron Microscopy 35
2.3 Preparation Methods of Polymer/Graphene Composites 37
2.3.1 *In-situ* Polymerization 37
2.3.2 Solution Compounding 37
2.3.3 Melt Blending 38
2.3.4 Combination of Mixing Techniques 39
2.4 Properties of Polymer/Graphene Composites 39
2.4.1 Mechanical Properties 39
2.4.2 Electrical Percolation Threshold and Conductivity 41
2.4.3 Thermal Conductivity 45
2.4.4 Gas Barrier Properties 47
2.4.5 Water Uptake of Polymer Matrix Composites 48

References 51
CHAPTER 3 Experimental 61
3.1 Materials 61
3.2 Preparation Methods 62
3.3 Preparation of Composites 63
3.4 Characterization of Filler and Epoxy Nano-composites 65
3.4.1 Optical Microscopy 65
3.4.2 Atomic Force Microscopy and Sample Preparation 65
3.4.3 Raman Spectroscopy 65
3.4.4 Thermal Gravimetric Analysis (TGA) 67
3.4.5 Scanning Electron Microscopy 68
3.4.6 X-ray Diffraction 68
3.4.7 Dynamic Mechanical Thermal Analysis 69
3.4.8 Tensile Testing 71
3.4.9 Water Uptake Measurement 71
3.4.10 Thermal Conductivity Measurement 72
3.4.11 Oscillating Shear and Rotational Shear Rheometer 74
3.4.12 Impedance Spectroscopy 74
References 78
CHAPTER 4 Structural characteriSation of M5 and M25 epoxy composites 80
4.1 Introduction 80
4.2 Raman Characterisation of GNP 80
4.3 AFM Characterisation of GNP 81
4.4 Basic Characterisations of GNP/epoxy Composites Produced by Shear Mixing 82
4.4.1 Rheology of Epoxy-GNP Dispersions 82
4.4.2 XRD Characterization of GNP and Composites 85
4.4.3 Optical Characterization of the Composites 86
4.4.4 SEM Characterization of GNP and Composites 92

4.4.5 Polarized Raman Spectroscopy Measurement of GNP Orientation in Epoxy Matrix 95

4.5 Comparative Study of Composites Prepared by Three-roll Milling and Solvent-assisted Mixing 98

4.6 Summary 101

References 102

CHAPTER 5 Mechanical properties of GNP composites 104

5.1 Introduction 104

5.2 *In-situ* Raman Spectroscopy to Evaluate the Degree of Stress Transfer 104

5.3 Dynamic Mechanical Thermal Analysis 106

5.4 Tensile Testing 110

5.5 Theoretical Models *vs* Experimental Data 116

5.6 Summary 118

References 119

CHAPTER 6 Thermal and electrical properties of GNP composites 122

6.1 Introduction 122

6.2 Thermal Conductivity of M5 and M25/epoxy Composites 122

6.3 Modelling of Thermal Conductivity 125

6.4 Impedance Testing of GNP/epoxy Composites 128

6.5 Electrical Percolation Threshold 131

6.6 The Equivalent Circuit Model of Composites 135

6.7 Summary 139

References 140

CHAPTER 7 WATER UPTAKE OF GNP/EPOXY COMPOSITES AND ITS EFFECTS ON MECHANICAL AND ELECTRICAL PROPERTIES 143

7.1 Introduction 143

7.2 Water Uptake Measurements of Epoxy Composites 143

7.3 Effects of Water Uptake on Thermal Conductivity of Composites 147

7.4 Effects of Water Uptake on Thermal Mechanical Behaviour of Composites 148

7.5 Effects of Water Uptake on Electrical Conductivity of Composites 151

7.6 Effects of Water Uptake on Mechanical Properties 153

7.7 Summary 155

References 155

CHAPTER 8 Conclusions and Future Work 157

8.1 Conclusions 157

8.2 Suggestions for Future Work 160

41,631 Words

LIST OF TABLES

Table 2.1 Electrical percolation threshold (ϕc) and other electrical parameters of graphene/polymer composite from the literature.....43

Table 3.1 Data sheet of GNP.....61

Table 4.1 ImageJ analysis of the ratio of the number of white to black pixels in the dark masked optical images in Figure 4.7.....88

Table 5.1 Summary of DMTA peak position and peak height of Tan δ. 110

Table 5.2 Summary of composite mechanical properties. 115

Table 6.1 Summary of electrical parameters of all samples.....135

Table 6.2 The corresponding parameters from the simulating results. 138

Table 7.1 Parameters of Water diffusion.....144

Table 7.2 Water absorption of neat epoxy and M25 composites. 146

Table 7.3 Dynamic mechanical thermal parameters for water saturated and water desorbed neat epoxy and nano-composites.....150

Table 7.4 Specific conductivity of M25 composite samples.....152

Table 7.5 Mechanical properties of epoxy and composites after water absorption.....154

LIST OF FIGURES

Figure 2.1 Structure of graphene and other carbon materials [1].....23

Figure 2.2 Electronic band structure of graphene and bulk graphite [3-4]. 24

Figure 2.3 Several methods of large scale production of graphene, which allow a wide range in terms of size, quality and price for any particular applications. Novoselov et al. [30].....26

Figure 2.4 Models of the basal plane of GO (a) [33] and (b) [31]. (c) Digital pictures of as-prepared graphite oxide dispersed in water and other organic solvents using sonication [32].....27

Figure 2.5 Several reactive intermediates of radicals, nitrenes, carbenes, and arynes used in graphene functionalization. These reactive species covalently modify graphene through free radical addition, CH insertion, or cycloaddition reactions [51]. 28

Figure 2.6 Illustration of interaction between graphene fillers and APTS, and the incorporating process of modified-graphene nanoplatelets into the epoxy matrix. Wang X et al. [51].....29

Figure 2.7 The preparation process of p-CCG [38].....29

Figure 2.8 Schematic of noncovalent functionalization of graphene using polymers and small-molecule adsorbates. Adapted from [57]. 30

Figure 2.9 Typical Raman spectrum for graphene edge, showing the main Raman features, the D, G and G' bands [71].....31

Figure 2.10 The Raman spectra for various layers of graphene on quartz (a) and on a SiO_2 (300 nm)/Si substrate (b). The enlarged 2D band regions with the curve fitting are shown in panel (c) and (d) [74]. 32

Figure 2.11 (a) The 2D band of monolayer graphene at unstrained, 0.78% strain and with strain released. (b) The 2D band position shift versus applied strain for monolayer and tri-layer graphene [83]. 33

Figure 2.12 Thickness of graphene measured using AFM. Adapted from [85-86]. 34

Figure 2.13 XRD intensity profiles of graphite, GO and individually exfoliated graphene sheets [87]. 35

Figure 2.14 Graphene thickness analysis. High-resolution TEM images of the folded graphene edge, where the dark lines indicate the number of layers of (a) 3, (b) 28 and 3-5 (f). 36

Figure 2.15 The incorporation process of exfoliated graphene sheets (FGS) into polymer by (a) solvent technique and (b) melt blend technique. Adapted from [87]..38

Figure 2.16 Combination of various preparation methods to disperse GNP into an epoxy matrix. [93].....39

Figure 2.17 Stress-strain curves for (a) solvent blended and (b) melt blended poly(ethylene oxide)/graphene composites [87]. (c) Tensile modulus of solvent blended or melt blended composites made of thermally reduced graphene oxide (TRG)/linear low density polyethylene (EG-8200) and TRG/ linear low density polyethylene grafted with maleic anhydride (EG-8200-MA) [94].....40

Figure 2.18 Young's modulus of poly(ethylene oxide)/graphene composites as a function of graphene volume fraction [87].....40

Figure 2.19 Specific conductivity of polystyrene composites filled with reduced graphene oxide functionalized by phenylisocyanate as function of filler volume fraction, and the power-law of conductivity above the percolation threshold ϕ_c [103]. 42

Figure 2.20 Thermal conductivity increment of epoxy-based composites. Graphitic fillers: graphitic micro particles (GMP), graphene nanoplatelet (GNP) exfoliated at 200 ^{o}C (GNP-200) and 800 ^{o}C (GNP-800), carbon black (CB), and purified single wall carbon nanotubes (SWNTs) [128].....46

Figure 2.21 Thermal conductivity of epoxy/graphene nanoplatelets (GNP) composite as a function of (a) GNP lateral dimension and loading (φ), (b) GNP grade (H_{15}, M_{15} and C_2) and φ [133].....47

Figure 2.22 Illustration of formation of a 'tortuous path' of platelets inhibiting diffusion of gases through a polymer composite (Nielson model). Adapted from [98]. 48

Figure 2.23 Water uptake behaviour of epoxy resin and nano-composites reinforced with CNTs [137].....49

Figure 3.1 Chemical structure of DGEBA (a) and the components in the hardener (b) [7]. 62

Figure 3.2 Digital images of the mould with 5 mm thick polytetrafluoroethylene plate between the two 5mm steel plates.....63

Figure 3.3 Diagram showing the energy level for Raman scattering, adapted from ref [10].....66

Figure 3.4 Bragg model of diffraction.....69

Figure 3.5 An impedance vector diagram. 75

Figure 3.6 Nyquist (a) and Bode plots (b) for a resistor and a capacitor connected in series, simulated by Zview software.....76

Figure 3.7 Nyquist and Bode plots for an ideal capacitor (C = 1μF) (a) and (b) the impedance of resistor and capacitor connected in parallel (R = 100Ω, C = 1μF), simulated using Zview software. 77

Figure 4.1 Raman spectroscopy of M5, M15 and M25 (a) obtained from experiment and (b) the data of grade M graphene nanoplatelets adapted from XG Sciences data sheet.....80

Figure 4.2 AFM images and height profiles of M5 (a) and M25 (b). The red dash lines in (b) and (d) are a guide to the eye. 81

Figure 4.3 The dependency of G' and G'' with strain amplitude as measured by oscillatory shear measurements for dispersions of M5/epoxy (a) and M25/epoxy (b). The experiments were conducted at room temperature and a fixed frequency of 1 rad/s.....83

Figure 4.4 Frequency sweep measurements conducted within LVR (γ = 0.2%), showing G' and G" vs. frequency for M5 (a) and M25 (b)/epoxy composites, and their complex viscosity (η*) of M5 (c) and M25 (d)/epoxy composites. 84

Figure 4.5 XRD patterns of GNP M25 (b), pure epoxy (a) and composite samples (b) with 2, 5 and 8 wt.% M25 graphene nanoplatelets loading. 85

Figure 4.6 Typical optical micrographs of the GNP/epoxy composite samples. (a) is of the uncured, liquid system where (c) is of the cured composite. (b) and d) are digitally processed versions of (a) and (c) respectively where a cut-off mask has been applied. Scale bar is 50 μm. (e) Raman spectrum one of the white regions in (c). 86

Figure 4.7 Typical dark masked optical images for uncured (a, c and e) and cured (b, d and f) M25/epoxy composites with 1 wt.% (a,b), 5 wt.% (c,d) and 8 wt.% (e,f). All of the images have the same scale bar 50 μm. 87

Figure 4.8 Applied mask of graphite/epoxy composites at different sample depths: top (a), middle (b) and bottom (c), ref [10]. 89

Figure 4.9 Typical optical images of M25/epoxy composites with loading of 1 wt.% (a, b), 5 wt.% (c, d) and 8 wt.% (e, f). Left images: Top side. Right images: Bottom side of the composites. 89

Figure 4.10 Optical images of micro voids within samples containing (a) 1wt.% and (b) 8wt.% M25 GNP. 90

Figure 4.11 SEM images of M5 (a), M15 (b) and M25 (c). Note the scale bars are different for clearer view. 92

Figure 4.12 SEM images of fracture surfaces of (a) pure epoxy, and M25/epoxy composites prepared by shear mixing with loadings of (b) 0.8 wt.%, (c) 2 wt.%, (d)5 wt.%, (e) 8 wt.%, and (f) an enlarged area of M25 GNP in the composite with 2 wt.% loading. 93

Figure 4.13 GNP interaction with matrix and aggregations in cross section areas of 1 wt.% (a, b), 5 wt.% (c, d) and 8 wt.% (e, f) epoxy/M25 composites prepared by shear mixing. 94

Figure 4.14 Schematic illustration of the geometry of the Raman spectroscopic analysis of the GNP/epoxy nano-composites with (b) the laser beam parallel to z, and (c) the laser beam parallel to x. (The double headed arrows in b and c indicate the axes of laser polarization). The black lines in the rectangle of c represent GNP flakes dispersed in the matrix. 96

Figure 4.15 (a,c) I_G (the intensity of the G band) variation with the laser beam parallel to the Z-axis as a function of the angle θZ. (b,d) I_G variation with the laser beam parallel to the X-axis as a function of the angle θX. Samples were prepared by shear mixing. 97

Figure 4.16 Fig (a,c) I_G variation with the laser beam parallel to the Z-axis as a function of the angle θ_Z. (b,d) I_G variation with the laser beam parallel to the X-axis as a function of the angle θ_X. Samples were prepared by three-roll milling with a 0.08 mm gap. 98

Figure 4.17 SEM images of (a) pure epoxy, and M25/epoxy composites prepared by solvent-assisted blending with loadings of (b) 0.8 wt.%, (c) 5 wt.%, (d) 8 wt.%. 99

Figure 4.18 SEM images of (a) pure epoxy, and M25/epoxy composites prepared by three-roll mill mixing with loadings of (b) 0.8 wt.%, (c)5 wt.%, (d) 7 wt.%. 100

Figure 4.19 Various GNP aggregate types found in composites. 101

Figure 5.1 The position shift of the 2D band with as a function of strain for the 1 wt.% (a) and 0.5 wt.% (b) epoxy/M25 nano-composites. The composites were loaded stepwise to 1 % strain follow by step-wise unloaded. 105

Figure 5.2 Storage modulus for M5 (a) and M25/epoxy (b) composites prepared by shear mixing, and M25/epoxy composites prepared by solvent-assisted mixing (c) and three-roll mill mixing (d). 107

Figure 5.3 Loss factor (tan δ) curve for M5 (a) and M25 (b) composites prepared by shear mixing, and M25 based composites fabricated by three-roll mil mixing (0.15mm roller gap) (c) and solvent-assisted blending (d). The loss factor (tan δ) profile (e) for M25/epoxy to show the peak height and peak width at half height. (f) Tan δ peaks as a function of filler loadings. 109

Figure 5.4 Typical stress-strain curves from: (a) epoxy/M5 composites produced by shear mixing, (b) epoxy/M25 composites produced by shear mixing, (c) epoxy/M25 composites produced by three-roll mill mixing, and (d) epoxy/M25 composites produced by solvent-assisted mixing. 112

Figure 5.5 Young's modulus as a function of filler loading for M5 and M25 epoxy composites prepared by various methods. 113

Figure 5.6 Tensile strength as a function of filler loading for M5 and M25 epoxy composites prepared by various methods. 114

Figure 5.7 Tensile Modulus of M5 and M25 epoxy composites: Comparison of Halpin-Tsai theoretical models with experimental data. 116

Figure 6.1 (a) M5 and M25/epoxy shear mixed composite conductivity as a function of GNP loadings and (b) thermal conductivity of M25/epoxy composites prepared by three different methods against GNP loadings. 124

Figure 6.2 Diagram of a GNP coated with a very thin interfacial boundary layer. 126

Figure 6.3 Comparison of experimental and modelling data of M5 (a) and M25 (b)/epoxy composites made by shear mixing. The dot and solid line represent experimental and modelling calculated data respectively. 127

Figure 6.4 Specific conductivity as a function of frequency for M5 (a) and M25 (b)epoxy composites at various GNP loadings. 129

Figure 6.5 Specific conductivity as a function of frequency for M25 epoxy composites fabricated by solvent-assisted mixing (a) and three-roll mill mixing at 0.15mm roller gap (b) and 0.08mm roller gap (c). 130

Figure 6.6 Semi log plot of the specific conductivity, σ, as a function of the filler loadings for M5 (a) and M25 (b) composites produced by shear mixing. The inset shows the fitting data used to fit percolation theory to the experimental results. 132

Figure 6.7 Semi log plot of the specific conductivity, σ, as a function of GNP loadings for the M25 composites produced by solvent-assisted mixing (a) and three-roll milling with 0.15 (b) and 0.08mm (c) roller gap. The inset shows the fitting data used. 134

Figure 6.8 The model and equivalent circuit model used for the GNP/epoxy composites.....135

Figure 6.9 The Nyquist plots and the simulated equivalent circuit for the GNP/epoxy composites prepared by shear mixing with different GNP contents. (a) 1 wt.%; (b) 3 wt.%; (c) 5 wt.%; (d) 7wt.% and (e) 8 wt.%. The points are the experiment data, and the solid line is from the equivalent circuit. 137

Figure 7.1 Water uptake of epoxy resin and nano-composites reinforced with M25 made by shear mixing. The lines are a guide for the eye. 144

Figure 7.2 Diffusion coefficient (a) and maximum water absorption (b) as function of GNP loadings for M25 composites. 145

Figure 7.3 Thermal conductivity of composites as function of GNP loadings with fitting results. 148

Figure 7.4 Storage modulus and loss factor of water desorbed (a, c) and water-saturated (b, d) samples versus temperature. 149

Figure 7.5 T_g of unaged, water saturated and water desorbed samples.....150

Figure 7.6 Specific conductivity of water-saturated and water-desorbed M25 composite samples. 152

Figure 7.7 Young's modulus (a), tensile strength (b) and elongation at break (c) as function of GNP loadings of unaged, water-saturated and water-desorbed M25 composite samples. 153

ABSTRACT

The University of Manchester

Gaoxiang Cao

Doctor of Philosophy

Multi-Functional Epoxy/Graphene Nanoplatelet Composites

2016

Graphene nanoplatelets (GNP) with thickness of 6 ~ 8 nm and lateral dimension of 5 μm (M5) and 25 μm (M25) have been used to prepare epoxy composites. Epoxy composites were fabricated initially by shear mixing to investigate the effects of filler type on the structure and properties of composites. The complex viscosity of GNP-epoxy mixture was found to increase by almost three orders of magnitude going from the neat epoxy to the 8 wt.% loading, leading to difficulties in their processing. Scanning electron microscopy of the composites showed that both fillers aggregated at high loadings with the M25 buckling more easily due to its larger diameter, which compromises its aspect ratio advantage over M5, resulting in only slightly better mechanical performance. Polarized Raman spectroscopy revealed that both M5 and M25 were randomly distributed in the epoxy matrix, After adding M5 and M25 fillers, the storage modulus increase with the filler loadings, however, the glass transition temperature (T_g) drops slightly after initial incorporation, then rises with further filler addition attributed to the pin effects of filler aggregations. In terms of electrical property, M25 has lower percolation (1 wt.%) than M5 composites due to its bigger aspect ratio, which enable M25 to form a conductive network more efficiently. Furthermore, M25 composites also have slightly better thermal and mechanical properties over that of M5 composites. However, the difference is not significant considering the aspect ratio of M25 is five times of that of M5. The reason is that the aggregation and buckling of M25 compromise its advantage over M5. Due to the better performance of M25 as filler, M25/epoxy composites were prepared by shear mixing, solvent compounding and three-roll mill. Samples made by solvent compounding display the lowest percolation threshold (0.5 wt.%), related to its relatively uniform dispersion of M25 in matrix, resulting in higher thermal conductivity and better mechanical properties. Water uptake in a water bath at 50 °C took 75 days to be saturated. Higher loaded samples have lower diffusion coefficient because of the barrier effects of GNP fillers, but have higher maximum water absorbed, which is owing to filler aggregation. Properties test of aged and unaged specimens show thermal conductivity of the aged was enhanced due to water's higher thermal conductivity than epoxy resin matrix, while electrical performance was compromised due to the swelling effects caused by absorbed water. The mechanical properties of aged samples also dropped slightly due to plasticization effects.

DECLARATION

No portion of the work referred to in the thesis has been submitted in support of an application for another degree or qualification of this or any other university or other institute of learning.

COPYRIGHT STATEMENT

i. The author of this thesis (including any appendices and/or schedules to this thesis) owns certain copyright or related rights in it (the "Copyright") and s/he has given The University of Manchester certain rights to use such Copyright, including for administrative purposes.

ii. Copies of this thesis, either in full or in extracts and whether in hard or electronic copy, may be made only in accordance with the Copyright, Designs and Patents Act 1988 (as amended) and regulations issued under it or, where appropriate, in accordance with licensing agreements which the University has from time to time. This page must form part of any such copies made.

iii. The ownership of certain Copyright, patents, designs, trade marks and other intellectual property (the "Intellectual Property") and any reproductions of copyright works in the thesis, for example graphs and tables ("Reproductions"), which may be described in this thesis, may not be owned by the author and may be owned by third parties. Such Intellectual Property and Reproductions cannot and must not be made available for use without the prior written permission of the owner(s) of the relevant Intellectual Property and/or Reproductions.

iv. Further information on the conditions under which disclosure, publication and commercialization of this thesis, the Copyright and any Intellectual Property and/or Reproductions described in it may take place is available in the University IP Policy (see http://documents.manchester.ac.uk/DocuInfo.aspx?DocID=487), in any relevant Thesis restriction declarations deposited in the University Library, The University Library's regulations (see http://www.manchester.ac.uk/library/aboutus/regulations) and in The University's policy on Presentation of Theses.

ACKNOWLEDGEMENT

First and foremost, I would like to express my sincere gratitude to my supervisor Prof. Ian Kinloch for the continuous support of my PhD study and related research. During the PhD project, his immense knowledge broadens my horizon, his patience encourages me, and his motivation inspires me. Secondly my gratitude also goes to my co-supervisor Prof. Robert Young for his kind suggestions and guidance in the time of my research project.

Besides my advisor, I would like to thank the technicians in School of Materials, Andrij Zadoroshnyj, Andrew Forrest and other staff for their demonstrations of equipments applied in my projects.

My sincere thanks also goes to my colleagues, Zheling Li, Arunprakash. Arangaraju, Cristina Valles, Yue Lin, Xin Zhao and Fei Liu for all of helps and advices provided during the project.

I thank my friends, with whom I have spent the last four years and had endless fun together, in particular Xuekun Lu, Ruizhi Pei, Xun Zhang, Zheling Li, Daishu Qian, Pei He, Bing Liu, Yuanyuan Liu and Bo Yu.

I also would like to thank China Scholarship Council for the financial support during the four-year project.

Last but not the least, I would like to thank my family: my parents and to my brothers and sister for supporting me. My girlfriend Ms Huihui SUN, you have been my source of joy for the last four years, thanks.

CHAPTER 1 INTRODUCTION AND AIMS

Nanoscience and nanotechnology have become increasingly important with their applications in chemical, electrical, biomedical and many other fields. However these applications strongly depend on the synthesis of nanomaterials with various shapes, sizes and properties, as well as incorporating them into complex architectures [1]. One of the most promising areas for the application of nanomaterials is polymer nano-composites, where a polymer matrix incorporates nano-scale fillers [2]. Polymers, both synthetic and natural, play an essential and ubiquitous role in everyday life because of their broad range of properties. However, polymers have significant drawbacks such as low modulus and strength [3], and insulating electrical properties, which limits its potential applications in many fields. Therefore, improving the electrical and thermal properties of a polymer by the addition of suitable fillers to expand its application to the field of devices and other electronics is of great significance. In addition, polymers, used as structure materials, usually have a high possibility to be exposed to various environments involving high temperature and humidity, which has great effects on the physical and mechanical properties of the polymer matrix. Therefore, the water uptake property needs to be enhanced for practical applications.

The Toyota research group's [4] work on polymer nano-composites with large mechanical property enhancement using montmorillonite as filler in a Nylon-6 matrix, opened a new dimension in the fields of materials. Since that early work, there has been much research interest in polymer nanocomposites which use inorganic materials as nanofillers with potential applications in the automotive, aerospace, construction and electronic industries [5-9]. Thus far, most of the research has been focused on natural layered materials, such as layered silicates or synthetic clay (layered double hydroxide), which however has quite poor electrical and thermal conductivity and cannot meet the requirements for applications in some electrical fields [10-11]. Therefore, in order to overcome these disadvantages, some carbon-based materials have been introduced into the polymer composites, such as carbon black (CB), carbon nano-fiber (CNF), carbon nanotubes (CNTs) [12-15]. Amongst them, CNTs has been proved to be the most effective filler to enhance the mechanical and electrical properties [16-19]. However, the high production cost of CNTs

establishes an obstacle for the mass preparation of CNTs-based functional composites. Furthermore, the high viscosity increase of a polymer matrix with a relatively low addition of CNTs limits their processability. Thus another carbon based material, graphene, which was discovered recently [20] has become the hot topic in this research field due to its highly conductive property and low production cost.

Graphene, has attracted tremendous attention in recent years owing to its exceptional thermal, mechanical, and electrical properties [21-23]. Graphene nano platelets (GNPs), consists of 10's layers of graphene, to give a thickness of 1-15 nm and graphene-based materials also possess excellent electrical and thermal conductivities along with high modulus [24]. GNPs, as a graphene-based material, have been widely used in academia as composite reinforcement to improve electrical [25-28], mechanical [26, 29-32], and thermal [33-35] properties. However, these properties have a close relationship with the number of graphene layers stacked in GNPs, their aspect ratio and the preparation methods of composites [36-37]. Relatively little systemic work has been done about the effects of filler dispersion and types, and preparation methods on the performance of resulting nano-composite.

In this PhD project, in order to study the effects of different fillers and preparation methods on the properties of composites, two types of GNPs (M5 and M25) with different aspect ratios were used to prepare epoxy/GNPs composites. Three different formulating methods (shear mixing, solvent-assisted compounding and three-roll mill blending) will be applied to fabricate composite samples. It was expected that the inclusion of GNPs would improve the mechanical, thermal and water-up take properties of epoxy resin, which are critical for expanding its applications in many fields. The dispersion, orientation of fillers in the epoxy matrix and structure of the nano-composite was characterized by optical microscopy, scanning electron microscopy (SEM), rheometer, Raman spectroscopy and X-ray diffraction (XRD), and thermal, mechanical and electrical performance will be tested via impedance spectroscopy, tensile test, dynamic mechanical thermal analysis (DTMA), and steady state thermal conductivity measurement to see the relationship between structure and properties. Finally, samples prepared by shear mixing will be immersed in distilled water to measure their water uptake properties

and property characterizations will be carried out to study the effects of absorbed water on properties.

In this thesis, Chapter 2 is the literature review of the previous work on graphene and graphene-based nano-fillers and their polymer composites. Chapter 3 described the experimental process for composite and test sample preparation, and the background of characterization methods applied in this project. The dispersion and orientation are discussed in details in chapter 4. Chapter 5 mainly focuses on mechanical properties characterized by DMTA and tensile tests. Chapter 6 is the focus of this thesis, addressing thermal and electrical conductivity, and theoretical models and an equivalent circuit have been used to study structure of composites. During the last chapter, water uptake behaviour was measured, and the effects of long-time aging on mechanical, thermal and electrical properties have been investigated.

References

1. Evanoff, D. D.; Chumanov, G., Synthesis and Optical Properties of Silver Nanoparticles and Arrays. *ChemPhysChem* **2005,** *6* (7), 1221-1231.
2. Potts, J. R.; Dreyer, D. R.; Bielawski, C. W.; Ruoff, R. S., Graphene-based polymer nano-composites. *Polymer* **2011,** *52* (1), 5-25.
3. Utracki, L. A.; Polymer alloys and blends thermodynamics and rheology. Munich, **1990**, 356, ISBN 3-446-14200-2.
4. Usuki, A.; Kojima, Y.; Kawasumi, M.; Okada, A.; Fukushima, Y.; Kurauchi, T.; Kamigaito, O., Synthesis of nylon 6-clay hybrid. *Journal of Materials Research* **1993,** *8* (05), 1179-1184.
5. Godovsky, D. Y., Device Applications of Polymer-Nano-composites. In *Biopolymers·PVA Hydrogels, Anionic Polymerisation Nano-composites*, Springer Berlin Heidelberg: **2000;** Vol. 153, pp 163-205.
6. Zhang, Z.; Shi, Q.; Peng, J.; Song, J.; Chen, Q.; Yang, J.; Gong, Y.; Ji, R.; He, X.; Lee, J.-H., Partial delamination of the organo-montmorillonite with surfactant containing hydroxyl groups in maleated poly(propylene carbonate). *Polymer* **2006,** *47* (26), 8548-8555.
7. Sinha Ray, S.; Okamoto, M., Polymer/layered silicate nano-composites: a review from preparation to processing. *Progress in Polymer Science* **2003,** *28* (11), 1539-1641.

8. Leroux, F.; Besse, J.-P., Polymer Interleaved Layered Double Hydroxide: A New Emerging Class of Nano-composites. *Chemistry of Materials* **2001,** *13* (10), 3507-3515.
9. Li, P.; Kim, N.; Bhadra, S.; Lee, J., Electroresponsive property of novel poly(acrylate- acryloyloxyethyl trimethyl ammonium chloride)/clay nano-composite hydrogels. In *2nd International Conference on Multi-Functional Materials and Structures*, **2009;** Vol. 79-82, pp 2263-2266.
10. Bao, Y.-Z.; Cong, L.-F.; Huang, Z.-M.; Weng, Z.-X., Preparation and proton conductivity of poly(vinylidene fluoride)/layered double hydroxide nano-composite gel electrolytes. *Journal of Materials Science* **2008,** *43* (1), 390-394.
11. Uddin, F., Clays, Nanoclays, and Montmorillonite Minerals. *Metallurgical and Materials Transactions A* **2008,** *39* (12), 2804-2814.
12. Mazinani, S.; Ajji, A.; Dubois, C., Morphology, structure and properties of conductive PS/CNT nano-composite electrospun mat. *Polymer* **2009,** *50* (14), 3329-3342.
13. Geng, Y.; Liu, M. Y.; Li, J.; Shi, X. M.; Kim, J. K., Effects of surfactant treatment on mechanical and electrical properties of CNT/epoxy nano-composites. *Composites Part A: Applied Science and Manufacturing* **2008,** *39* (12), 1876-1883.
14. Li, Q.; Park, O.; Lee, J., Positive temperature coefficient behaviour of HDPE/EVA blends filled with carbon black. In *2nd International Conference on Multi-Functional Materials and Structures*, **2009;** Vol. 79-82, pp 2267-2270.
15. Renukappa, N. M.; Siddaramaiah; Sudhaker Samuel, R. D.; Sundara Rajan, J.; Lee, J., Dielectric properties of carbon black: SBR composites. *Journal of Materials Science: Materials in Electronics* **2009,** *20* (7), 648-656.
16. Liao, S.-H.; Weng, C.-C.; Yen, C.-Y.; Hsiao, M.-C.; Ma, C.-C. M.; Tsai, M.-C.; Su, A.; Yen, M.-Y.; Lin, Y.-F.; Liu, P.-L., Preparation and properties of functionalized multiwalled carbon nanotubes/polypropylene nano-composite bipolar plates for polymer electrolyte membrane fuel cells. *Journal of Power Sources* **2010,** *195* (1), 263-270.
17. Jeevananda, T.; Siddaramaiah; Kim, N. H.; Heo, S.-B.; Lee, J. H., Synthesis and characterization of polyaniline-multiwalled carbon nanotube nano-composites in the presence of sodium dodecyl sulfate. *Polymers for Advanced Technologies* **2008,** *19* (12), 1754-1762.
18. Sandler, J. K. W.; Kirk, J. E.; Kinloch, I. A.; Shaffer, M. S. P.; Windle, A. H., Ultra-low electrical percolation threshold in carbon-nanotube-epoxy composites. *Polymer* **2003,** *44* (19), 5893-5899.
19. Spitalsky, Z.; Tasis, D.; Papagelis, K.; Galiotis, C., Carbon nanotube–polymer composites: Chemistry, processing, mechanical and electrical properties. *Progress in Polymer Science* **2010,** *35* (3), 357-401.
20. Novoselov, K. S.; Geim, A. K.; Morozov, S. V.; Jiang, D.; Zhang, Y.; Dubonos, S. V.; Grigorieva, I. V.; Firsov, A. A., Electric Field Effect in Atomically Thin Carbon Films. *Science* **2004,** *306* (5696), 666-669.
21. Zhu, Y.; Murali, S.; Cai, W.; Li, X.; Suk, J. W.; Potts, J. R.; Ruoff, R. S., Graphene and Graphene Oxide: Synthesis, Properties, and Applications. *Advanced Materials* **2010,** *22* (35), 3906-3924.

22. Geim, A. K.; Novoselov, K. S., The rise of graphene. *Nat Mater* **2007,** *6* (3), 183-191.
23. Compton, O. C.; Nguyen, S. T., Graphene Oxide, Highly Reduced Graphene Oxide, and Graphene: Versatile Building Blocks for Carbon-Based Materials. *Small* **2010,** *6* (6), 711-723.
24. Chandrasekaran, S.; Seidel, C.; Schulte, K., Preparation and characterization of graphite nano-platelet (GNP)/epoxy nano-composite: Mechanical, electrical and thermal properties. *European Polymer Journal* **2013,** *49* (12), 3878-3888.
25. Chen, G.; Weng, W.; Wu, D.; Wu, C., PMMA/graphite nanosheets composite and its conducting properties. *European Polymer Journal* **2003,** *39* (12), 2329-2335.
26. Kalaitzidou, K.; Fukushima, H.; Drzal, L. T., A new compounding method for exfoliated graphite–polypropylene nano-composites with enhanced flexural properties and lower percolation threshold. *Composites Science and Technology* **2007,** *67* (10), 2045-2051.
27. Wu, X.; Qi, S.; He, J.; Duan, G., High conductivity and low percolation threshold in polyaniline/graphite nanosheets composites. *Journal of Materials Science* **2010,** *45* (2), 483-489.
28. Vadukumpully, S.; Paul, J.; Mahanta, N.; Valiyaveettil, S., Flexible conductive graphene/poly(vinyl chloride) composite thin films with high mechanical strength and thermal stability. *Carbon* **2011,** *49* (1), 198-205.
29. Kim, S.; Drzal, L. T., Comparison of Exfoliated Graphite Nanoplatelets (GNP) and CNTs for Reinforcement of EVA Nano-composites Fabricated by Solution Compounding Method and Three Screw Rotating Systems. *Journal of Adhesion Science and Technology* **2009,** *23* (12), 1623-1638.
30. Ramanathan, T.; Stankovich, S.; Dikin, D. A.; Liu, H.; Shen, H.; Nguyen, S. T.; Brinson, L. C., Graphitic nanofillers in PMMA nano-composites—An investigation of particle size and dispersion and their influence on nano-composite properties. *Journal of Polymer Science Part B: Polymer Physics* **2007,** *45* (15), 2097-2112.
31. Kalaitzidou, K.; Fukushima, H.; Drzal, L. T., Mechanical properties and morphological characterization of exfoliated graphite–polypropylene nano-composites. *Composites Part A: Applied Science and Manufacturing* **2007,** *38* (7), 1675-1682.
32. Kim, S.; Do, I.; Drzal, L. T., Thermal stability and dynamic mechanical behaviour of exfoliated graphite nanoplatelets-LLDPE nano-composites. *Polymer Composites* **2010,** *31* (5), 755-761.
33. Veca, L. M.; Meziani, M. J.; Wang, W.; Wang, X.; Lu, F.; Zhang, P.; Lin, Y.; Fee, R.; Connell, J. W.; Sun, Y.-P., Carbon Nanosheets for Polymeric Nano-composites with High Thermal Conductivity. *Advanced Materials* **2009,** *21* (20), 2088-2092.
34. Yu, A.; Ramesh, P.; Sun, X.; Bekyarova, E.; Itkis, M. E.; Haddon, R. C., Enhanced Thermal Conductivity in a Hybrid Graphite Nanoplatelet – Carbon Nanotube Filler for Epoxy Composites. *Advanced Materials* **2008,** *20* (24), 4740-4744.
35. Debelak, B.; Lafdi, K., Use of exfoliated graphite filler to enhance polymer physical properties. *Carbon* **2007,** *45* (9), 1727-1734.

36. Tong, X.; Wang, H.; Wang, G.; Wan, L.; Ren, Z.; Bai, J.; Bai, J., Controllable synthesis of graphene sheets with different numbers of layers and effect of the number of graphene layers on the specific capacity of anode material in lithium-ion batteries. *Journal of Solid State Chemistry* **2011,** *184* (5), 982-989.
37. Kuilla, T.; Bhadra, S.; Yao, D.; Kim, N. H.; Bose, S.; Lee, J. H., Recent advances in graphene based polymer composites. *Progress in Polymer Science* **2010,** *35* (11), 1350-1375.

CHAPTER 2 LITERATURE REVIEW

2.1 Discovery and Properties of Graphene

Graphene is a two-dimensional sheet of sp^2-hybridized carbon and is one of the strongest and stiffest known materials. It has attracted considerable research interest despite of its short history. Graphene can be visualized as the basic material for the other dimensional sp^2 materials. As illustrated in Figure 2.1, 0D fullerenes, 1D carbon nanotubes and 3D graphite can be obtained by wrapping up or stacking graphene [1].

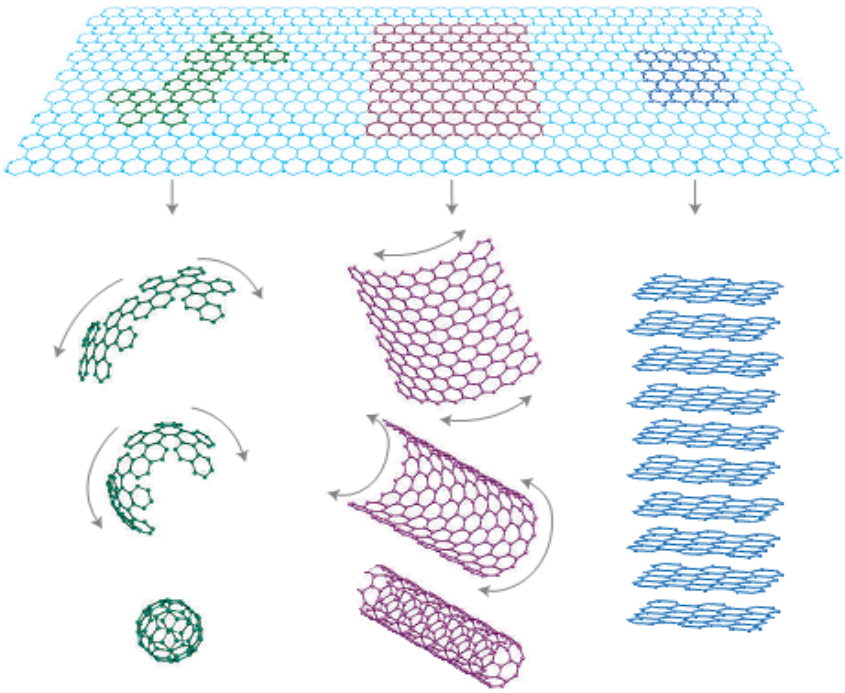

Figure 2.1 Structure of graphene and other carbon materials. Adapted from [1].

The unique structure and symmetry of graphene gives rise to its exceptional physical and chemical properties [2]. For example, the electronic properties of graphene have a very close relationship to its number of layers (Figure 2.2 [3-4]). Monolayer and bilayer graphene are both zero-gap semiconductors. However, for three or more layers, the conduction and valence bands begin to overlap [3] and when the number of layers is 10 or higher the electronic properties tend to that of bulk graphite.

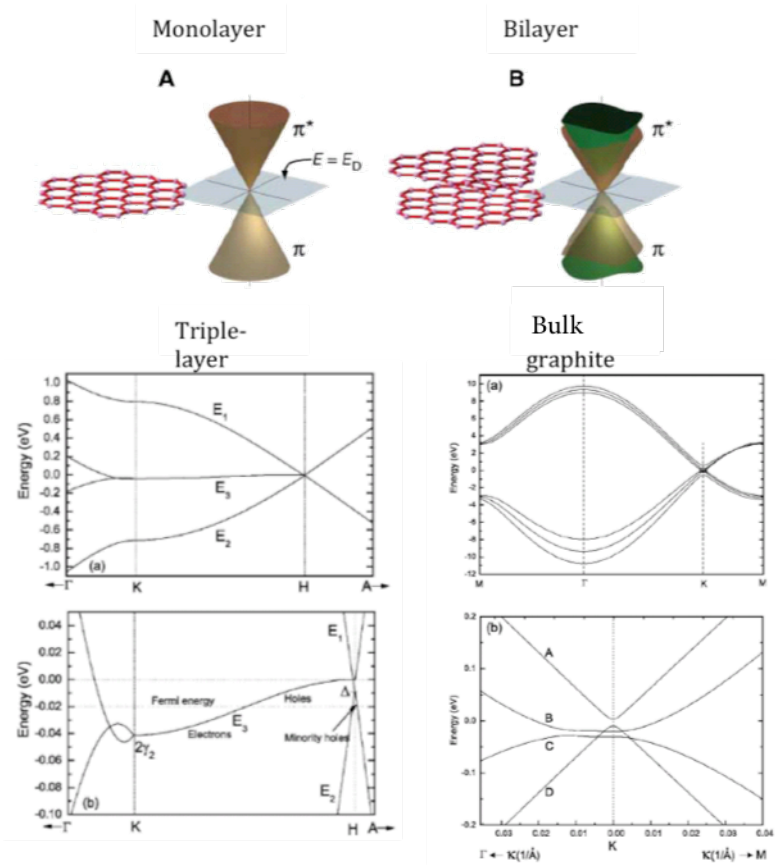

Figure 2.2 Electronic band structure of graphene and bulk graphite [3-4].

Monolayer graphene has a very high charge carrier mobility, (< 15,000 cm^2/Vs), even at room temperature [1]. The mobility, though, is strongly affected by the underlying substrate, with the highest mobility of > 200,000 cm^2/Vs at electron densities of $\sim 2\times10^{11}$ cm^{-2} being achieved by suspending the graphene layer [5]. Furthermore, graphene can show a Quantum Hall Effect (QHE) at room-temperature, giving the possibility of the development of new QHE resistance standards [6].

Lee *et al.* measured the elastic modulus and intrinsic tensile strength of a free-standing monolayer graphene sheet using atomic force microscopy and calculated the in-plane Young's modulus to be about 1.0 TPa, and the intrinsic strength of bulk graphite to be 130 GPa [7], very close to that predicted by theory [8]. These properties mean the graphene is the strongest known material, although for bulk graphite materials the strength is limited by defects and grain boundaries. In addition, graphene has a very high surface area (2600 m^2 g^{-1}), aspect ratio, thermal conductivity (3000-5000 W $m^{-1}K^{-1}$), electromagnetic interference (EMI) shielding ability, flexibility, transparency, and low coefficient of thermal expansion (CTE) [9-13]. All

of these superb properties give graphene the advantages to act as a preferred nano-filler over other carbon-based materials.

2.1.1 Synthesis of Graphene

Graphene was first isolated by the mechanical exfoliation of graphite using Scotch Tape® at the University of Manchester in 2004 [3]. This method can give a nearly perfect structure of single layer of carbon atom and is suitable for laboratory research but does not yield sufficient quantities for applications such as composites. In order to overcome this disadvantage, several other graphene preparation methods have been developed [10-12, 14-16], including the liquid phase exfoliation of natural graphite or graphite intercalation compounds (Figure 2.3) [17], rapid heating of graphene intercalation compounds, chemical vapour deposition (CVD), using ethylene to discompose on nickel surfaces [18], electric arc discharge, plasma enhanced CVD (PE-CVD), epitaxial growth on insulating surfaces such as silicon carbide (SiC), un-zipping of carbon nanotubes (CNTs), and the chemical (and electrochemical) reduction of graphite oxide [19-26]. The latter is currently most commonly applied in the composite literature due mainly to its high yield and low cost. Among them, liquid exfoliation and mechanical exfoliation yield the best quality graphene, possessing the best mechanical and electrical properties. However, pristine graphene is unsuitable for polymer composite fabrication due to its high tendency to aggregate in a polymer matrix [27-28]. Chemical routes such as the reduction of graphite oxide produce graphene with side groups, like hydroxyl and carboxyl groups, which will facilitate dispersion and stabilization of graphene to prevent aggregation [28-29]. After chemical functionalization, it can enhance the interfacial interactions with polymer matrix.

In this project, the GNP used is produced predominantly by the rapid heating of graphene intercalation compounds. This route is non-oxidizing so the resultant material has a pristine graphitic surface of sp^2 carbon molecules that makes it especially suitable for applications requiring high electrical or thermal conductivity, but also leads to difficulty in producing uniform dispersions in a polymer matrix.

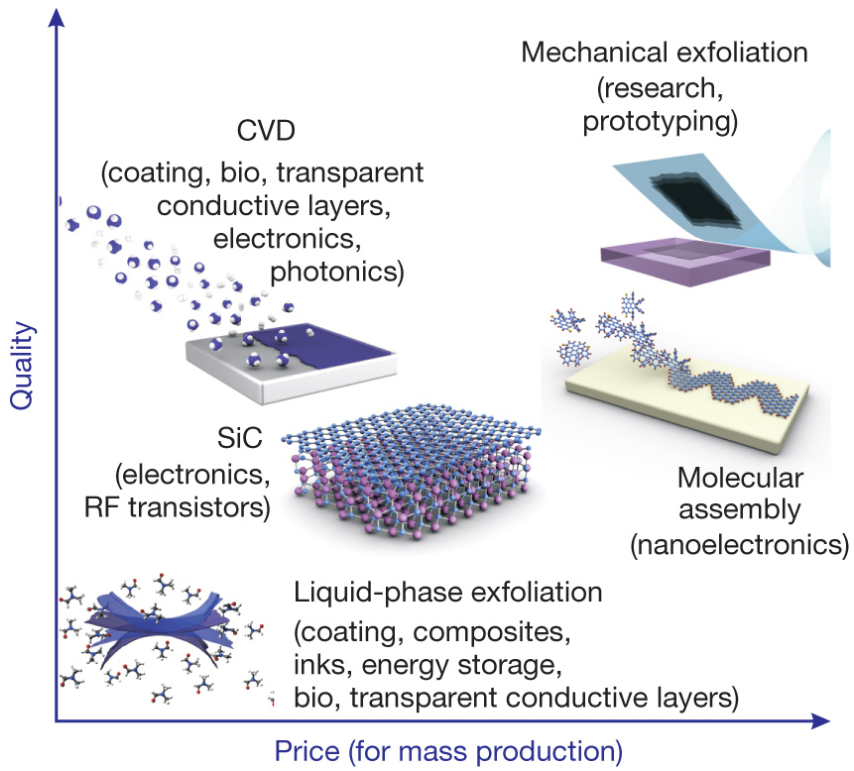

Figure 2.3 Several methods of large scale production of graphene, which allow a wide range in terms of size, quality and price for any particular applications. Novoselov et al. [30].

2.1.2 **Graphene Oxide**

Graphene oxide (GO) is the most common form of functionalized graphene and tends to be formed directly from graphite as part of the exfoliation process. The Hummers method is mostly used for synthesis of GO, by using a combination of potassium permanganate and sulfuric acid [12]. A proposed structure of GO is shown in Figure 2.4 [31-33]. Owing to the side groups on the surface of GO sheets like hydroxyl, diol, and carboxyl groups, it can be easily dissolved in water [34] and many organic solvent and stay stable for long time, which is different from pristine graphene. The solvent and the extent of surface functionalization determine GO's solubility and the maximum dispersibility, which is critical for processing and further derivatization [12].

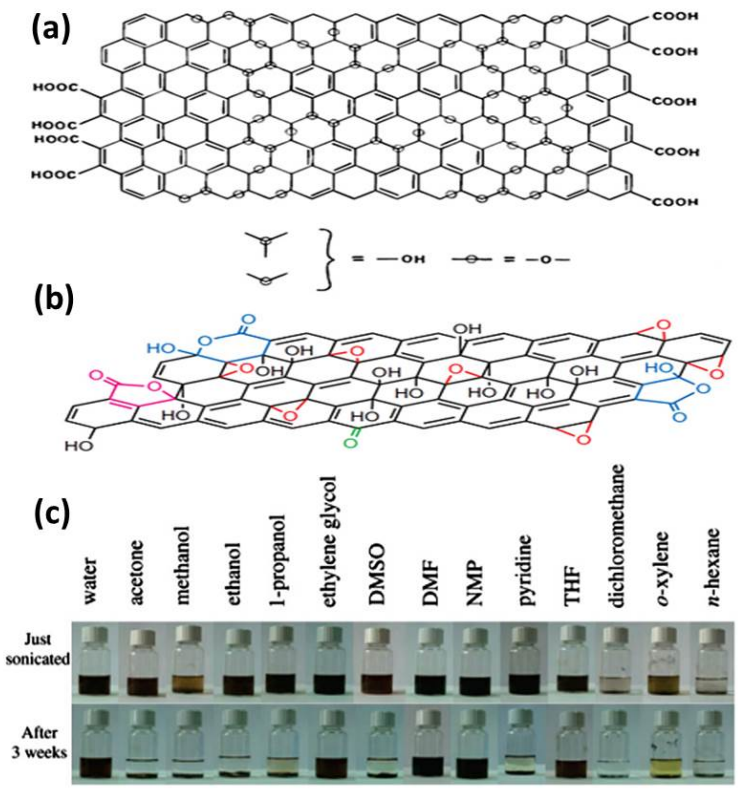

Figure 2.4 Models of the basal plane of GO (a) [33] and (b) [31]. (c) Digital pictures of as-prepared graphite oxide dispersed in water and other organic solvents using sonication [32].

Graphene oxide, with its disrupted sp^2 structure, is electrically insulating that limits its applications. Therefore reduction is one of the most important reactions for GO [12], which can restore the sp^2 network and hence increase the electrical conductivity.

However, when the reduction of GO is carried out in solution, the process usually leads to precipitation of graphite nano-sheet irreversibly. Therefore, in order to stabilize reduced GO, some covalent modifications are usually carried out by taking advantage of the side group, such as the carboxylic acid group [35-36] and epoxy group [37-38]. Apart from that non-covalent functionalization [39] is also commonly applied [40-41].

GO is the most commonly used starting material for covalent modification, hence the possibility of developing reduction methods that can largely eliminate residual oxygen functionality whilst adding chemical functionality for large-scale production of graphene.

2.1.3 Chemical Functionalization of Graphene

Pure graphene has a strong tendency to aggregate in the polymer due to the van der Waals interaction between individual graphene sheets and the weak interaction between graphene and polymers. This aggregation affects the homogeneous dispersion of the graphene in a matrix and lowers the strength of the graphene-polymer interface. Since the physical properties of aggregated graphene sheets are inferior to pristine graphene, the degree of reinforcement in the composites are not as high as expected for truly dispersed monolayer sheets [42-43]. Functionalization of graphene is a promising way to improve its solubility and stability in polymer matrix.

2.1.3.1 Covalent Functionalization

Covalent functionalization of pristine graphene forms covalent adducts with the sp^2 carbon structures in and typically requires reactive species, like nitrenes, carbenes, and arynes as shown in Figure 2.5.

Functionalization, through lowering the surface energy of the graphene can stabilize graphene dispersions [44-47]. In order to apply graphene in electronic and photonic fields, opening a band gap in graphene is needed, which can be achieved by basal plane functionalization [48-50].

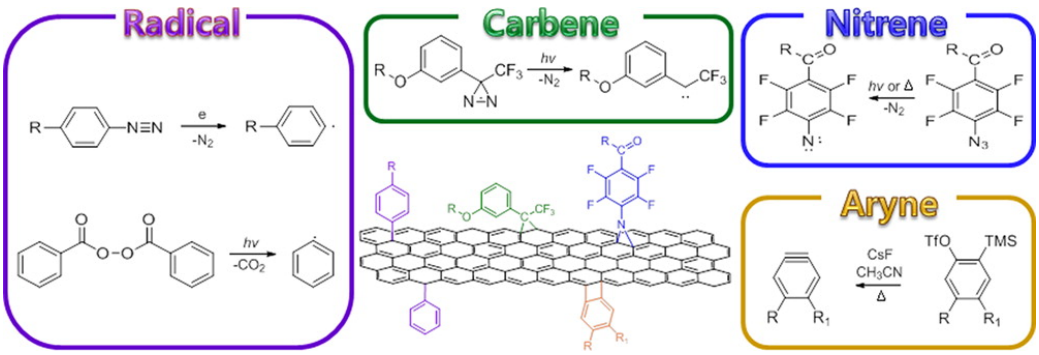

Figure 2.5 Several reactive intermediates of radicals, nitrenes, carbenes, and arynes used in graphene functionalization. These reactive species covalently modify graphene through free radical addition, CH insertion, or cycloaddition reactions [51].

Wang *et al.* [51] reported that the covalent functionalisation of graphene could be beneficial for their uniform dispersion in the epoxy matrix even at a high filler loading (Figure 2.6).

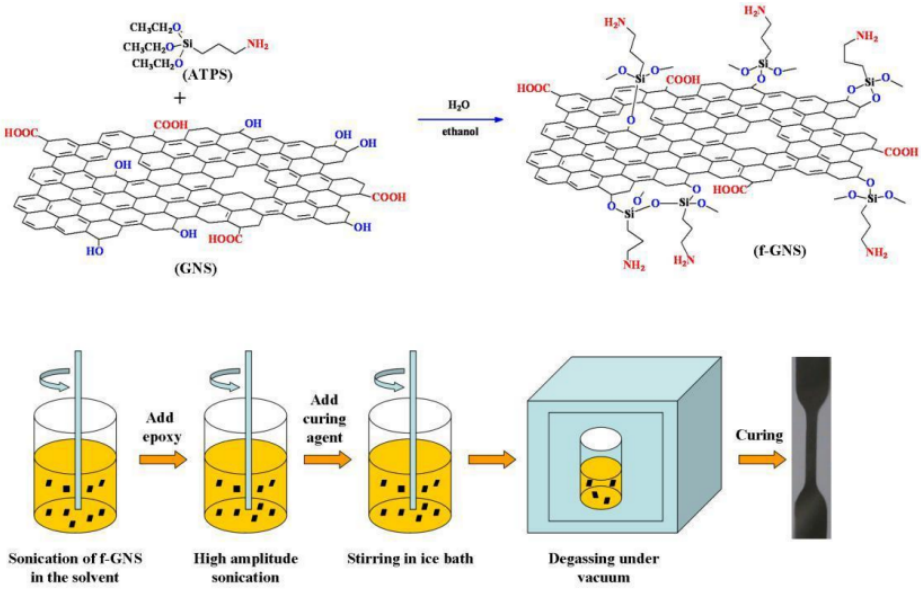

Figure 2.6 Illustration of interaction between graphene fillers and APTS, and the incorporating process of modified-graphene nanoplatelets into the epoxy matrix. Wang X et al. [51].

Yang *et al.* presented a method to obtain polydisperse chemically-converted graphene sheets (p-CCG) (as shown in Figure 2.7) that are covalently functionalized with ionic liquid, which can stay in water, dimethylformamide (DMF), or dimethyl sulfoxide (DMSO) stably [38].

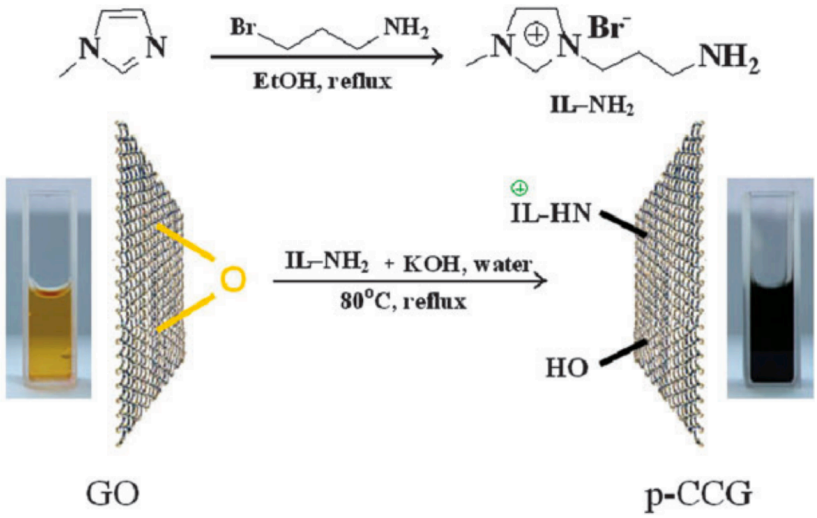

Figure 2.7 The preparation process of p-CCG [38].

Considerable work has been done on the covalent modification of graphene [52-56]. This method gives a strong bond between functional group and graphene, but sometimes it causes some damage to the sp^2 structure and leads to the decrease of electrical properties.

2.1.3.2 Non-covalent Functionalization

Figure 2.8 [57] shows non-covalent functionalization of graphene by attaching polymers chain and small-molecules and the structure of adsorbates commonly used. The lack of functionality on the smooth surface of pristine graphene makes it difficult to obtain covalent modification, thus non-covalent functionalization is a widely used method to modify the surface of graphene [57], and is critical to the stabilization of proteins, DNA-protein, organic supramolecules, and functional nanomaterials [58-63].

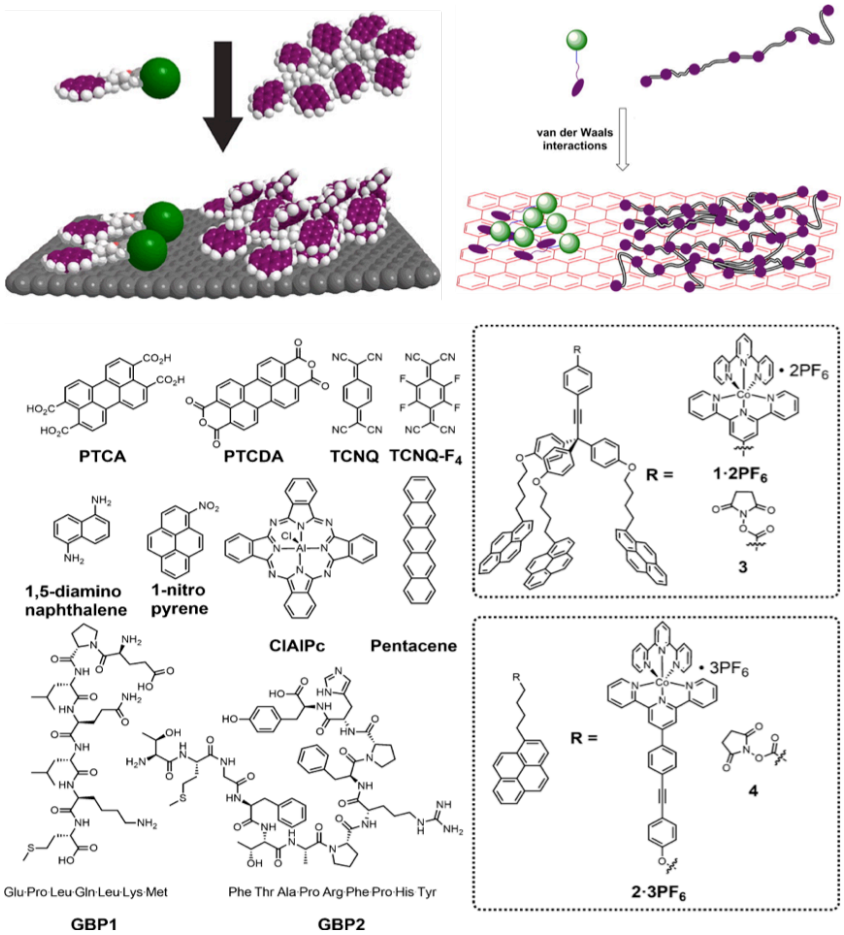

Figure 2.8 Schematic of noncovalent functionalization of graphene using polymers and small-molecule adsorbates. Adapted from [57].

Apart from π- π, a significant amount of work on noncovalent functionalization of graphene via van der Waals and ionic interactions between graphene and a functionalized molecule has been carried out [64-68].

2.2 Characterisation of Graphene

2.2.1 Raman Spectroscopy

Raman spectroscopy is a very useful and powerful tool to characterize the structure of carbon-based materials [69] including the behaviour of electrons and phonons in graphene [70-71].

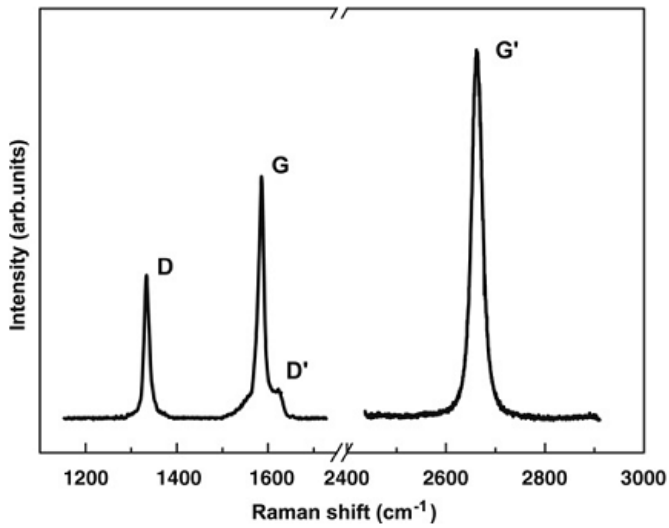

Figure 2.9 Typical Raman spectrum for graphene edge, showing the main Raman features, the D, G and G' bands [71].

Graphene prepared by different methods will have different Raman features. The chemically reduced graphene shows extensive defects, which will be clearly reflected by the peak around 1350 cm^{-1} (D band) in Raman spectra (Figure 2.9) [71]. D band is characteristic of defects and disorders. While graphene prepared by CVD usually shows no/small D band; liquid phase production, and mechanical exfoliation of graphite exhibit no defects, which shows these graphene have a better structure than chemically reduced graphene oxide [72-73]. Graphene, regardless of production route, exhibits a peak at around 1580 cm^{-1} (termed as G band).

Apart from the D band and G band, there is a peak around 2700 cm^{-1} (G' band) originating from a second-order process. Since the G' band is approximately twice the

D band frequency, some literature prefer to call it the 2D band. G' band is a very important Raman feature that is strongly dependent on the number of the layers of graphene in the sample.

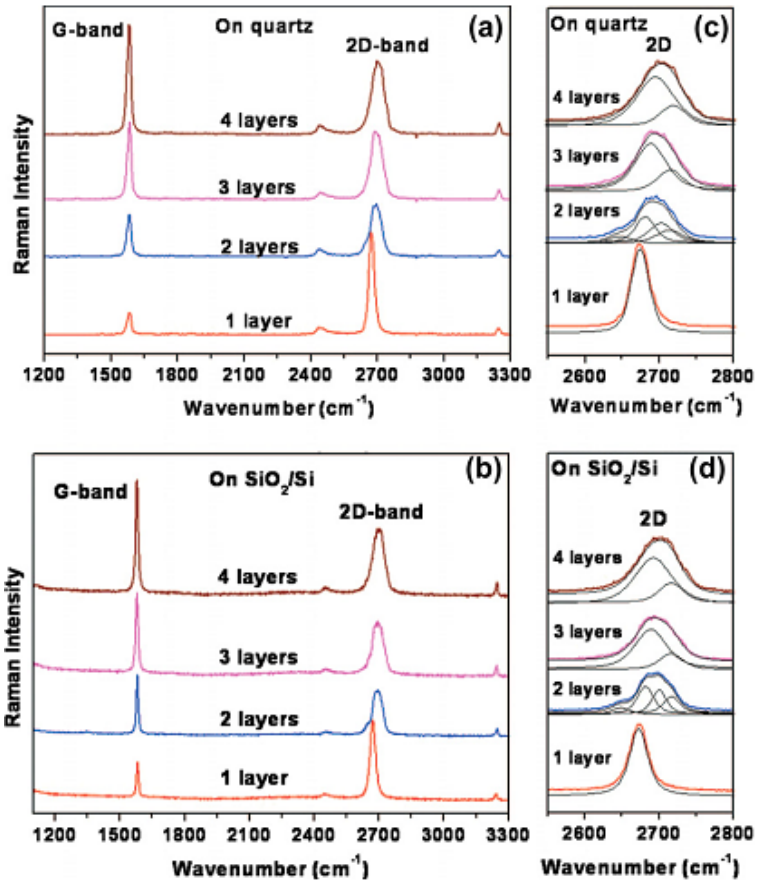

Figure 2.10 The Raman spectra for various layers of graphene on quartz (a) and on a SiO_2 (300 nm)/Si substrate (b). The enlarged 2D band regions with the curve fitting are shown in panel (c) and (d) [74].

For monolayer graphene, the 2D band is single sharp peak, while there are two peaks of this band in graphite. Furthermore, the G band intensity of monolayer graphene is lower than that of bi-, tri-, or multi-layer graphene and increases in wavelength linearly with increasing number of layers, as is shown in Figure 2.10 [74]. For bilayer graphene, the 2D band is much broader and up-shifted compared to monolayer graphene. Hence, Ferrari *et al.* deduced that Raman spectroscopy could clearly distinguish between a single layer, bilayer, and several layers (<5 layers) [75].

Apart from that, several recent papers have established that the Raman bands of monolayer graphene shift during deformation. The shift of 2D band can be applied to test the interfacial stress transfer of graphene/polymer composites [76-78].

Generally, there are several common methods having been adopted to apply strain to the graphene [79]. One is to deposit graphene on a substrate which can be achieved by chemical functionalization or piezo positioners treatment [80]. Second method is to use the difference of thermal expansion coefficients of the substrate and graphene to induce strain by thermal processes [81-82]. One of the most common methods is to couple the graphene onto a flexible substrate and to stretch or bend directly [76-78, 83].

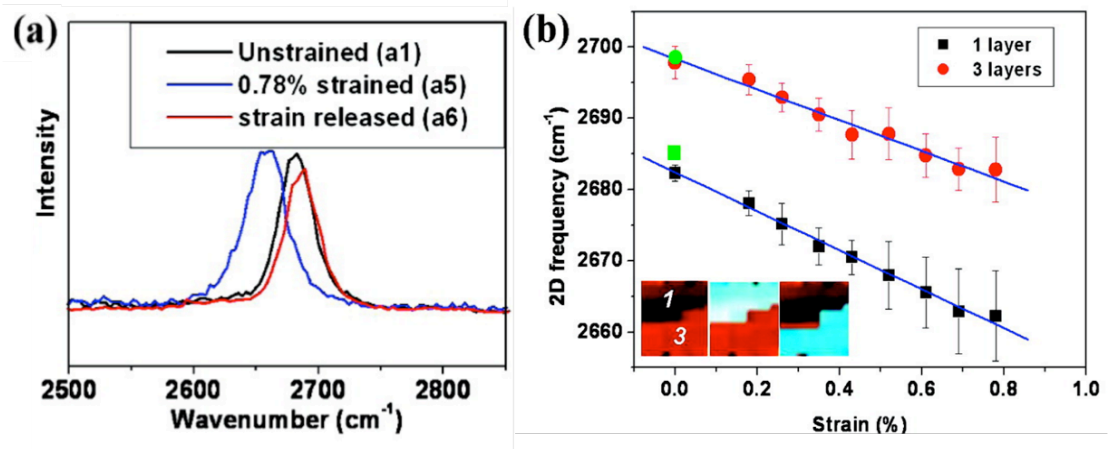

Figure 2.11 (a) The 2D band of monolayer graphene at unstrained, 0.78% strain and with strain released. (b) The 2D band position shift versus applied strain for monolayer and tri-layer graphene [83].

Ni *et al*. [83] deposited graphene onto a flexible PET film and applied a uniaxial tensile strain up to ~0.8% (as shown in Figure 2.11). They found the 2D band shifted to lower frequency linearly as the uniaxial strain was applied, with the slope of ~-27.8 $cm^{-1}/\%$.

Gong L *et al*. [76] used Raman spectroscopy to monitor stress transfer in a system consisting of a thin polymer matrix layer with a mechanically exfoliated monolayer graphene using the stress-sensitivity of the graphene 2D band. For the first time it was reported that the possibility to map the deformation of graphene monolayer in a polymer composite.

Another use of the Raman technique is to use polarized Raman spectroscopy to characterize a carbon filler's orientation based on the knowledge that the intensity of the Raman bands depends upon the direction of laser polarization [84].

2.2.2 Atomic Force Microscopy

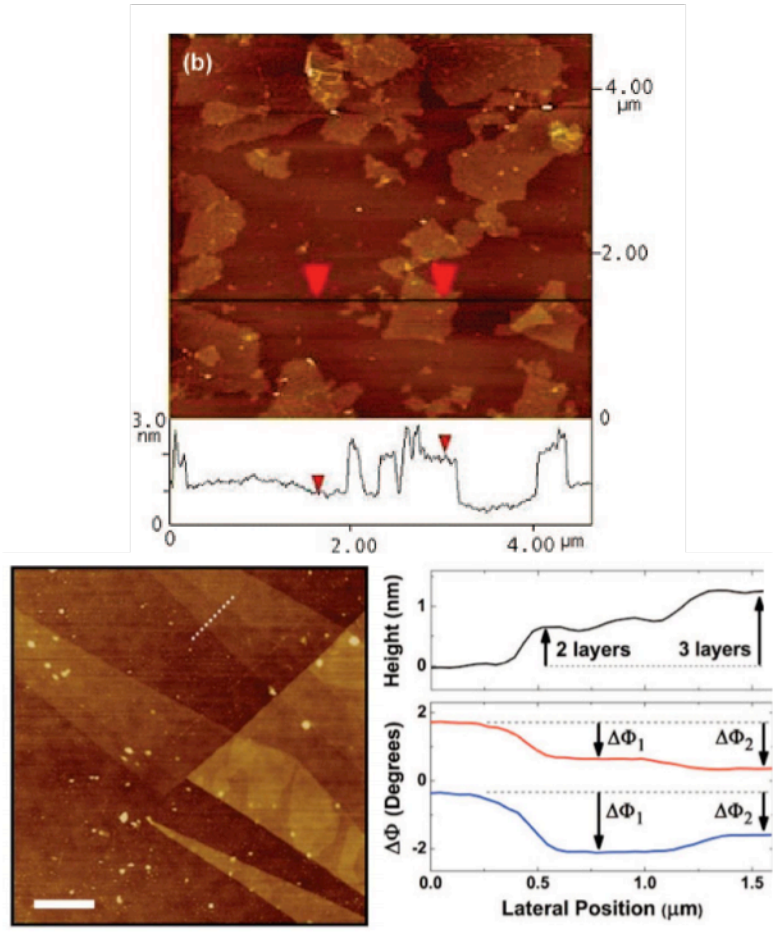

Figure 2.12 Thickness of graphene measured using AFM. Adapted from [85-86].

Atomic force microscope (AFM) is one of the most used methods for identifying single layer graphene and to measure the thickness of few layer graphene. The thickness of graphene prepared by various methods is around 0.34nm (Figure 2.12) [85-86].

2.2.3 X-ray Diffraction

X-ray diffraction (XRD), when compared with Raman spectra and AFM, is not a perfect method to characterise graphene, but still very useful. In an XRD pattern (λ = 1.542 Å), pristine graphite shows a basal reflection (002) peak at $2\theta = 26.6^{o}$ (d spacing = 0.335 nm). After oxidation to form GO, the d_{002} spacing increases to 0.79

nm ($2\theta = 11.2^{o}$) due to the functional groups and the intercalation of water molecules and generation of oxygen functionality in the interlayer spacing of graphite. No apparent diffraction peak but a straight line in the XRD pattern is obtained (Figure 2.13) when GO is completely exfoliated to a single layer of GO. After reduction of GO into graphene, the XRD pattern of as-obtained graphene shows exactly the same XRD pattern as that of single-layer GO, suggesting the periodic structure of graphite has been restored [87].

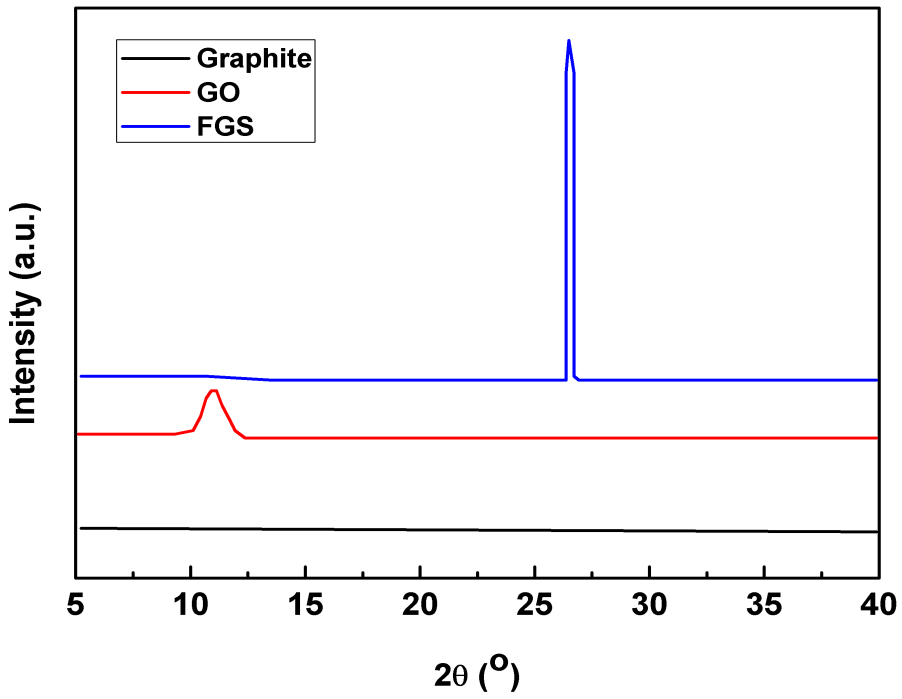

Figure 2.13 XRD intensity profiles of graphite, GO and individually exfoliated graphene sheets [87].

Therefore, when GO or graphene are used as fillers to prepare composites, the XRD pattern is a good tool to characterize the dispersion of the fillers in the matrix.

2.2.4 Transmission Electron Microscopy

TEM can image materials at a very high resolution due to the small de Broglie wavelength of electrons, making examining detail even as small as a single column of atoms possible. Therefore, TEM can be used to confirm the thickness of a graphene sample.

The Figure 2.14 [88-89] shows typical TEM and high-resolution transmission electron microscopy (HRTEM) images of graphene and the corresponding small area electron diffraction (SAED) patterns. From Figure 2.14 (c) and (d), we can clearly see an electron transparent graphene flake, indicating single-layer or few layer graphene. The edges of the suspended film sometimes fold back, allowing for a cross-sectional view, from which HR-TEM can be used to approximate the number of layers. Figure 2.14 (a, b and f) shows clearly few layers graphene sheets. The SAED pattern of monolayer graphene (Figure 2.14e) exhibits the typical six-fold graphene symmetry.

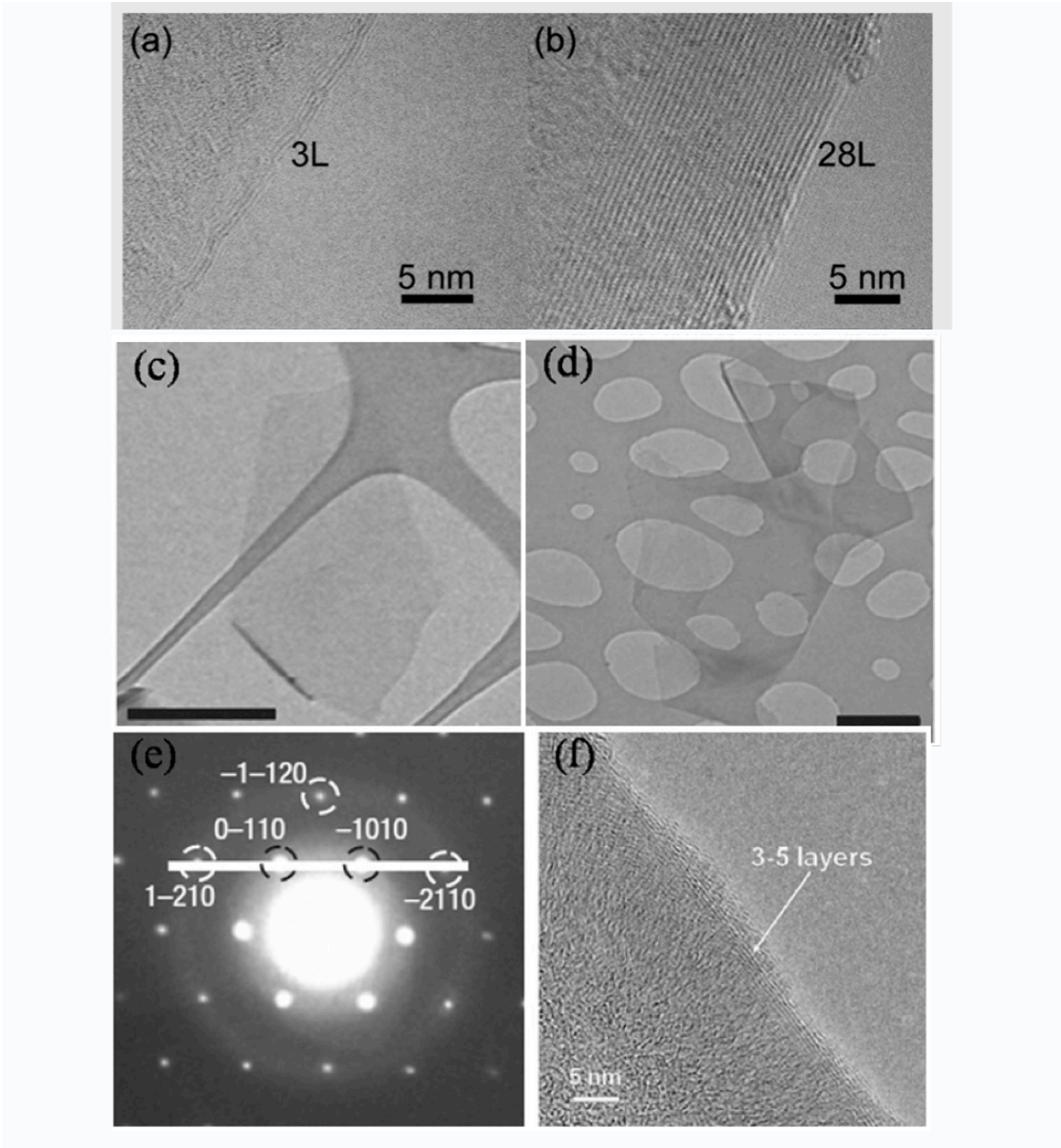

Figure 2.14 Graphene thickness analysis. High-resolution TEM images of the folded graphene edge, where the dark lines indicate the number of layers of (a) 3, (b) 28 and 3-5 (f).

(c, d) Bright-field TEM images of a folded graphene sheet and multilayer graphene, both deposited from NMP, (e) Electron diffraction pattern of the graphene sheet with the peaks labelled by Miller–Bravais indices Adapted from [88-89].

2.3 Preparation Methods of Polymer/Graphene Composites

According to the literature, there are three main routes to prepare polymer/graphene composites: *In-situ* polymerization, solution blending and melt mixing [90]. The advantages of each technique as well as their disadvantages are discussed below.

2.3.1 *In-situ* Polymerization

In-situ polymerization can benefit both the dispersion of graphene in a polymer matrix and the interaction between them. It is based upon the functionalization techniques discussed in section 2.1.3. Typically graphene or modified graphene fillers are swollen in a liquid monomer. A suitable initiator is then added and the polymerization is initiated by either heating or radiation. During this method, the monomer is polymerized in the presence of the filler, to give the strongest interaction amongst the three methods. As a result, composites fabricated by this method usually have better mechanical properties and thermal conductivity compared to solution compounding and melt blending. The drawbacks are that (i) it will consume considerable amount of electrical energy during dispersion process, (ii) relatively poor dispersion of fillers in matrix and (iii) low productivity.

2.3.2 Solution Compounding

Solution compounding is when the polymer is first dissolved in a suitable solvent, followed by addition of graphene or modified graphene fillers. After mixing, the solvent is removed from the system and the polymer containing graphene fillers is then moulded to the final shape.

This technique results typically in a low electrical percolation threshold. In this method, the dispersion of graphene and polymer in the solvent is critical in controlling the final microstructure, as well as the process used to remove the solvent. Pure graphene from mechanical exfoliation is difficult to disperse in a solvent, which

is the reason for the modification of graphene. Chemically reduced graphene or modified graphene can be easily dispersed in various solvents (for example water, acetone, DMF and toluene) owing to the weak forces between the layers. During the dispersion process, the polymer absorbs onto the exfoliated sheets such that when the solvent is removed, the resulting of nanocomposite consist of sheets well dispersed in the polymer [91].

The main advantage of solution compounding is that it allows the synthesis of nano-composites using polymers with low polarity [16]. The disadvantage is the use of large amounts of solvent and its removal, which is not environmentally friendly and is energetically costly.

2.3.3 Melt Blending

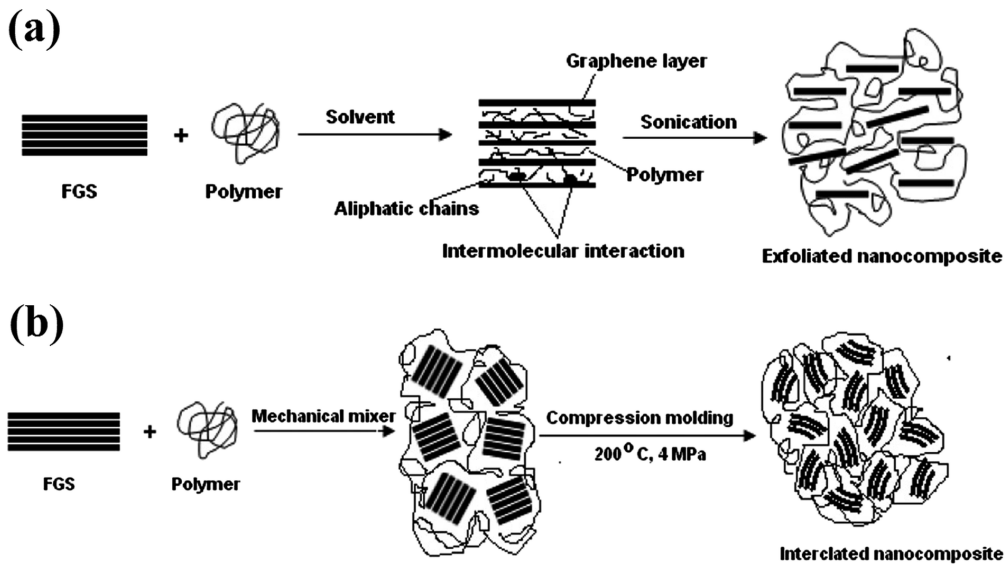

Figure 2.15 The incorporation process of exfoliated graphene sheets (FGS) into polymer by (a) solvent technique and (b) melt blend technique. Adapted from [87].

Melt blending is a desirable fabrication method for the industrial production of polymer/graphene nano-composites, as it is a continuous and environmentally friendly process, with no solvent used [16, 87]. Graphene or modified graphene is directly mixed with the polymer matrix (usually thermoplastic polymer) in molten state to form composites. Traditional mechanical blending equipment such as internal mixers, extruders, and two-roll mills can be adopted for the melt blending process [87, 92]. The main shortcoming of this method is the poorer dispersion of fillers in matrix than that achieved by the other two techniques.

2.3.4 Combination of Mixing Techniques

As mentioned above, the three fabricate methods have both advantages and disadvantages. Therefore, in order to harness the virtues of each and mitigate their drawbacks, some polymer/graphene composites have been prepared by a combination of two of more methodologies. In the case of epoxy resin, due to the rapid increase of viscosity upon solvent removal, the combined method becomes necessary (as shown in Figure 2.16) [93] and is a promising route for composite fabrication.

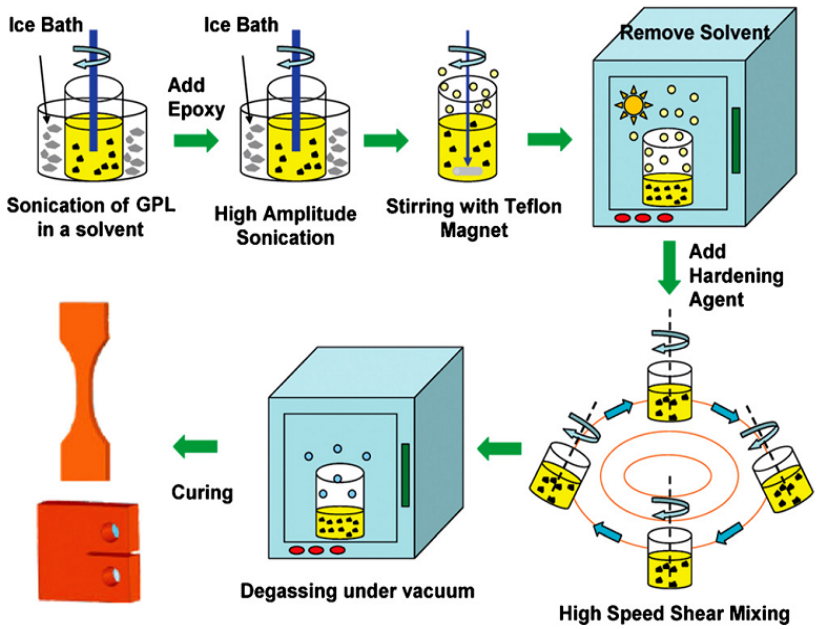

Figure 2.16 Combination of various preparation methods to disperse GNP into an epoxy matrix. [93].

2.4 Properties of Polymer/Graphene Composites

2.4.1 Mechanical Properties

Graphene is the stiffest material ever measured with in-plane elastic modulus of approximately 1.1 TPa. Thus, when incorporated into a polymer it is expected to reinforce the mechanical properties of the resultant composite. The very large modulus values, along with the large surface areas of the platelets, allow graphene or modified graphene fillers to act as the main load-bearing component of a polymer composite. Figure 2.17 and Figure 2.18 provide an example of the reinforcing effect of foliated graphene/poly(ethyleneoxide) (PEO) nano-composites [87].

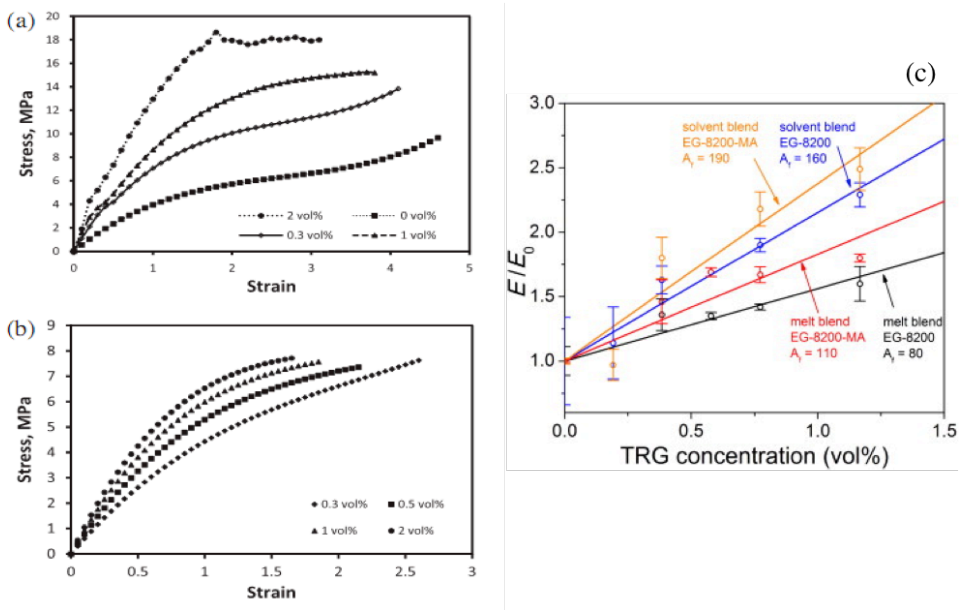

Figure 2.17 Stress-strain curves for (a) solvent blended and (b) melt blended poly(ethylene oxide)/graphene composites [87]. (c) Tensile modulus of solvent blended or melt blended composites made of thermally reduced graphene oxide (TRG)/linear low density polyethylene (EG-8200) and TRG/ linear low density polyethylene grafted with maleic anhydride (EG-8200-MA) [94].

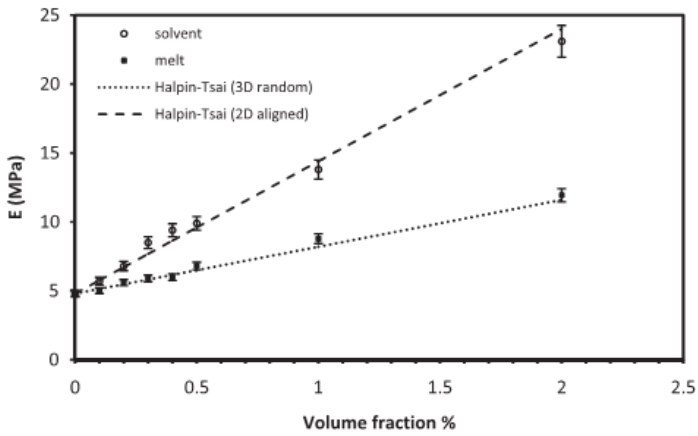

Figure 2.18 Young's modulus of poly(ethylene oxide)/graphene composites as a function of graphene volume fraction [87].

It can be clearly seen in Figure 2.18 that the modulus increases with the addition of graphene, but the enforcement is not as much as expected given the extraordinary intrinsic modulus of graphene. This difference between predicted and observed performance is probably due to the wrinkled structure of thin graphene sheets which reduces their effective modulus [95].

The mechanical properties of composites have some relationship with the fabrication methods. Mahmoud *et al.* found that that solvent compounding is more effective at enhancing the mechanical performance than melt blending and suggested that this may be due to the blending reducing the platelets aspect ratio due to filler attrition during the process (Figure 2.17 and Figure 2.18). Kim *et al.* [94] carried out a comparative study of the effects of blending methods, and found out that solvent based blending more effectively dispersed these exfoliated carbon sheets than did melt compounding. Also a higher degree of dispersion of fillers in the matrix was achieved using the solvent technique. There is evidence that, in general, nanofillers (including CNTs) which appear uniformly dispersed on a short length scale may aggregated at a larger scale, thus acting as a stress concentration, leading to weak mechanical performance [96].

The effective reinforcement of graphene may also be limited by the interfacial adhesion between fillers and matrix [97-98], which influences the stress transfer effectiveness. Incompatibility between the filler and matrix may lower stress transfer due to low interfacial force, resulting in a poor composite modulus. AFM and Raman spectroscopy are the main tools in the literature used to measure the interfacial adhesion. Due to the nearly perfect structure of pure graphene obtained by mechanical exfoliation, the interfacial adhesion between graphene and polymer is relatively low. Modification of graphene with small molecules or groups is a promising route to promote stronger interfacial adhesion, because it usually creates covalent or non-covalent bonds with the matrix.

Besides the reinforcement of modulus, improvements in fracture toughness, fatigue strength, and buckling resistance have also been reported [93, 99-100].

2.4.2 Electrical Percolation Threshold and Conductivity

Most polymers are electrically insulating, limiting their applications in many areas. Whereas graphene has an extremely high conductivity, and thus is expected to improve a polymer's bulk conductivity when incorporated into polymer matrix. Researchers suggest that one of the most promising potential applications of graphene/polymer composites is in the packaging of devices and other electronics. In order to make an insulating polymer matrix into a electrically conductive composite, the conductive fillers must form a network and the concentration of fillers must be

above a value called the electrical percolation threshold [101]. Percolation theory assumes that this network is a random, space-filling network. As shows in Figure 2.19, when the electrical percolation threshold has been achieved the conductivity usually increases by several orders and the increase in conductivity as a function of filler loading can be modeled by a simple power-law expression:

$$\sigma_c = \sigma_f(\phi - \phi_c)^t \tag{2.1}$$

where ϕ is the filler volume fraction, ϕ_c is the percolation threshold, σ_f is a proportionality constant, σ_c is the composite conductivity and t is a universal exponent ($t \geq 2$ for a randomly 3D dispersion of filler and $t < 2$ for 2D dispersion) [102].

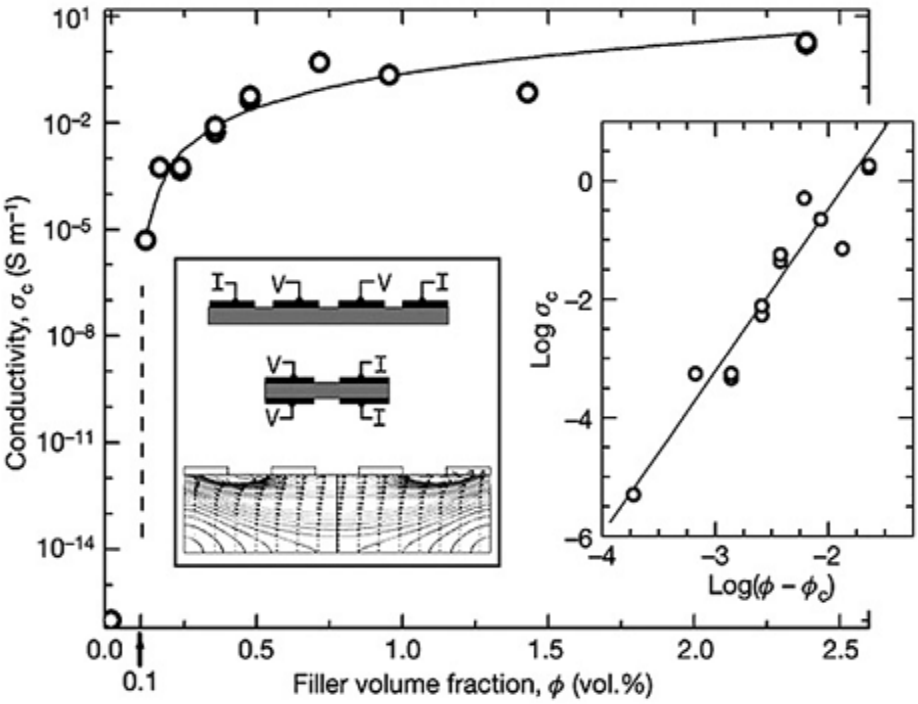

Figure 2.19 Specific conductivity of polystyrene composites filled with reduced graphene oxide functionalized by phenylisocyanate as function of filler volume fraction, and the power-law of conductivity above the percolation threshold ϕ_c [103].

Actually for the dispersed fillers, it is not necessary to connect with each other directly to form a conductive network, as current can tunnel between fillers coated with polymer, and this tunneling resistance is said to be a limitation in the composite conductivity [104].

This formation of a percolated network is found to affect the electrical, mechanical and rheological properties, with each having their own threshold. Unlike the influence on mechanical properties, uniformly dispersed fillers may not necessarily yield the lowest electrical percolation [96], as the polymer coated on the surfaces of uniformly dispersed filler particle prevents direct contact between particles. In fact, by far the lowest electrical percolation threshold achieved for a graphene/polymer composite (approximately 0.15 wt.%) was observed when the filler was not uniformly dispersed in the matrix, but rather segregated from the matrix to form a conductive network [105]. However, such aggregation may compromise the mechanical properties of the bulk composites.

In addition, the alignment of fillers also has a close relationship with the percolation threshold. When the fillers are aligned in the matrix, the percolation threshold may increase due to the decreasing contact effectiveness. When polycarbonate and thermal reduced graphene oxide (TRGO)/polyester composites were compression moulded with aligned platelets, it shows a percolation threshold about twice that of annealed samples with randomly dispersed platelets [106].

As mentioned before, the large aspect ratio of graphene is a great advantage over other fillers and that includes the area of percolation threshold. Aspect ratio is the dominant factor affecting percolation threshold and confirmed by theoretical models [107] and experiments [108]. Higher aspect ratio yields better electrical properties (lower percolation threshold). Wrinkled, broken, restacked or folded graphene conformations may also raise the electrical percolation threshold [109].

A summary of the highest electrical conductivity and ϕ_c of graphene/polymer composites from the literature is listed in Table 2.1, in comparison with the ϕ_c of CNT/ polymer composites fabricated using the same methods [110].

It is clearly shown that thermal reduced graphene oxide (TRGO) and chemically reduced graphene oxide (CRGO) are most commonly used as fillers in polymer composites, which is mainly because of their lower production price.

Table 2.1 Electrical percolation threshold (ϕ_c) and other electrical parameters of graphene/polymer composite from the literature [110].

Filler type	Matrix	ϕ_c	Highest σ	ϕ_c of CNT	ref

			(S/m)	composites	
GNP	PA12	2 wt.%		1.5wt.%	[111]
TRGO	PA6	7.5 wt.%	0.71×10^{-2}	12 wt.%	[112]
In situ CRGO	PS	0.19 vol%	72.18		[113]
In situ CRGO	PS	0.1 vol%	1		[103]
PS-graphene	PS	2.7 wt.%	10^{-4}		[114]
TRGO	PS	0.33 vol%	3.49	0.5vol%	[115]
GO	PP		0.3		[116]
TRGO	iPP	<5 wt.%	0.02	<5 wt.%	[112]
TRGO	PU	2 wt.%	0.0275		[117]
TRGO	PU	2 wt.%	0.0492		[87]
TRGO	PVDF	2 wt.%			[118]
Acid functionalized-graphene	PVDF foam	0.5 wt.%	10.16		[119]
TRGO	HDPE	1 vol%	0.01	0.15 vol%	[119]
TRGO	PC	2.5 wt.%	0.1	2.5 wt.%	[112]
TRGO	PC	1.25 wt.%			[106]
Microwave-exfoliated GO	PC	1.3 wt.%	2.5×10^{-3}		[120]
TRGO	PET	0.47 vol%	2.11		[121]
CRGO	Epoxy	0.52 vol%	10		[122]
TRGO	PMMA foam	0.6 vol%	3.11		[123]
TRGO	PLA	3 ≈ 5 wt.%			[124]
Graphene by directly sonicating and exfoliating graphite	PVC	0.6 vol%	5.8		[125]

Xie *et al.* [126] proposed that graphene is more effective in terms of improving conductivity than CNTs because of their large specific surface area. However, that is not observed experimentally when comparing electrical conductivity between graphene and CNT-based composites.

Table 2.1 shows electrical conductivity from 10^{-4} to 72 S m^{-1} for reduced graphene oxide/polymer composites and a ϕ_c ranging from 0.1 vol% to 7.5 wt.%. Stankovich *et al.* [103] has achieved the lowest ϕ_c (0.1 vol% *in-situ* CRGO). However, it is still much higher than for CNT/ epoxy composites with a percolation of 0.0025 wt.% [127].

Some factors may shed light on these results. Firstly, graphene, as a thin 2D filler, is easier to aggregate than MWCNTs due to its larger surface area and plane-to-plane attractive forces. Secondly, the 2D structure is apt to wrinkle, and even roll into a tube-like structure, resulting in a lower aspect ratio. Finally, for 2D graphene it is more difficult to form a conductive network than for 1D CNTs. Therefore, in order to make the most out of graphene extraordinary properties, an effective fabrication method to avoid graphene rolling, keeping them flat and preventing them from restacking should be proposed.

2.4.3 Thermal Conductivity

With the progress of miniaturization in device components, the problem associated with heat transfer in the electronics has aggravated, bringing an urgent need for improved thermal interface materials (TIMs). Current TIMs are mainly polymer or grease composites with thermally conductive particles such as alumina or silver, requiring very high vol.% of filler to achieve thermal conductivity values of 1−5 W $m^{-1}K^{-1}$ which will reduce their mechanical performance. A number of nano-materials have been developed as candidates to improve the thermal conductivity of polymer composites, especially carbon based materials, like CNTs have emerged as an efficient filler due to their exceptional thermal conductivity (~ 3000 W $m^{-1}K^{-1}$ along the tube axis) and high aspect ratio [128]. However, the production cost of CNTs is a limiting factor for their industrial applications. Compared with CNTs, the graphene not only has similar intrinsic thermal conductivity but is more importantly, very cost-effective. Furthermore, the sheet-like geometry of graphene materials may lead to lower interfacial thermal resistance, improving thermal conductivity more than CNTs in polymer composites [129].

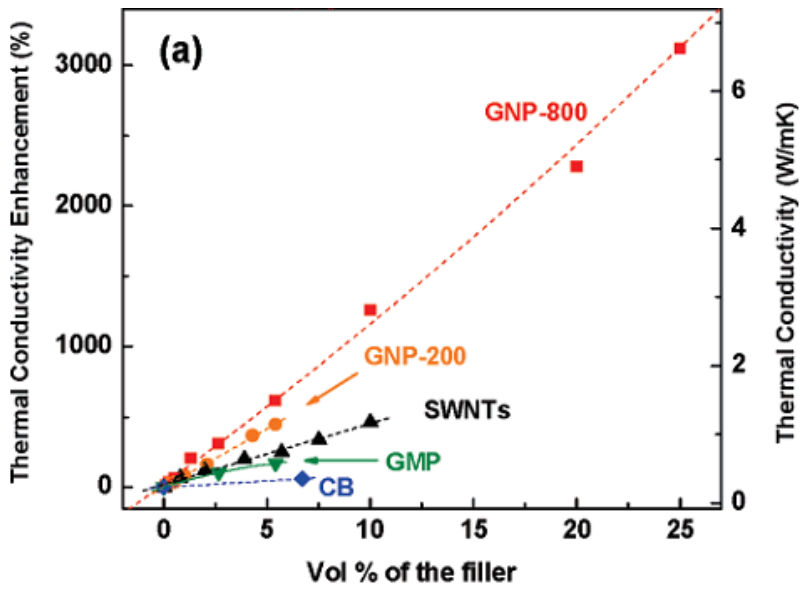

Figure 2.20 Thermal conductivity increment of epoxy-based composites. Graphitic fillers: graphitic micro particles (GMP), graphene nanoplatelet (GNP) exfoliated at 200 °C (GNP-200) and 800 °C (GNP-800), carbon black (CB), and purified single wall carbon nanotubes (SWNTs) [128].

The factors affecting thermal conductivity are similar to those of electrical conduction. Direct contact of fillers reduces thermal resistance, increasing thermal conductivity. Thermal conductivity in composites has been modeled with percolation theory [130]. Since phonons are the primary mode of thermal conduction in polymer composites, bonding between fillers and matrix will promote higher thermal conductivity, like covalent bonding [131]. Functionalization of graphene to improve bonding with the matrix is a promising route, but like electrical conduction, the functionalised group may compromise the intrinsic thermal conductivity of graphene.

Literature shows that the method of preparation has a significant impact on the resultant filler dispersion, leading to different thermal conductivity of the final composite. Chandrasekaran *et al.* [132] reported on epoxy/graphene nanoplatelets composites fabricated by three-roll milling and sonication combined with high speed shear mixing. The conductivity of their composites increased only slightly above the pure matrix, considering the high thermal conductivity of fillers. The percentage of increase in thermal conductivity was only 11 % for 1.0 wt.% and 14 % for 2.0 wt.% filler loading. No thermal conductivity percolation was observed for these samples. While Shtein *et al.*[133] demonstrated a significant enhancement of thermal conductivity from 0.2 W $m^{-1}K^{-1}$ for neat epoxy to 12.4 W $m^{-1}K^{-1}$ for 25 vol.% filler

loading composites (Figure 2.21). This thermal conductivity value corresponds to a 6800 % enhancement over the neat polymer, an outstanding value for filler compared to traditional filers. This ultrahigh increase was achieved by using GNPs with large lateral dimensions and low defect densities and applying a high compression forces during the dispersion to bring adjacent particle together.

Apart from increasing thermal conductivity of a polymer matrix, graphene fillers also can improve composite thermal stability, confirmed by a significant number of reports [16,134-136].

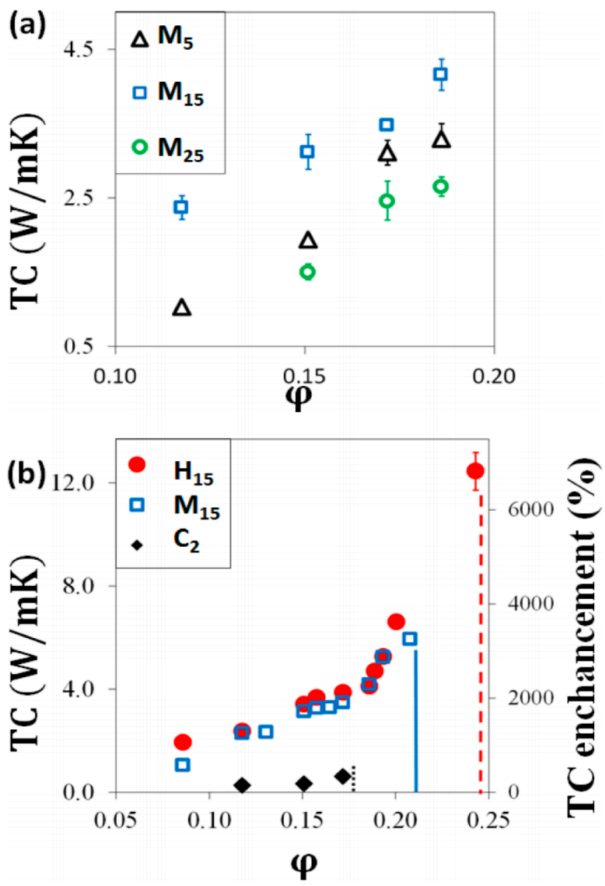

Figure 2.21 Thermal conductivity of epoxy/graphene nanoplatelets (GNP) composite as a function of (a) GNP lateral dimension and loading (φ), (b) GNP grade (H_{15}, M_{15} and C_2) and φ [133].

2.4.4 Gas Barrier Properties

The incorporation of graphene nanosheets can significantly reduce gas permeation through a polymer composite compared with the neat matrix polymer.

When a network of graphene forms in the matrix, it can largely decrease gas permeation by a mechanism of the "tortuous path", which slows molecular diffusion in a way shown in Figure 2.22 [98].

As can be seen from Figure 2.22, the orientation of the graphene platelets plays an important role in gas barrier function. Well-aligned graphene nanosheets may further enhance barrier properties in the perpendicular direction, while higher aspect ratios of platelet leads to increased barrier resistance [98].

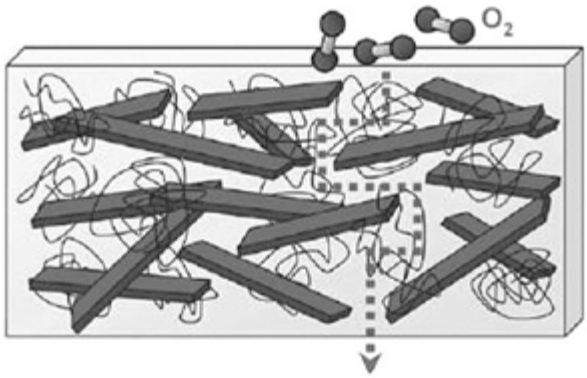

Figure 2.22 Illustration of formation of a 'tortuous path' of platelets inhibiting diffusion of gases through a polymer composite (Nielson model). Adapted from [98].

2.4.5 Water Uptake of Polymer Matrix Composites

Polymer carbon composites, used as structure materials, usually have a high possibility to be exposed to various environments involving high temperature and humidity. Much research has been conducted to study the effects of water absorption on the physical and chemical properties of polymer composites. Most of the results showed that both the physical and mechanical properties of composite materials can be strongly affected by hydrothermal ageing, affecting the composite performance in service [137].

Water absorption in polymer-matrix composites can cause plasticization of the polymeric matrix leading to a significant reduction of the glass-transition temperature (T_g) [138]. Apart from that, water absorbed can seriously affect the fiber–matrix interfacial interaction, causing polymer degradation [139], with a concurrent swelling

and lowering of T_g [140]. It has been proposed [141] that the transport of moisture below the T_g comprises of three stages :

i. Diffusion of water through the bulk of the polymer network.
ii. Absorption of moisture on the surface of vacuoles that define the excess free volume of the glassy structure.
iii. Through hydrogen bond formation between hydrophilic groups associated with hydroxyl or amine groups attached to the polymer chain and the water molecules.

There are many factors affecting the way composite materials absorb moisture, including temperature, filler volume fraction, reinforcement orientation, filler nature (that is, permeability, polarity, density), area of exposed surfaces, diffusivity, and surface protection [134].

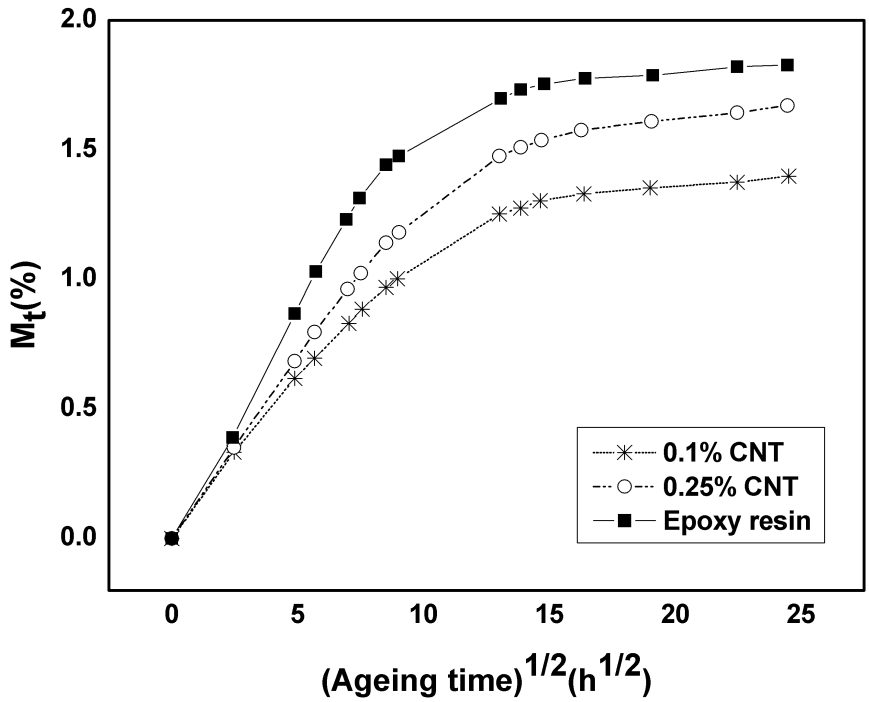

Figure 2.23 Water uptake behaviour of epoxy resin and nano-composites reinforced with CNTs [140].

Carbon nanofillers, due to their hydrophobic properties and barrier effect in a polymer matrix, are expected to reduce the water absorption after addition to a polymer matrix. Prolongo *et al.* [142] reported that carbon nanotubes can significantly decrease the water absorption and water diffusion coefficient by 20-30 % (Figure 2.23).

This decrease is higher than expected for composites reinforced with CNT due its 1D nature. The author reasoned that this could be associated with the barrier properties of nanofillers in epoxy matrix [143], which form tortuous paths, hindering the water progress and decreasing the diffusion rate. At higher filler loading, the enhancement of their hydrothermal ageing behaviour decreased, which was related to the aggregation of the fillers in the matrix, introducing micro-scale voids for water molecules. However, there is also research [140] which showed that the water uptake was increased after adding carbon filler. It found that the higher the wt.% CNT content, the higher the water uptake. This supports the reasoning that the addition of CNTs into an epoxy matrix leads to an increased interfacial region, serving as a route for higher water uptake.

It is expected that the incorporation of graphene nanoplatelets will decrease the water uptake considering the hydrophobic nature of GNP surface that tends to immobilize some of the moisture, which inhibits the water permeation into the polymer matrix [144].

Various models have been proposed to describe the kinetics of water diffusion. Most favoured treatments are based on Fick's law. According to the Fickian diffusion law, the diffusion coefficients are easily calculated from the moisture-uptake profiles with Fick's second law:

$$\frac{M_t}{M_\infty} = 1 - \sum_{n=0}^{\infty} \frac{8}{(2n+1)^2\pi^2} \exp\left[\frac{-D(2n+1)^2\pi^2 t}{4L^2}\right] \tag{2.2}$$

where M_t is the water absorption at time t, M_∞ is the equilibrium water absorption, L is the sample thickness, and D is the diffusion coefficient. At very short times, where M_t / M_∞ is less than 0.5; Eq. (3) can be approximated as follows:

$$\frac{M_t}{M_\infty} = \frac{4}{L}\sqrt{\frac{Dt}{\pi}} \tag{2.3}$$

This equation is derived under the assumption that the diffusion coefficient D is a constant and is easily rearranged to reveal that the initial slope in a plot about the percentage water uptake M_t versus $\sqrt{t}$ curve:

$$D = \frac{\pi}{16}\left(\frac{L}{M_\infty}\right)^2\left(\frac{M_{t2}-M_{t1}}{\sqrt{t_2}-\sqrt{t_1}}\right)^2 \tag{2.4}$$

From Figure 2.23, water uptake is linearly proportional to $\sqrt{t}$ at the initial stage. Using the equilibrium-uptake data and Eq. (4), the diffusion coefficients D are determined from the slope of the initial linear portion of the water uptake curve.

References

1. Geim, A. K.; Novoselov, K. S., The rise of graphene. *Nat Mater* **2007,** *6* (3), 183-191.
2. Young, R. J.; Kinloch, I. A.; Gong, L.; Novoselov, K. S., The mechanics of graphene nano-composites: A review. *Composites Science and Technology* **2012,** *72* (12), 1459-1476.
3. Novoselov, K. S.; Geim, A. K.; Morozov, S. V.; Jiang, D.; Zhang, Y.; Dubonos, S. V.; Grigorieva, I. V.; Firsov, A. A., Electric Field Effect in Atomically Thin Carbon Films. *Science* **2004,** *306* (5696), 666-669.
4. Ohta, T.; Bostwick, A.; Seyller, T.; Horn, K.; Rotenberg, E., Controlling the Electronic Structure of Bilayer Graphene. *Science* **2006,** *313* (5789), 951-954.
5. Bolotin, K. I.; Sikes, K. J.; Jiang, Z.; Klima, M.; Fudenberg, G.; Hone, J.; Kim, P.; Stormer, H. L., Ultrahigh electron mobility in suspended graphene. *Solid State Communications* **2008,** *146* (9–10), 351-355.
6. Novoselov, K. S.; Jiang, Z.; Zhang, Y.; Morozov, S. V.; Stormer, H. L.; Zeitler, U.; Maan, J. C.; Boebinger, G. S.; Kim, P.; Geim, A. K., Room-Temperature Quantum Hall Effect in Graphene. *Science* **2007,** *315* (5817), 1379-1379.
7. Lee, C.; Wei, X.; Kysar, J. W.; Hone, J., Measurement of the Elastic Properties and Intrinsic Strength of Monolayer Graphene. *Science* **2008,** *321* (5887), 385-388.
8. Liu, F.; Ming, P.; Li, J., Ab calculation of ideal strength and phonon instability of graphene under tension. *Physical Review B* **2007,** *76* (6), 064120.
9. Li, X.; Wang, X.; Zhang, L.; Lee, S.; Dai, H., Chemically Derived, Ultrasmooth Graphene Nanoribbon Semiconductors. *Science* **2008,** *319* (5867), 1229-1232.
10. Wang, G.; Yang, J.; Park, J.; Gou, X.; Wang, B.; Liu, H.; Yao, J., Facile Synthesis and Characterization of Graphene Nanosheets. *The Journal of Physical Chemistry C* **2008,** *112* (22), 8192-8195.
11. Blake, P.; Brimicombe, P. D.; Nair, R. R.; Booth, T. J.; Jiang, D.; Schedin, F.; Ponomarenko, L. A.; Morozov, S. V.; Gleeson, H. F.; Hill, E. W.; Geim, A. K.; Novoselov, K. S., Graphene-Based Liquid Crystal Device. *Nano Letters* **2008,** *8* (6), 1704-1708.
12. Dreyer, D. R.; Park, S.; Bielawski, C. W.; Ruoff, R. S., The chemistry of graphene oxide. *Chemical Society Reviews* **2010,** *39* (1), 228-240.
13. Wang, G.; Shen, X.; Wang, B.; Yao, J.; Park, J., Synthesis and characterisation of hydrophilic and organophilic graphene nanosheets. *Carbon* **2009,** *47* (5), 1359-1364.

14. Choi, W.; Lahiri, I.; Seelaboyina, R.; Kang, Y. S., Synthesis of Graphene and Its Applications: A Review. *Critical Reviews in Solid State and Materials Sciences* **2010,** *35* (1), 52-71.
15. Kuila, T.; Bose, S.; Mishra, A. K.; Khanra, P.; Kim, N. H.; Lee, J. H., Chemical functionalization of graphene and its applications. *Progress in Materials Science* **2012,** *57* (7), 1061-1105.
16. Kuilla, T.; Bhadra, S.; Yao, D.; Kim, N. H.; Bose, S.; Lee, J. H., Recent advances in graphene based polymer composites. *Progress in Polymer Science* **2010,** *35* (11), 1350-1375.
17. Vallés, C.; Drummond, C.; Saadaoui, H.; Furtado, C. A.; He, M.; Roubeau, O.; Ortolani, L.; Monthioux, M.; Pénicaud, A., Solutions of Negatively Charged Graphene Sheets and Ribbons. *Journal of the American Chemical Society* **2008,** *130* (47), 15802-15804.
18. Eizenberg, M.; Blakely, J. M., Carbon monolayer phase condensation on Ni(111). *Surface Science* **1979,** *82* (1), 228-236.
19. Dubin, S.; Gilje, S.; Wang, K.; Tung, V. C.; Cha, K.; Hall, A. S.; Farrar, J.; Varshneya, R.; Yang, Y.; Kaner, R. B., A One-Step, Solvothermal Reduction Method for Producing Reduced Graphene Oxide Dispersions in Organic Solvents. *ACS Nano* **2010,** *4* (7), 3845-3852.
20. Chen, W.; Yan, L.; Bangal, P. R., Chemical Reduction of Graphene Oxide to Graphene by Sulfur-Containing Compounds. *The Journal of Physical Chemistry C* **2010,** *114* (47), 19885-19890.
21. Ramesha, G. K.; Sampath, S., Electrochemical Reduction of Oriented Graphene Oxide Films: An in Situ Raman Spectroelectrochemical Study. *The Journal of Physical Chemistry C* **2009,** *113* (19), 7985-7989.
22. Akhavan, O.; Ghaderi, E., Photocatalytic Reduction of Graphene Oxide Nanosheets on TiO2 Thin Film for Photoinactivation of Bacteria in Solar Light Irradiation. *The Journal of Physical Chemistry C* **2009,** *113* (47), 20214-20220.
23. Shao, Y.; Wang, J.; Engelhard, M.; Wang, C.; Lin, Y., Facile and controllable electrochemical reduction of graphene oxide and its applications. *Journal of Materials Chemistry* **2010,** *20* (4), 743-748.
24. Shin, H.-J.; Kim, K. K.; Benayad, A.; Yoon, S.-M.; Park, H. K.; Jung, I.-S.; Jin, M. H.; Jeong, H.-K.; Kim, J. M.; Choi, J.-Y.; Lee, Y. H., Efficient Reduction of Graphite Oxide by Sodium Borohydride and Its Effect on Electrical Conductance. *Advanced Functional Materials* **2009,** *19* (12), 1987-1992.
25. Abdelkader, A. M.; Vallés, C.; Cooper, A. J.; Kinloch, I. A.; Dryfe, R. A. W., Alkali Reduction of Graphene Oxide in Molten Halide Salts: Production of Corrugated Graphene Derivatives for High-Performance Supercapacitors. *ACS Nano* **2014,** *8* (11), 11225-11233.
26. Abdelkader, A. M.; Cooper, A. J.; Dryfe, R. A. W.; Kinloch, I. A., How to get between the sheets: a review of recent works on the electrochemical exfoliation of graphene materials from bulk graphite. *Nanoscale* **2015,** *7* (16), 6944-6956.
27. Stankovich, S.; Dikin, D. A.; Piner, R. D.; Kohlhaas, K. A.; Kleinhammes, A.; Jia, Y.; Wu, Y.; Nguyen, S. T.; Ruoff, R. S., Synthesis of graphene-based nanosheets via chemical reduction of exfoliated graphite oxide. *Carbon* **2007,** *45* (7), 1558-1565.

28. Geng, Y.; Wang, S. J.; Kim, J.-K., Preparation of graphite nanoplatelets and graphene sheets. *Journal of Colloid and Interface Science* **2009,** *336* (2), 592-598.
29. Wei, T.; Luo, G.; Fan, Z.; Zheng, C.; Yan, J.; Yao, C.; Li, W.; Zhang, C., Preparation of graphene nanosheet/polymer composites using in situ reduction–extractive dispersion. *Carbon* **2009,** *47* (9), 2296-2299.
30. Novoselov, K. S.; Falko, V. I.; Colombo, L.; Gellert, P. R.; Schwab, M. G.; Kim, K., A roadmap for graphene. *Nature* **2012,** *490* (7419), 192-200.
31. Gao, W.; Alemany, L. B.; Ci, L.; Ajayan, P. M., New insights into the structure and reduction of graphite oxide. *Nat Chem* **2009,** *1* (5), 403-408.
32. Paredes, J. I.; Villar-Rodil, S.; Martínez-Alonso, A.; Tascón, J. M. D., Graphene Oxide Dispersions in Organic Solvents. *Langmuir* **2008,** *24* (19), 10560-10564.
33. Lerf, A.; He, H.; Forster, M.; Klinowski, J., Structure of Graphite Oxide Revisited. *The Journal of Physical Chemistry B* **1998,** *102* (23), 4477-4482.
34. Nethravathi, C.; Rajamathi, J. T.; Ravishankar, N.; Shivakumara, C.; Rajamathi, M., Graphite Oxide-Intercalated Anionic Clay and Its Decomposition to Graphene–Inorganic Material Nano-composites. *Langmuir* **2008,** *24* (15), 8240-8244.
35. Niyogi, S.; Bekyarova, E.; Itkis, M. E.; McWilliams, J. L.; Hamon, M. A.; Haddon, R. C., Solution Properties of Graphite and Graphene. *Journal of the American Chemical Society* **2006,** *128* (24), 7720-7721.
36. Liu, Z.-B.; Xu, Y.-F.; Zhang, X.-Y.; Zhang, X.-L.; Chen, Y.-S.; Tian, J.-G., Porphyrin and Fullerene Covalently Functionalized Graphene Hybrid Materials with Large Nonlinear Optical Properties. *The Journal of Physical Chemistry B* **2009,** *113* (29), 9681-9686.
37. Wang, S.; Chia, P.-J.; Chua, L.-L.; Zhao, L.-H.; Png, R.-Q.; Sivaramakrishnan, S.; Zhou, M.; Goh, R. G. S.; Friend, R. H.; Wee, A. T. S.; Ho, P. K. H., Band-like Transport in Surface-Functionalized Highly Solution-Processable Graphene Nanosheets. *Advanced Materials* **2008,** *20* (18), 3440-3446.
38. Yang, H.; Shan, C.; Li, F.; Han, D.; Zhang, Q.; Niu, L., Covalent functionalization of polydisperse chemically-converted graphene sheets with amine-terminated ionic liquid. *Chemical Communications* **2009,** (26), 3880-3882.
39. Wajid, A. S.; Das, S.; Irin, F.; Ahmed, H. S. T.; Shelburne, J. L.; Parviz, D.; Fullerton, R. J.; Jankowski, A. F.; Hedden, R. C.; Green, M. J., Polymer-stabilized graphene dispersions at high concentrations in organic solvents for composite production. *Carbon* **2012,** *50* (2), 526-534.
40. Lu, C.-H.; Yang, H.-H.; Zhu, C.-L.; Chen, X.; Chen, G.-N., A Graphene Platform for Sensing Biomolecules. *Angewandte Chemie International Edition* **2009,** *48* (26), 4785-4787.
41. Yang, X.; Zhang, X.; Liu, Z.; Ma, Y.; Huang, Y.; Chen, Y., High-Efficiency Loading and Controlled Release of Doxorubicin Hydrochloride on Graphene Oxide. *The Journal of Physical Chemistry C* **2008,** *112* (45), 17554-17558.
42. Stankovich, S.; Piner, R. D.; Nguyen, S. T.; Ruoff, R. S., Synthesis and exfoliation of isocyanate-treated graphene oxide nanoplatelets. *Carbon* **2006,** *44* (15), 3342-3347.

43. Xu, Y.; Bai, H.; Lu, G.; Li, C.; Shi, G., Flexible Graphene Films via the Filtration of Water-Soluble Noncovalent Functionalized Graphene Sheets. *Journal of the American Chemical Society* **2008,** *130* (18), 5856-5857.
44. Panchakarla, L. S.; Govindaraj, A., Covalent and non-covalent functionalization and solubilization of double-walled carbon nanotubes in nonpolar and aqueous media. *Journal of Chemical Sciences* **2008,** *120* (6), 607-611.
45. Stankovich, S.; Piner, R. D.; Chen, X.; Wu, N.; Nguyen, S. T.; Ruoff, R. S., Stable aqueous dispersions of graphitic nanoplatelets via the reduction of exfoliated graphite oxide in the presence of poly(sodium 4-styrenesulfonate). *Journal of Materials Chemistry* **2006,** *16* (2), 155-158.
46. Salavagione, H. J.; Martínez, G.; Ellis, G., Recent Advances in the Covalent Modification of Graphene With Polymers. *Macromolecular Rapid Communications* **2011,** *32* (22), 1771-1789.
47. Shan, C.; Yang, H.; Han, D.; Zhang, Q.; Ivaska, A.; Niu, L., Water-Soluble Graphene Covalently Functionalized by Biocompatible Poly-l-lysine. *Langmuir* **2009,** *25* (20), 12030-12033.
48. Loh, K. P.; Bao, Q.; Ang, P. K.; Yang, J., The chemistry of graphene. *Journal of Materials Chemistry* **2010,** *20* (12), 2277-2289.
49. Zhu, Y.; Murali, S.; Cai, W.; Li, X.; Suk, J. W.; Potts, J. R.; Ruoff, R. S., Graphene and Graphene Oxide: Synthesis, Properties, and Applications. *Advanced Materials* **2010,** *22* (35), 3906-3924.
50. Yan, L.; Zheng, Y. B.; Zhao, F.; Li, S.; Gao, X.; Xu, B.; Weiss, P. S.; Zhao, Y., Chemistry and physics of a single atomic layer: strategies and challenges for functionalization of graphene and graphene-based materials. *Chemical Society Reviews* **2012,** *41* (1), 97-114.
51. Wang, X.; Xing, W.; Zhang, P.; Song, L.; Yang, H.; Hu, Y., Covalent functionalization of graphene with organosilane and its use as a reinforcement in epoxy composites. *Composites Science and Technology* **2012,** *72* (6), 737-743.
52. Cui, Y.; Kim, S. N.; Jones, S. E.; Wissler, L. L.; Naik, R. R.; McAlpine, M. C., Chemical Functionalization of Graphene Enabled by Phage Displayed Peptides. *Nano Letters* **2010,** *10* (11), 4559-4565.
53. Tapas, K.; Partha, K.; Saswata, B.; Nam Hoon, K.; Bon-Cheol, K.; Bongho, M.; Joong Hee, L., Preparation of water-dispersible graphene by facile surface modification of graphite oxide. *Nanotechnology* **2011,** *22* (30), 305710.
54. Hossain, M. Z.; Walsh, M. A.; Hersam, M. C., Scanning Tunneling Microscopy, Spectroscopy, and Nanolithography of Epitaxial Graphene Chemically Modified with Aryl Moieties. *Journal of the American Chemical Society* **2010,** *132* (43), 15399-15403.
55. Sharma, R.; Baik, J. H.; Perera, C. J.; Strano, M. S., Anomalously Large Reactivity of Single Graphene Layers and Edges toward Electron Transfer Chemistries. *Nano Letters* **2010,** *10* (2), 398-405.
56. Bekyarova, E.; Itkis, M. E.; Ramesh, P.; Berger, C.; Sprinkle, M.; de Heer, W. A.; Haddon, R. C., Chemical Modification of Epitaxial Graphene: Spontaneous Grafting of Aryl Groups. *Journal of the American Chemical Society* **2009,** *131* (4), 1336-1337.

57. Mann, J. A.; Dichtel, W. R., Noncovalent Functionalization of Graphene by Molecular and Polymeric Adsorbates. *The Journal of Physical Chemistry Letters* **2013,** *4* (16), 2649-2657.
58. Georgakilas, V.; Otyepka, M.; Bourlinos, A. B.; Chandra, V.; Kim, N.; Kemp, K. C.; Hobza, P.; Zboril, R.; Kim, K. S., Functionalization of Graphene: Covalent and Non-Covalent Approaches, Derivatives and Applications. *Chemical Reviews* **2012,** *112* (11), 6156-6214.
59. Burley, S. K.; Petsko, G. A., Aromatic-aromatic interaction: a mechanism of protein structure stabilization. *Science* **1985,** *229* (4708), 23-28.
60. Meyer, E. A.; Castellano, R. K.; Diederich, F., Interactions with Aromatic Rings in Chemical and Biological Recognition. *Angewandte Chemie International Edition* **2003,** *42* (11), 1210-1250.
61. Hong, B. H.; Lee, J. Y.; Lee, C.-W.; Kim, J. C.; Bae, S. C.; Kim, K. S., Self-Assembled Arrays of Organic Nanotubes with Infinitely Long One-Dimensional H-Bond Chains. *Journal of the American Chemical Society* **2001,** *123* (43), 10748-10749.
62. Singh, N. J.; Lee, H. M.; Hwang, I.-C.; Kim, K. S., Designing Ionophores and Molecular Nanotubes Based on Molecular Recognition. *Supramolecular Chemistry* **2007,** *19* (4-5), 321-332.
63. Lee, J. Y.; Hong, B. H.; Kim, W. Y.; Min, S. K.; Kim, Y.; Jouravlev, M. V.; Bose, R.; Kim, K. S.; Hwang, I.-C.; Kaufman, L. J.; Wong, C. W.; Kim, P.; Kim, K. S., Near-field focusing and magnification through self-assembled nanoscale spherical lenses. *Nature* **2009,** *460* (7254), 498-501.
64. Wang, Y.; Chen, X.; Zhong, Y.; Zhu, F.; Loh, K. P., Large area, continuous, few-layered graphene as anodes in organic photovoltaic devices. *Applied Physics Letters* **2009,** *95* (6), 063302.
65. Kodali, V. K.; Scrimgeour, J.; Kim, S.; Hankinson, J. H.; Carroll, K. M.; de Heer, W. A.; Berger, C.; Curtis, J. E., Nonperturbative Chemical Modification of Graphene for Protein Micropatterning. *Langmuir* **2011,** *27* (3), 863-865.
66. Lopes, M.; Candini, A.; Urdampilleta, M.; Reserbat-Plantey, A.; Bellini, V.; Klyatskaya, S.; Marty, L.; Ruben, M.; Affronte, M.; Wernsdorfer, W.; Bendiab, N., Surface-Enhanced Raman Signal for Terbium Single-Molecule Magnets Grafted on Graphene. *ACS Nano* **2010,** *4* (12), 7531-7537.
67. Cheng, H.-C.; Shiue, R.-J.; Tsai, C.-C.; Wang, W.-H.; Chen, Y.-T., High-Quality Graphene p−n Junctions via Resist-free Fabrication and Solution-Based Noncovalent Functionalization. *ACS Nano* **2011,** *5* (3), 2051-2059.
68. Wang, X.; Tabakman, S. M.; Dai, H., Atomic Layer Deposition of Metal Oxides on Pristine and Functionalized Graphene. *Journal of the American Chemical Society* **2008,** *130* (26), 8152-8153.
69. Pimenta, M. A.; Dresselhaus, G.; Dresselhaus, M. S.; Cancado, L. G.; Jorio, A.; Saito, R., Studying disorder in graphite-based systems by Raman spectroscopy. *Physical Chemistry Chemical Physics* **2007,** *9* (11), 1276-1290.
70. Castro Neto, A. H.; Guinea, F.; Peres, N. M. R.; Novoselov, K. S.; Geim, A. K., The electronic properties of graphene. *Reviews of Modern Physics* **2009,** *81* (1), 109-162.
71. Ni, Z.; Wang, Y.; Yu, T.; Shen, Z., Raman spectroscopy and imaging of graphene. *Nano Research* **2008,** *1* (4), 273-291.

72. Reina, A.; Jia, X.; Ho, J.; Nezich, D.; Son, H.; Bulovic, V.; Dresselhaus, M. S.; Kong, J., Large Area, Few-Layer Graphene Films on Arbitrary Substrates by Chemical Vapor Deposition. *Nano Letters* **2009,** *9* (1), 30-35.
73. Sun, Z.; Yan, Z.; Yao, J.; Beitler, E.; Zhu, Y.; Tour, J. M., Growth of graphene from solid carbon sources. *Nature* **2011,** *471* (7336), 124-124.
74. Wang, Y. y.; Ni, Z. h.; Yu, T.; Shen, Z. X.; Wang, H. m.; Wu, Y. h.; Chen, W.; Shen Wee, A. T., Raman Studies of Monolayer Graphene: The Substrate Effect. *The Journal of Physical Chemistry C* **2008,** *112* (29), 10637-10640.
75. Ferrari, A. C.; Meyer, J. C.; Scardaci, V.; Casiraghi, C.; Lazzeri, M.; Mauri, F.; Piscanec, S.; Jiang, D.; Novoselov, K. S.; Roth, S.; Geim, A. K., Raman Spectrum of Graphene and Graphene Layers. *Physical Review Letters* **2006,** *97* (18), 187401.
76. Gong, L.; Kinloch, I. A.; Young, R. J.; Riaz, I.; Jalil, R.; Novoselov, K. S., Interfacial Stress Transfer in a Graphene Monolayer Nano-composite. *Advanced Materials* **2010,** *22* (24), 2694-2697.
77. Mohiuddin, T. M. G.; Lombardo, A.; Nair, R. R.; Bonetti, A.; Savini, G.; Jalil, R.; Bonini, N.; Basko, D. M.; Galiotis, C.; Marzari, N.; Novoselov, K. S.; Geim, A. K.; Ferrari, A. C., Uniaxial strain in graphene by Raman spectroscopy: G peak splitting, Gr\"uneisen parameters, and sample orientation. *Physical Review B* **2009,** *79* (20), 205433.
78. Huang, M.; Yan, H.; Chen, C.; Song, D.; Heinz, T. F.; Hone, J., Phonon softening and crystallographic orientation of strained graphene studied by Raman spectroscopy. *Proceedings of the National Academy of Sciences* **2009,** *106* (18), 7304-7308.
79. Gong, L., Deformation Micromechanics of Graphene Nano-composites. PhD Thesis, The University of Manchester, **2013**.
80. Metzger, C.; Rémi, S.; Liu, M.; Kusminskiy, S. V.; Castro Neto, A. H.; Swan, A. K.; Goldberg, B. B., Biaxial Strain in Graphene Adhered to Shallow Depressions. *Nano Letters* **2010,** *10* (1), 6-10.
81. Chen, C.-C.; Bao, W.; Theiss, J.; Dames, C.; Lau, C. N.; Cronin, S. B., Raman Spectroscopy of Ripple Formation in Suspended Graphene. *Nano Letters* **2009,** *9* (12), 4172-4176.
82. Sutter, P.; Sadowski, J. T.; Sutter, E., Graphene on Pt(111): Growth and substrate interaction. *Physical Review B* **2009,** *80* (24), 245411.
83. Ni, Z. H.; Yu, T.; Lu, Y. H.; Wang, Y. Y.; Feng, Y. P.; Shen, Z. X., Uniaxial Strain on Graphene: Raman Spectroscopy Study and Band-Gap Opening. *ACS Nano* **2008,** *2* (11), 2301-2305.
84. Li, Z.; Young, R. J.; Kinloch, I. A.; Wilson, N. R.; Marsden, A. J.; Raju, A. P. A., Quantitative determination of the spatial orientation of graphene by polarized Raman spectroscopy. *Carbon* **2015,** *88*, 215-224.
85. Si, Y.; Samulski, E. T., Synthesis of Water Soluble Graphene. *Nano Letters* **2008,** *8* (6), 1679-1682.
86. Datta, S. S.; Strachan, D. R.; Mele, E. J.; Johnson, A. T. C., Surface Potentials and Layer Charge Distributions in Few-Layer Graphene Films. *Nano Letters* **2009,** *9* (1), 7-11.
87. Mahmoud, W. E., Morphology and physical properties of poly(ethylene oxide) loaded graphene nano-composites prepared by two different techniques. *European Polymer Journal* **2011,** *47* (8), 1534-1540.

88. Hernandez, Y.; Nicolosi, V.; Lotya, M.; Blighe, F. M.; Sun, Z.; De, S.; McGovern, I. T.; Holland, B.; Byrne, M.; Gun'Ko, Y. K.; Boland, J. J.; Niraj, P.; Duesberg, G.; Krishnamurthy, S.; Goodhue, R.; Hutchison, J.; Scardaci, V.; Ferrari, A. C.; Coleman, J. N., High-yield production of graphene by liquid-phase exfoliation of graphite. *Nat Nano* **2008,** *3* (9), 563-568.
89. Song, F. Q.; Li, Z. Y.; Wang, Z. W.; He, L.; Han, M.; Wang, G. H., Free-standing graphene by scanning transmission electron microscopy. *Ultramicroscopy* **2010,** *110* (12), 1460-1464.
90. Jang, B. Z.; Zhamu, A., Processing of nanographene platelets (NGPs) and NGP nano-composites: a review. *Journal of Materials Science* **2008,** *43* (15), 5092-5101.
91. Potts, J. R.; Lee, S. H.; Alam, T. M.; An, J.; Stoller, M. D.; Piner, R. D.; Ruoff, R. S., Thermomechanical properties of chemically modified graphene/poly(methyl methacrylate) composites made by in situ polymerization. *Carbon* **2011,** *49* (8), 2615-2623.
92. Wang, W.-P.; Pan, C.-Y., Preparation and characterization of polystyrene/graphite composite prepared by cationic grafting polymerization. *Polymer* **2004,** *45* (12), 3987-3995.
93. Rafiee, M. A.; Rafiee, J.; Wang, Z.; Song, H.; Yu, Z.-Z.; Koratkar, N., Enhanced Mechanical Properties of Nano-composites at Low Graphene Content. *ACS Nano* **2009,** *3* (12), 3884-3890.
94. Kim, H.; Kobayashi, S.; AbdurRahim, M. A.; Zhang, M. J.; Khusainova, A.; Hillmyer, M. A.; Abdala, A. A.; Macosko, C. W., Graphene/polyethylene nano-composites: Effect of polyethylene functionalization and blending methods. *Polymer* **2011,** *52* (8), 1837-1846.
95. Wakabayashi, K.; Pierre, C.; Dikin, D. A.; Ruoff, R. S.; Ramanathan, T.; Brinson, L. C.; Torkelson, J. M., Polymer−Graphite Nano-composites: Effective Dispersion and Major Property Enhancement via Solid-State Shear Pulverization. *Macromolecules* **2008,** *41* (6), 1905-1908.
96. Schaefer, D. W.; Justice, R. S., How Nano Are Nano-composites? *Macromolecules* **2007,** *40* (24), 8501-8517.
97. Klüppel, M., The Role of Disorder in Filler Reinforcement of Elastomers on Various Length Scales. In *Filler-Reinforced Elastomers/Scanning Force Microscopy*, Capella, B.; Geuss, M.; Klüppel, M.; Munz, M.; Schulz, E.; Sturm, H., Eds. Springer Berlin Heidelberg: 2003; Vol. 164, pp 1-86.
98. Paul, D. R.; Robeson, L. M., Polymer nanotechnology: Nano-composites. *Polymer* **2008,** *49* (15), 3187-3204.
99. Fang, M.; Zhang, Z.; Li, J.; Zhang, H.; Lu, H.; Yang, Y., Constructing hierarchically structured interphases for strong and tough epoxy nano-composites by amine-rich graphene surfaces. *Journal of Materials Chemistry* **2010,** *20* (43), 9635-9643.
100. Rafiee, M. A.; Rafiee, J.; Srivastava, I.; Wang, Z.; Song, H.; Yu, Z.-Z.; Koratkar, N., Fracture and Fatigue in Graphene Nano-composites. *Small* **2010,** *6* (2), 179-183.
101. Balogun, Y. A.; Buchanan, R. C., Enhanced percolative properties from partial solubility dispersion of filler phase in conducting polymer composites (CPCs). *Composites Science and Technology* **2010,** *70* (6), 892-900.

102. Derrida, B.; Stauffer, D.; Herrmann H.J.; J., V. e., Transfer matrix calculation of conductivity in three-dimensional random resistor networks at percolation threshold. *J Physique Lettres* **1983,** *44* (17), 701-706.
103. Stankovich, S.; Dikin, D. A.; Dommett, G. H. B.; Kohlhaas, K. M.; Zimney, E. J.; Stach, E. A.; Piner, R. D.; Nguyen, S. T.; Ruoff, R. S., Graphene-based composite materials. *Nature* **2006,** *442* (7100), 282-286.
104. Toker, D.; Azulay, D.; Shimoni, N.; Balberg, I.; Millo, O., Tunneling and percolation in metal-insulator composite materials. *Physical Review B* **2003,** *68* (4), 041403.
105. Pang, H.; Chen, T.; Zhang, G.; Zeng, B.; Li, Z.-M., An electrically conducting polymer/graphene composite with a very low percolation threshold. *Materials Letters* **2010,** *64* (20), 2226-2229.
106. Kim, H.; Macosko, C. W., Processing-property relationships of polycarbonate/graphene composites. *Polymer* **2009,** *50* (15), 3797-3809.
107. Sandler, J. K. W.; Pegel, S.; Cadek, M.; Gojny, F.; van Es, M.; Lohmar, J.; Blau, W. J.; Schulte, K.; Windle, A. H.; Shaffer, M. S. P., A comparative study of melt spun polyamide-12 fibres reinforced with carbon nanotubes and nanofibres. *Polymer* **2004,** *45* (6), 2001-2015.
108. Eda, G.; Chhowalla, M., Graphene-based Composite Thin Films for Electronics. *Nano Letters* **2009,** *9* (2), 814-818.
109. Yi, Y. B.; Tawerghi, E., Geometric percolation thresholds of interpenetrating plates in three-dimensional space. *Physical review. E, Statistical, nonlinear, and soft matter physics* **2009,** *79* (4 Pt 1), 041134.
110. Du, J.; Cheng, H.-M., The Fabrication, Properties, and Uses of Graphene/Polymer Composites. *Macromolecular Chemistry and Physics* **2012,** *213* (10-11), 1060-1077.
111. Chatterjee, S.; Nüesch, F. A.; Chu, B. T. T., Comparing carbon nanotubes and graphene nanoplatelets as reinforcements in polyamide 12 composites. *Nanotechnology* **2011,** *22* (27), 275714.
112. Steurer, P.; Wissert, R.; Thomann, R.; Mülhaupt, R., Functionalized Graphenes and Thermoplastic Nano-composites Based upon Expanded Graphite Oxide. *Macromolecular Rapid Communications* **2009,** *30* (4-5), 316-327.
113. Pham, V. H.; Cuong, T. V.; Dang, T. T.; Hur, S. H.; Kong, B.-S.; Kim, E. J.; Shin, E. W.; Chung, J. S., Superior conductive polystyrene - chemically converted graphene nano-composite. *Journal of Materials Chemistry* **2011,** *21* (30), 11312-11316.
114. Wu, H.; Zhao, W.; Hu, H.; Chen, G., One-step in situball milling synthesis of polymer-functionalized graphene nano-composites. *Journal of Materials Chemistry* **2011,** *21* (24), 8626-8632.
115. Qi, X.-Y.; Yan, D.; Jiang, Z.; Cao, Y.-K.; Yu, Z.-Z.; Yavari, F.; Koratkar, N., Enhanced Electrical Conductivity in Polystyrene Nano-composites at Ultra-Low Graphene Content. *ACS Applied Materials & Interfaces* **2011,** *3* (8), 3130-3133.
116. Huang, Y.; Qin, Y.; Zhou, Y.; Niu, H.; Yu, Z.-Z.; Dong, J.-Y., Polypropylene/Graphene Oxide Nano-composites Prepared by In Situ Ziegler−Natta Polymerization. *Chemistry of Materials* **2010,** *22* (13), 4096-4102.

117. Raghu, A. V.; Lee, Y. R.; Jeong, H. M.; Shin, C. M., Preparation and Physical Properties of Waterborne Polyurethane/Functionalized Graphene Sheet Nano-composites. *Macromolecular Chemistry and Physics* **2008,** *209* (24), 2487-2493.
118. Ansari, S.; Giannelis, E. P., Functionalized graphene sheet—Poly(vinylidene fluoride) conductive nano-composites. *Journal of Polymer Science Part B: Polymer Physics* **2009,** *47* (9), 888-897.
119. Du, J.; Zhao, L.; Zeng, Y.; Zhang, L.; Li, F.; Liu, P.; Liu, C., Comparison of electrical properties between multi-walled carbon nanotube and graphene nanosheet/high density polyethylene composites with a segregated network structure. *Carbon* **2011,** *49* (4), 1094-1100.
120. Potts, J. R.; Murali, S.; Zhu, Y.; Zhao, X.; Ruoff, R. S., Microwave-Exfoliated Graphite Oxide/Polycarbonate Composites. *Macromolecules* **2011,** *44* (16), 6488-6495.
121. Zhang, H.-B.; Zheng, W.-G.; Yan, Q.; Yang, Y.; Wang, J.-W.; Lu, Z.-H.; Ji, G.-Y.; Yu, Z.-Z., Electrically conductive polyethylene terephthalate/graphene nano-composites prepared by melt compounding. *Polymer* **2010,** *51* (5), 1191-1196.
122. Liang, J.; Wang, Y.; Huang, Y.; Ma, Y.; Liu, Z.; Cai, J.; Zhang, C.; Gao, H.; Chen, Y., Electromagnetic interference shielding of graphene/epoxy composites. *Carbon* **2009,** *47* (3), 922-925.
123. Zhang, H.-B.; Yan, Q.; Zheng, W.-G.; He, Z.; Yu, Z.-Z., Tough Graphene−Polymer Microcellular Foams for Electromagnetic Interference Shielding. *ACS Applied Materials & Interfaces* **2011,** *3* (3), 918-924.
124. Kim, I.-H.; Jeong, Y. G., Polylactide/exfoliated graphite nano-composites with enhanced thermal stability, mechanical modulus, and electrical conductivity. *Journal of Polymer Science Part B: Polymer Physics* **2010,** *48* (8), 850-858.
125. Vadukumpully, S.; Paul, J.; Mahanta, N.; Valiyaveettil, S., Flexible conductive graphene/poly(vinyl chloride) composite thin films with high mechanical strength and thermal stability. *Carbon* **2011,** *49* (1), 198-205.
126. De Bellis, G.; Tamburrano, A.; Dinescu, A.; Santarelli, M. L.; Sarto, M. S., Electromagnetic properties of composites containing graphite nanoplatelets at radio frequency. *Carbon* **2011,** *49* (13), 4291-4300.
127. Sandler, J. K. W.; Kirk, J. E.; Kinloch, I. A.; Shaffer, M. S. P.; Windle, A. H., Ultra-low electrical percolation threshold in carbon-nanotube-epoxy composites. *Polymer* **2003,** *44* (19), 5893-5899.
128. Yu, A.; Ramesh, P.; Itkis, M. E.; Bekyarova, E.; Haddon, R. C., Graphite Nanoplatelet−Epoxy Composite Thermal Interface Materials. *The Journal of Physical Chemistry C* **2007,** *111* (21), 7565-7569.
129. Yu, A.; Ramesh, P.; Sun, X.; Bekyarova, E.; Itkis, M. E.; Haddon, R. C., Enhanced Thermal Conductivity in a Hybrid Graphite Nanoplatelet – Carbon Nanotube Filler for Epoxy Composites. *Advanced Materials* **2008,** *20* (24), 4740-4744.
130. Zhang, G.; Xia, Y.; Wang, H.; Tao, Y.; Tao, G.; Tu, S.; Wu, H., A Percolation Model of Thermal Conductivity for Filled Polymer Composites. *Journal of Composite Materials* **2010,** *44* (8), 963-970.

131. Ganguli, S.; Roy, A. K.; Anderson, D. P., Improved thermal conductivity for chemically functionalized exfoliated graphite/epoxy composites. *Carbon* **2008,** *46* (5), 806-817.
132. Chandrasekaran, S.; Seidel, C.; Schulte, K., Preparation and characterization of graphite nano-platelet (GNP)/epoxy nano-composite: Mechanical, electrical and thermal properties. *European Polymer Journal* **2013,** *49* (12), 3878-3888.
133. Shtein, M.; Nadiv, R.; Buzaglo, M.; Kahil, K.; Regev, O., Thermally Conductive Graphene-Polymer Composites: Size, Percolation, and Synergy Effects. *Chemistry of Materials* **2015,** *27* (6), 2100-2106.
134. Lin, Y. C.; Hsu, F. H.; Wu, T. M., Enhanced conductivity and thermal stability of conductive polyaniline/graphene composite synthesized by in situ chemical oxidation polymerization with sodium dodecyl sulfate. *Synthetic Metals* **2013**, Volume 184, 29–34.
135. Vadukumpully, S.; Paul, J.; Mahanta, N.; Valiyaveettil, S., Flexible conductive graphene/poly(vinyl chloride) composite thin films with high mechanical strength and thermal stability. *Carbon* **2011**, Volume 49 (1), 198–205.
136. Shtein, M.; Nadiv, R.; Buzaglo, M.; Kahil, K.; Regev, O., Thermally Conductive Graphene-Polymer Composites: Size, Percolation, and Synergy Effects. *Chemistry of Materials* **2015**, 27 (6), 2100–2106.
137. Zhou, J.; Lucas, J. P., Hygrothermal effects of epoxy resin. Part II: variations of glass transition temperature. *Polymer* **1999,** *40* (20), 5513-5522.
138. Maggana, C.; Pissis, P., Water sorption and diffusion studies in an epoxy resin system. *Journal of Polymer Science Part B: Polymer Physics* **1999,** *37* (11), 1165-1182.
139. Peyser, P.; Bascom, W., The anomalous lowering of the glass transition of an epoxy resin by plasticization with water. *Journal of Materials Science* **1981,** *16* (1), 75-83.
140. Kotrotsos, A.; Vavouliotis, A.; Tsantzalis, S.; Kostopoulos, V., Effect of CNT modified matrix of epoxy CFRPs on hydrothermal behaviour of material. Evaluation of water uptake using electrical resistance measurements. *Plastics, Rubber and Composites* **2014,** *43* (4), 122-129.
141. Boinard, P.; Banks, W. M.; Pethrick, R. A., Changes in the dielectric relaxations of water in epoxy resin as a function of the extent of water ingress in carbon fibre composites. *Polymer* **2005,** *46* (7), 2218-2229.
142. Prolongo, S. G.; Gude, M. R.; Ureña, A., Water uptake of epoxy composites reinforced with carbon nanofillers. *Composites Part A: Applied Science and Manufacturing* **2012,** *43* (12), 2169-2175.
143. Guadagno, L.; Vertuccio, L.; Sorrentino, A.; Raimondo, M.; Naddeo, C.; Vittoria, V.; Iannuzzo, G.; Calvi, E.; Russo, S., Mechanical and barrier properties of epoxy resin filled with multi-walled carbon nanotubes. *Carbon* **2009,** *47* (10), 2419-2430.
144. Chaharmahali, M.; Hamzeh, Y.; Ebrahimi, G.; Ashori, A.; Ghasemi, I., Effects of nano-graphene on the physico-mechanical properties of bagasse/polypropylene composites. *Polymer Bulletin* **2014,** *71* (2), 337-349.

CHAPTER 3 EXPERIMENTAL

3.1 Materials

Graphene nanoplatelets (GNP), Grade M, from XG Sciences were used as the fillers in this project. These Grade M nanoparticles have an average thickness of approximately 6-8 nm (18-24 layers of graphene) and possess a typical surface area of 120 to 150 m^2/g. Three grades with different particle diameters are available with M5, M15 and M25 having 5, 15 or 25 microns diameter respectively. These particles are effective at providing barrier properties, while their pure graphitic composition makes them excellent electrical and thermal conductors. Unlike many other additives, GNP can improve mechanical properties such as stiffness, and surface hardness of the matrix material [1-5].

GNP can be easily mixed with almost all polymers, and can be an active ingredient in inks or coatings as well as an excellent additive to plastics of most types [6]. The manufacturing processes are non-oxidizing, so the as-received material has a pristine graphitic surface of sp^2 carbon molecules that makes it especially suitable for applications requiring high electrical or thermal conductivity (as shown in Table 3.1).

Table 3.1 Data sheet of GNP.

	Parallel to surface	Perpendicular to surface
Density (g/cm^3)	2.2	
Carbon content (%)	>99.5	
Thermal conductivity (W/mK)	3,000	6
Thermal expansion ($m/m/^oK$)	$4\text{-}6 \times 10^{-6}$	$0.5\text{-}1.0 \times 10^{-6}$
Tensile Modulus (GPa)	1,000	N/A
Tensile Strength (GPa)	5	N/A
Electrical Conductivity (S/m)	10^7	10^2

Only the M5 and M25 grades were used as fillers in this project due to time restraints.

The epoxy used in this project was Araldite LY 556®, a formulated resin for structural composites from Huntsman Advanced Materials. It is a pre-polymer based on the diglycidyl ether of bisphenol A (DGEBA) (Figure 3.1a) [7]. The hardener used in this study was XB 3473 (Huntsman Advanced Materials), which contains diethyltoluenediamine (80 % ~ 92 % concentration) and 1,2-diaminocyclohexane (4 % ~ 10 % concentration) (Figure 3.1b). During the curing process, the epoxide groups of the DGEBA react with the amine groups from the XB 3473 and crosslink to form a three-dimensional, thermosetting network.

a)

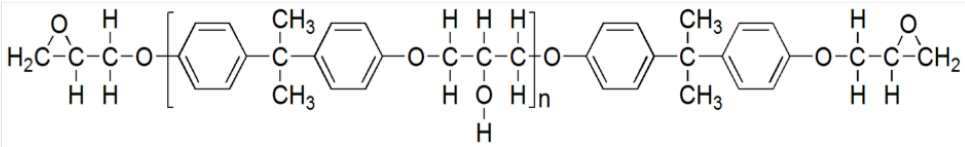

DGEBA

b)

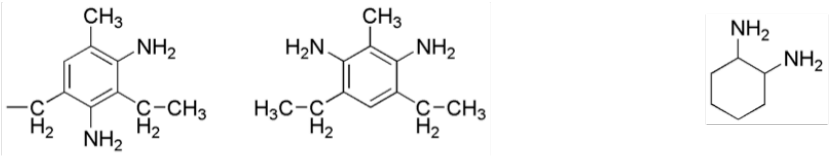

Diethyltoluenediamine 1,2 - Diaminecyclohexane

Figure 3.1 Chemical structure of DGEBA (a) and the components in the hardener (b) [7].

3.2 Preparation Methods

Three different routes for preparation the polymer/graphene nanoplatelets composites were compared:

1. Shear Mixing: Shear mixing is used to disperse, or transport, a minor phase or ingredient (liquid, solid, gas) into a major continuous phase (liquid), with which it would normally be immiscible. A high shear mixer with blade is used to blend epoxy and GNP in a beaker. The main advantage of shear mixing is its simplicity and time saving. The disadvantage lays in the relatively poor dispersion of the filler in the matrix.

2. Three-roll mill mixing: A three-roll mill uses shear forces created by three horizontally positioned rolls rotating at different speeds relative to each other, in order to mix, refine, disperse, or homogenize viscous materials fed into it [8]. The epoxy and graphene nanoplatelets mixture was poured directly into a three-roll-mill for uniform mixing.
3. Solution Compounding: Usually, a solvent which has a good interaction with both filler and polymer matrix is used to assist the dispersion of a filler in composites. During the mixing process, mixture will be heated to remove solvent. The advantage of solution compounding is that it can produce uniform filler dispersion and good interfacial interaction between the filler and matrix. The disadvantages are that the solvent used makes it not environment friendly and energy-consuming during solvent evaporation.

3.3 Preparation of Composites

Figure 3.2 Digital images of the mould with 5 mm thick polytetrafluoroethylene plate between the two 5mm steel plates.

Figure 3.2 is the mould used for preparing bulk composite samples. It consists of three layers, and using PTFE layer benefits the removal of the samples from metal mould due to the weak contact force between the composites and PTFE.

The three processing methods used for composites fabrication were as follows:

Shear mixing: the weight of graphene nanoplatelets, epoxy and hardener needed for preparation different filler loading epoxy/GNP composites were calculated and weighed. The GNP was then poured into a beaker (50 ml) of epoxy, stirred using a shear mixer (IKA eurostar 40 Stirrer) with an anchor stirrer (3 cm in diameter) for 1 hr at a rotation rate of 2000 rpm. The hardener (weight ratio of hardener and epoxy is 23:100) was added to the epoxy and the mixture stirred for a further 5 mins at the rate of 2000 rpm. The mixture was held in an oven at 80°C under a vacuum for 10 mins in order to degas it, and then transferred to a mould and left to rest at atmospheric pressure for 30 mins so that any remaining gas was released. Finally, the system was cured by placing the mould in an oven, and raising the temperature to 140 °C at heat rate of 3 °C/min and then held for 10 hrs. The oven was then cooled down to room temperature naturally and the sample taken out.

Three-roll mill: The same shear mixer used in shear mixing was used to pre-mix the epoxy and GNP for 5 mins at 2000 rpm at room temperature. The mixture was then poured into a three-roll mill (Torrey Hills T65 (2.5 × 5) Lab model) and mixed at a rate of 40 rpm, 80 rpm and 160 rpm respectively for the slow roll, middle roll and fast roll. The two gaps between three-rolls were kept the same. The mixture was then collected and the hardener added by shear mixing for 5 mins at 2000 rpm. The same degasing and curing process was then used for process 1 above.

Solvent-assisted mixing: The weighted epoxy, graphene nanoplatelets and chloroform (30 ml) were put in a 50 ml beaker, and stirred using a magnetic stirrer at the rate of 1000 rpm. During the stirring, the mixture was heated to 100 °C to remove the solvent. The mixture was weighed every two hours until the weight didn't change for three consecutive measurements. The hardener was then added over a five minute period whilst the mixture was stirred. The same degasing and curing process was then used for process 1 above.

It was found that the resin viscosity increased with increasing filler amount until at some point, it became difficult to fabricate a composite part. Thus, a maximum of 8 wt.% GNP was used.

3.4 Characterization of Filler and Epoxy Nano-composites

3.4.1 Optical Microscopy

Optical microscopy is one of the most basic tools to magnify images of small samples. It is simple, but still quite useful for characterizing the dispersion of fillers in a matrix. In this project samples were viewed under an Olympus BH-2 optical microscope using and ×10, ×20 and ×50 objective lens. The software AxioVision Rel. 4.8 was used to capture and adjust (exposure, contrast, saturation etc.) the images.

The two sides of the samples for optical microscopy need to be paralleled to each other to ensure good focusing. Therefore, during preparation, the surface was ground using abrasive paper of different coarseness (400, 800, 1200 then 2500). Finally, a polishing process was applied to give a high-quality surface finish.

3.4.2 Atomic Force Microscopy and Sample Preparation

Atomic force microscopy (AFM) or scanning force microscopy (SFM) is a very high-resolution type of scanning probe microscopy (SPM), with demonstrated resolution on the order of fractions of a nanometer, more than 1000 times better than the optical diffraction limit. It is a powerful and easy tool to identify the thickness of the fillers used in experiments. AFM images were obtained using a Dimension 3100 AFM (Bruker) in the tapping mode in conjunction with the 'TESPA' probe (Bruker).

Sample preparation for AFM was as follows: GNP were put into ethanol, and then sonicated at 70% power (maximum power of 820 W) for 0.5 hrs to fully disperse the graphene nanoplatelets. After that, more ethanol was added to dilute the mixture until it was almost transparent. Then a capillary glass tube was used to transfer the graphene nanoplatelets suspension onto a 1 cm × 1 cm silicon substrate which was placed in a clean vacuum oven to dry.

3.4.3 Raman Spectroscopy

Raman spectroscopy is a spectroscopic technique used to observe vibrational, rotational, and other low-frequency modes in a system. Raman spectroscopy is commonly used in chemistry to provide a fingerprint by which molecules can be identified. In this project, Raman plays a vital role as a non-destructive technique to detect the presence of GNPs in composites, and to investigate the crystallinity of the

GNPs. Furthermore, Raman can provide information about the orientation of fillers in the matrix and the stress transfer efficiency from the matrix to the fillers. Raman spectroscopy can be performed at room temperature and ambient pressure, and the resultant spectra can be acquired within minutes. The technique is based on the characteristic of inelastic scattering that occurs when a monochromatic light (usually a laser source) interacts with a sample [9]. The incident light excites an electron into a higher virtual state and then the electron decays back to a lower level, emitting a scattered photon. When the energy of the scattered photon is lower than that of the incident photon, it is defined as Stokes scattering, whilst anti-Stokes scattering occurs when the energy of the scattered photon is higher than that of the incident photon, which is much less usual than Stokes scattering. If the incident and the scattered photons have the same energy, then the scattering is known as elastic Rayleigh scattering. Rayleigh scattering is filtered out during analysis to prevent saturation of the CCD. Figure 3.3 shows an energy diagram of Stokes Raman scattering and anti-Stokes Raman scattering.

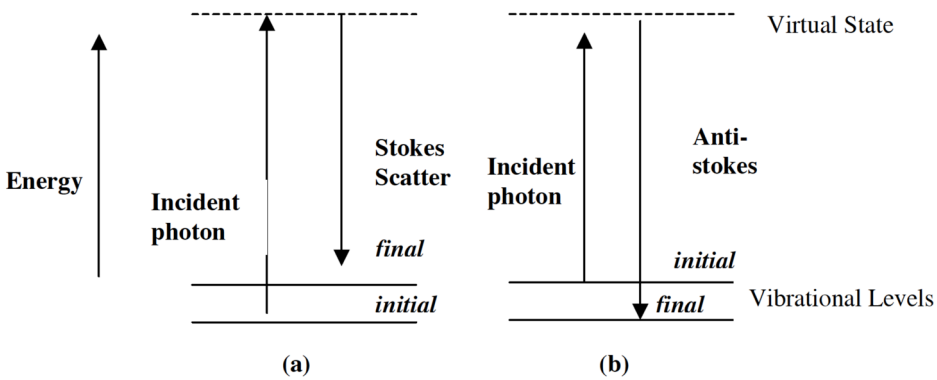

Figure 3.3 Diagram showing the energy level for Raman scattering, adapted from ref [10].

The Raman shift (cm^{-1}) for a band is defined as the difference in the incident wavenumber and scattered wavenumber (equation 3.1) and its proportion to the energy of the vibrational states in the sample. In graphene, the Stokes phonon energy shift caused by laser excitation creates two main peaks in the Raman spectrum: G (1580 cm^{-1}), a primary in-plane vibrational mode, and 2D (2690 cm^{-1}), a second-order overtone of a difference in plane vibration, D (1350 cm^{-1}) [11]. D and 2D peak positions are dispersive (dependent on the laser excitation energy). NB these are the positions quoted from a 532 nm excitation laser, as the 2D mode is dispersive. The D

mode is related to structural defects and impurity, while the G band is related to the sample's crystallinity.

$$Raman\ shift\ (cm^{-1}) = \frac{1}{\lambda_{incident}} - \frac{1}{\lambda_{scattered}} \quad (3.1)$$

In this study, Raman was performed using a Renishaw Raman Spectrometer with a HeNe excitation laser (632.8 nm wavelength). Prior to performing Raman experiments, the spectrometer was calibrated using the 520 cm^{-1} band of silicon and instrument setting of 100% of the laser power with high gain on the CCD and an exposure time of 10 s with 1 accumulation). The peak was fitted using WIRE™ software. If the peak value was outside the 519 ~ 521 cm^{-1} range, the calibration offset would be set.

For a powder sample, a small amount of GNP were placed on a glass slide and then compressed by another glass slide to make a smooth surface in case the rough surface contaminates the lens. For composite samples, the samples were cut from the bulk composite and ground with 800-grade emery paper. A HeNe laser (632.8 nm wavelength) was used with 10 % laser power to minimize the heating in the samples. The typical collection setting for the instrument were high gain on the CCD, and 5 acculations with a exposure time of 10 s). At least 5 regions were investigated from each sample examined to understand the variation within it.

3.4.4 Thermal Gravimetric Analysis (TGA)

TGA is commonly used to study materials that exhibit either mass loss or gain due to decomposition, oxidation, or loss of volatiles (such as moisture). It is an especially useful technique for the study of polymeric materials.

In this study, a TA Instrument TGA Q500 was used to obtain information on the thermal stability of the materials used and the composites. The powder sample (around 15 mg) was heated from 20 °C to 800 °C at the heating rate of 10 °C/min under a nitrogen atmosphere. In a desired temperature range, if a species is thermally stable, there will be no observed mass change. Negligible mass loss corresponds to little or no slope in the TGA trace. TGA also gives the upper limit for the temperature at which a material may be used, in that beyond this temperature the material will begin to degrade.

3.4.5 Scanning Electron Microscopy

A scanning electron microscopy (SEM) is a type of electron microscope that produces images by scanning a focused beam of electrons across a sample. The electrons interact with the atoms in the sample, to produce various signals that can be detected and which contain information about the sample's surface topography and composition. Due to its wide range of magnification, from about 10 times (about equivalent to that of a powerful hand-lens) to > 500,000 times, (about 250 times the magnification limit of the best light microscopes) SEM has become one of the most popular techniques to study surfaces. In this project, SEM was very important for analysis of the fillers dispersion and interfaces between the fillers and the matrix.

SEM samples must be of an appropriate size to fit in the specimen chamber and are generally mounted rigidly on a specimen holder stub. For conventional imaging in the SEM, specimens must be electrically conductive, at least at the surface, and electrically grounded to prevent the accumulation of electrostatic charge at the surface.

Sample preparation was as follows: For the filler powder samples, a few mg of GNP was sonicated in acetone to disperse it uniformly until it is almost transparent. After that, several drops of the liquid were transferred to a 1 cm × 1 cm gold-coated silicon substrate and dried in a vacuum oven. The composites were frozen in liquid nitrogen and then broken by a gripper. Some of the samples with low graphene nanoplatelets loadings are almost insulating. Therefore, gold coating (using an Edward S150B Sputter Coater) was applied to all samples and silver paint (Agar scientific Ltd. Unite, Batch No.0439) was used to connect the surface to the sample Stub. The topography of the samples was viewed using a Philips XL 30 field emission gun SEM (FEGSEM) at a 10kV acceleration voltage.

3.4.6 X-ray Diffraction

X-ray Diffraction (XRD) is a powerful tool for studying the atomic and molecular structure of a crystalline material. By measuring the angles and intensities of the incident X-ray beams diffracted by atoms in a crystal, a crystallographer can produce a three-dimensional picture of the density of electrons within the crystal. From this electron density, the mean positions of the atoms in the crystal can be

determined, as well as their chemical bonds, their disorder and various other information.

The theory is based on the Bragg model of diffraction (Figure 3.4). The beam coming from upper left causes each scatterer to re-radiate a small portion of its intensity as a spherical wave. If scatterers are arranged symmetrically with a separation d, these spherical waves will be in sync (add constructively) only in directions where their path-length difference $2d\sin\theta$ equals an integer multiple (n) of the wavelength λ (as shown in equation 3.2). In that case, part of the incoming beam is deflected by an angle 2θ, producing a reflection spot in the diffraction pattern.

$$2dsin\theta = n\lambda \tag{3.2}$$

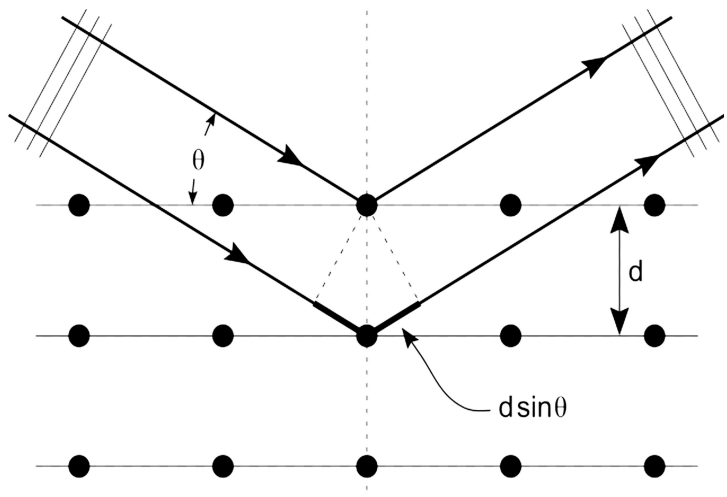

Figure 3.4 Bragg model of diffraction.

A reflection is said to be indexed when its Miller indices have been identified from the known wavelength and the scattering angle 2θ. Such indexing gives the length and angles of the unit-cell, as well as its space group.

In this project, XRD (X'Pert X-ray diffractometer) was carried out using a Cu Kα radiation source (λ = 1.542 Å) to identify the d spacing of fillers as received and fillers in the matrix prepared through three different methods.

3.4.7 Dynamic Mechanical Thermal Analysis

Dynamic mechanical thermal analysis (DTMA) is a technique used to study the viscoelastic behaviour of polymers. This approach can be used to locate the glass transition temperature (T_g) of the material, as well as to identify transitions corresponding to other molecular motions, data which is critical for the application of

polymer composites. T_g is one of the most important and representative parameters of the chemical and physical properties of polymer matrix composite materials [12] and gives information about the mechanical properties of a composite material, the chemical structure of its matrix and the materials performance under specific environmental conditions.

During DMTA, a sinusoidal stress is applied to a specimen and the strain in the specimen is measured, allowing one to determine the complex modulus (E*). For viscoelastic polymer composite materials, there is a phase lag, δ between the input stress and output strain, which is defined as follows [13]:

$$E^* = \frac{Stress}{Strain} \tag{3.3}$$

$$E' = E^* cos\delta \tag{3.4}$$

$$E'' = E^* sin\delta \tag{3.5}$$

$$tan\delta = \frac{E''}{E'} \tag{3.6}$$

During where *E'* is storage modulus, *E''* is loss modulus. DMTA temperature of the sample and/or the frequency of the stress are often varied, leading to variations in the complex modulus; the physical and thermodynamical properties of a sample are measured as a function of the temperature. The deformation is kept low to avoid changing the structure of the substance (the deformation is always kept within the linear viscoelastic range).

At the T_g, the *E'* decreases dramatically and the loss modulus reaches a maximum, and the ratio of loss modulus to storage modulus is defined as tan δ, which reaches its peak value. The temperature when tan δ reaches its peak is viewed as the T_g of a polymer. DMTA can also determine changes in storage modulus to study the load transfer from matrix to fillers.

All of the DMTA experiments in this work were performed using a TA Instruments Q800. Specimen dimensions for DMTA were ~ 35mm × 10mm × 1-3mm. The dimensions value inputted into the DMTA machine software were averaged values of at least three measurements at different points on a specimen. Single-cantilever bending mode at 1 Hz were applied for all specimen, over a temperature range of room temperature to 200 °C at a heating rate of 5 °C/min. The stress was varied such that the strain was kept constant at 1% throughout the

experiment. The curves of E′, E″, tan δ were displayed as a function of temperature via Universal Analysis software.

3.4.8 Tensile Testing

Tensile testing [14] is probably the most fundamental type of mechanical test. Tensile tests are simple and relatively inexpensive. During the test, a sample is subjected to a controlled increasing elongation until failure. The properties that are directly measured are load and change in length. In particular, the Young's modulus, and yield strength can be determined from these measurements.. The results can be applied for quality control of materials for different purposes, and can be used to predict a material's reaction under other types of forces.

Uniaxial tensile testing is the most commonly used technique for obtaining the mechanical characteristics of isotropic materials. The most common testing machine used in tensile testing is the universal testing machine. This type of machine has two clamps; one is fixed and the other is adjusted for the length of the specimen and driven to apply tension to the test specimen. Alignment of the test specimen in the testing machine is critical, especially for brittle materials. If the specimen is misaligned, either at an angle or offset to one side, it will dramatically skew the results.

For tensile testing of epoxy/graphene nanoplatelets composites, an extensometer was mounted onto the specimens to ensure the accurate measurement of strain. The samples were left in the mechanical testing room, in which the temperature was set at 23 ± 0.1 °C and a humidity set at 50 ± 5 %, for at least 24 h prior to mechanical testing. Tensile testing was carried out using an Instron-1122 universal testing machine. The machine was equipped with a 1 N load cell and the crosshead speed was set at 0.5 mm/min. At least 5 composite samples for each loading were tested. The strain measurements were measured with clip on extensometer. The results were averaged.

3.4.9 Water Uptake Measurement

Water uptake measurements determine the relative rate of absorption of water when a sample is immersed, and the weight percentage of water absorbed when saturated. The results of these tests can act as a guide to the proportion of water

absorbed by a material and consequently, in those cases where the relationships between moisture and electrical or mechanical properties, dimensions, or appearance have been determined, as a guide to the effects of exposure to water or humid conditions on such properties; and second, as a control test on the uniformity of a product.

In this project, the standard test method used to measure water uptake of this resin/GNP composite is ASTM-D570. An analytical balance capable of reading 0.0001 g and an oven capable of maintaining uniform temperatures of 50 ±3°C and of 105 to 110°C were used for these tests. The test specimens were disks with 50.8 mm in diameter and 3.2 mm in thickness. Permissible variations in thickness were ± 0.18 mm for hot-molded and ± 0.30 mm for cold-molded or cast materials. The surface was polished with 1200 abrasive paper. Three specimens for each loading were prepared. The oven containing distilled water was heated to 50°C, then all of the specimens were immersed directly in the water. All of the samples were removed from the water after 1, 2, 4, 8, 24 and 48 hrs, and wiped free of surface moisture with a dry cloth. Specimens were allowed to cool down for a short period of time (~ 3 mins) before weighting. The effect of removing the specimens from the chamber for a short period of time on the measurement of weight gains was shown to be negligible. All of the specimens were weighed to the nearest 0.001g, and then immediately replaced in the water. The weightings were repeated at the end of the first week and every two weeks thereafter until the increase in weight per two-week period, as shown by three consecutive weightings, averaged less than 1 % of the total increase in weight or 5 mg, whichever was greater; the specimen was considered to be substantially saturated. The difference between the substantially saturated weight and the dry weight was considered as the water absorbed when substantially saturated.

3.4.10 **Thermal Conductivity Measurement**

GNPs have excellent thermal conductivity, and are expected to improve the thermal conductivity of epoxy/GNP composites significantly. The degree of enhancement depends on the loading, dispersion, and orientation of fillers, and its interaction with the epoxy matrix. Thermal conductivity measurements are used to detect the property of a material to conduct heat. In this study, a Fox 50 from LaserComp was used, which is one of the most advanced instruments to measure

thermal conductivity in moderate range. The Fox 50 Heat Flow Meter is an accurate, easy-to-use instrument for measuring the thermal conductivity according to ASTM C518 and ISO 8301. Samples are placed between two plates in the test stack and a temperature gradient is established over the thickness of the material. The upper plate remains stationary while a pneumatic drive positions the lower stack to assure reliable contact between the sample and the transducer, which helps to minimize interfacial resistance. The general principle of the Fox heat flow meter instruments is based on one-dimension equation of the Fourier–Biot law:

$$q = -\lambda(\frac{dT}{dx}) \tag{3.7}$$

where q is heat flux (W/m^2) flowing through the sample, λ is its thermal conductivity (Wm^{-1}K^{-1}) of the sample, dT/dx is the temperature gradient (Km^{-1}) on the isotherm flat surface in the sample.

If a flat sample is placed between two flat isothermal plates with the plates maintained as different temperatures, eventually an uniform one dimensional temperature filed is established within the sample volume (size of the plates is supposed to be much larger than the thickness of the sample). The temperature field gradient within the sample is equal to the difference between temperatures of its surfaces ΔT ($\Delta T = T_{\text{hot surface}} - T_{\text{cold surface}}$) divided by its thickness Δx, because in this case the average temperature gradient $d\text{T}/dx$ is equal to $-\Delta T/\Delta x$. The thermal resistance of the flat sample R_{sample} is equal to its thickness Δx(m) divided by its thermal conductivity λ:

$$R_{sample} = \Delta x/\lambda \quad (\text{m}^2\text{K W}^{-1}) \tag{3.8}$$

Basic heat flow meter measurements conflate the sample's thermal resistance with the thermal contact resistance of the sample/transducer interface. This interfacial resistance can often be greater than the bulk thermal resistance of the sample, leading to a calculated thermal conductivity that is lower than its true value. The Fox 50 heat flow meter using WinTherm software is able to measure the sample resistance and interface resistance independently, using a two-thickness procedure of calibrations and tests.

3.4.11 **Oscillating Shear and Rotational Shear Rheometer**

Adding of fillers into an epoxy resin matrix can cause the viscosity to rise, which will affect its handling, processing, and applications. For example, more energy will be consumed and inhomogeneous mixing were likely to occur; leading to poor composite properties, especially for mechanical performance [15]. For carbon nanotube/epoxy composites, some reports showed that a elastic gel network had formed [16] and the viscosity was increased to a large extent, making their processing as composite matrices much more difficult [17]. So it is necessary to test the rheology of epoxy/GNP composite.

A Thermo Scientific Haake MARS (Modular Advanced Rheometer System) was used to perform all the rheological studies on epoxy suspensions. All measurements were performed at room temperature using 35 mm aluminum disposable parallel plates with a 0.8 mm gap. All of the rheological parameters were calculated and displayed via Haake Rheowin software.

Both the dynamic and steady shear experiments followed closely the methods described by Kinloch et al [18]. The flow properties of the suspensions were studied using the rheometer in rotational mode. The shear rate (γ) was increased in a stepwise manner from 0.005 to 1000 s^{-1} and the sample was held at each step for 60 s. Values of shear stress (τ) and shear viscosity (η) were recorded for each shear rate. Rheological characterisation was also performed under dynamic oscillatory mode to assess the structure formed by GNP reinforcements within the linear viscoelastic region (LVR). A dynamic strain sweep test (0.5 – 500 % strain) was first applied to the samples to determine the LVR region. Once this region was identified, a frequency sweep test over a range of 0.1 to 100 (rad/s) was performed at constant strain.

3.4.12 **Impedance Spectroscopy**

GNPs, as carbon fillers, possess extraordinary electrical properties with conductivity of 10^7 S/m parallel to surface or 10^2 S/m perpendicular to surface. The main purpose of this project is to improve the electrical conductivity of epoxy resin composites by adding GNP to form a conductive network.

Impedance spectroscopy measures electrical conductivity by applying an alternating current (ac) to a material, and detecting its response. Electrical impedance

(Z) is the complex ratio of voltage applied to current for an ac current. Impedance can be viewed as an extension of the concept of resistance to AC circuits. It possesses both magnitude and phase, while resistance has only magnitude. In a direct current (DC), there is no distinction between impedance and resistance; the latter can be thought of as impedance with zero phase angle (θ).

Impedance, as a complex quantity, consists of two parts, resistance (R) and capacitance (C). The former one forms the real component (Z') of impedance; the latter forms the imaginary part (Z''). Their relationship is as shown in Figure 3.5

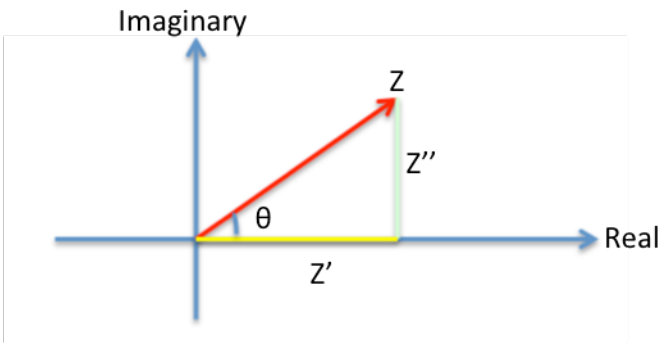

Figure 3.5 An impedance vector diagram.

$$Z = Z' + jZ'' \tag{3.9}$$

$$Z' = |Z|cos\theta \tag{3.10}$$

$$Z'' = |Z|sin\theta \tag{3.11}$$

$$\theta = tan^{-1}\frac{Z''}{Z'} \tag{3.12}$$

As we can see, if $\theta = 0^o$, the material is a pure resistor and if $\theta = 90^o$ it is a pure capacitor. In most cases, a composite material is a combination of both components where $0^o < \theta < 90^o$. In analysis of the impedance of a material, two types of plots are often used, the Nyquist plot and the Bode plot. A Nyquist plot is a parametric plot of a frequency response used in automatic control and signal processing. Generally, the real part of impedance (Z') is plotted on the x-axis while the imaginary part (Z'') is plotted on the y-axis. The shape of a Nyquist line can be used to estimate the equivalent circuit for the materials and get a rough idea about the electrical components (resistor or capacitor) and their arrangements (series or parallel). A Bode plot is a graph of the frequency responses of magnitude and phase in an electrical

system. Usually two plots are combined to form a Bode plot. The Bode magnitude plot expresses the magnitude of the frequency response, and a Bode phase plot, expresses the phase shift. Both quantities are plotted against a horizontal axis proportional to the logarithm of frequency. These plots can show you directly the trend of impedance in the circuit with frequency. In the case of the series arrangement, the corresponding Nyquist and Bode plots are as shown in Figure 3.6.

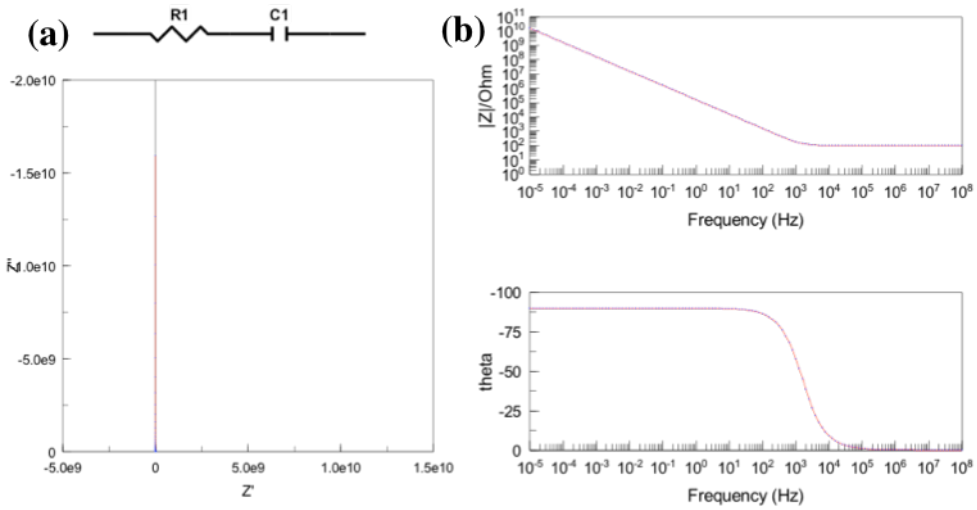

Figure 3.6 Nyquist (a) and Bode plots (b) for a resistor and a capacitor connected in series, simulated by Zview software.

Accordingly, the equations to represent the circuit shown in Figure 3.6 may be written as:

$$Z^*(\omega) = Z'(\omega) + jZ''(\omega) \tag{3.13}$$

$$Z'(\omega) = R_1 \tag{3.14}$$

$$Z''(\omega) = \frac{1}{\omega C_1} \tag{3.15}$$

In the case of a resistor and capacitor connected in parallel, then the corresponding Nyquist line is shown in Figure 3.7.

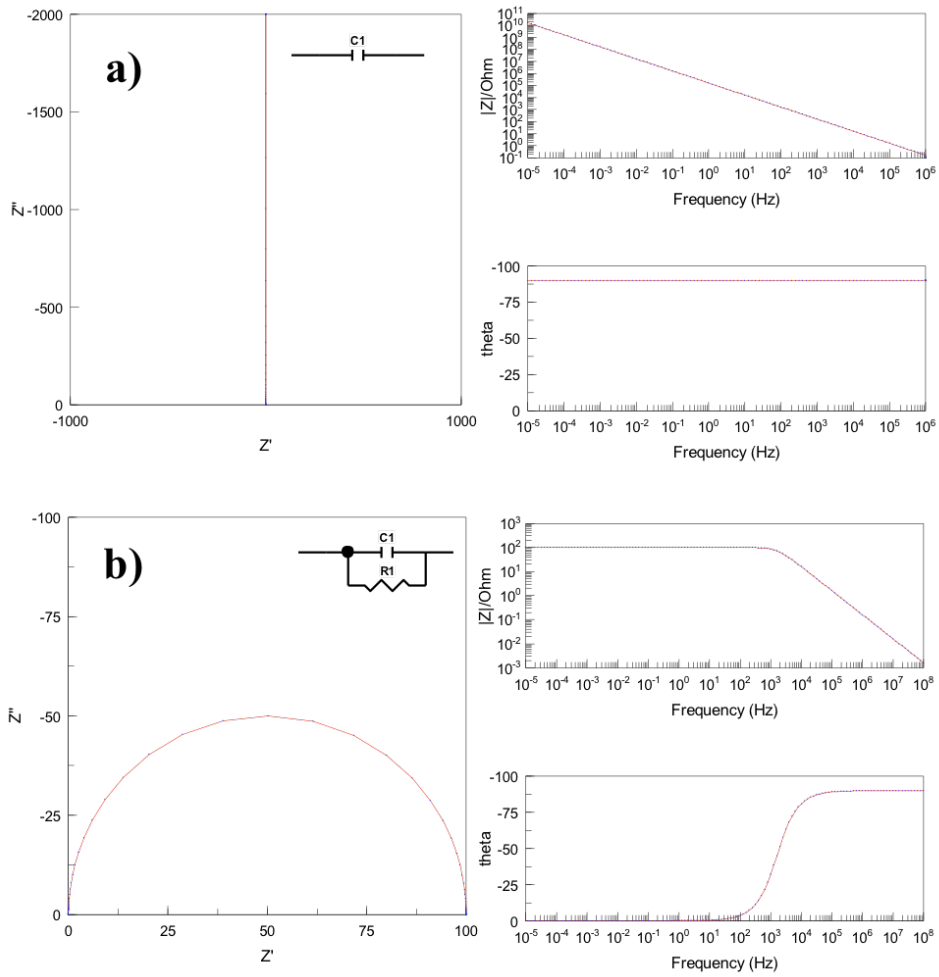

Figure 3.7 Nyquist and Bode plots for an ideal capacitor (C = 1μF) (a) and (b) the impedance of resistor and capacitor connected in parallel (R = 100Ω, C = 1μF), simulated using Zview software.

The circuit equations derived from such an arrangement are as follows:

$$\frac{1}{Z^*} = \frac{1}{Z_{R1}} + \frac{1}{Z_{C1}} = \frac{Z_{R1}+Z_{C1}}{Z_{R1}+Z_{C1}} \qquad \text{for parallel} \tag{3.16}$$

Therefore

$$Z^* = \frac{Z_{R1}\times Z_{C1}}{Z_{R1}+Z_{C1}} \tag{3.17}$$

Based on the plots from the impedance data, equivalent circuit models can be proposed, providing information about the structure of composites.

A NumetriQ PSM1735, connected to an Impedance Analysis Interface (IAI), was used to measure the impedance of composite samples. The IAI is an accessory that can provide a wide range of shunts (1 mΩ - 500 MΩ) that enabled the

measurement of samples of various resistances. The NumetriQ PSM1735 supplied the voltage and displayed the data obtained. The measurements were carried out with a four terminal Kelvin connection with a Kelvin clip, which can eliminate the effects of contact resistance on the results. The instrument was turned on for at least thirty minutes to warm up prior to a measurement. A resistor of known value was first tested to verify that the instrument was working correctly. Data acquisition was performed in Inductor-Capacitor-Resistor (LCR) mode. Each sample was measured five times. The parameters of frequency, impedance, inductance, capacitance, phase, tan δ, and Q factor and resistance were listed separately in different columns. A frequency range of 1 to 10^6 Hz with voltage (rms) amplitude of 1.0 V was used for all experiments. Rectangular composite specimens were cut from bulk samples and ground with fine abrasive paper. Silver paint was then applied to both ends and left it to dry for a few minutes, to minimize the contact resistance. Two conductive copper wires were connected to both ends by silver-loaded epoxy adhesive. The samples were kept in oven for 20 hours at 60 °C to dry the adhesive.

The specific conductivity of the composite is defined as in equation 3.18, where *l, w,* and *h* represent the length, width and thickness of the rectangular specimens for impedance test. To measure the sample specific conductivity, the dimensions needed to be taken into consideration. These dimensions were measured at three different points of each sample.

$$\sigma = \frac{1}{R} \times \frac{l}{w*h} \tag{3.18}$$

References

1. Zaman, I.; Phan, T. T.; Kuan, H.-C.; Meng, Q.; Bao La, L. T.; Luong, L.; Youssf, O.; Ma, J., Epoxy/graphene platelets nano-composites with two levels of interface strength. *Polymer* **2011,** *52* (7), 1603-1611.
2. Singh, S.; Srivastava, V. K.; Prakash, R., Influences of carbon nanofillers on mechanical performance of epoxy resin polymer. *Applied Nanoscience* **2015,** *5* (3), 305-313.
3. Zaman, I.; Manshoor, B.; Khalid, A.; Meng, Q. S.; Araby, S., Interface modification of clay and graphene platelets reinforced epoxy nano-

composites: a comparative study. *Journal of Materials Science* **2014,** *49* (17), 5856-5865.

4. Yasmin, A.; Daniel, I. M., Mechanical and thermal properties of graphite platelet/epoxy composites. *Polymer* **2004,** *45* (24), 8211-8219.
5. Wang, F. Z.; Drzal, L. T.; Qin, Y.; Huang, Z. X., Mechanical properties and thermal conductivity of graphene nanoplatelet/epoxy composites. *Journal of Materials Science* **2015,** *50* (3), 1082-1093.
6. Li, B.; Zhong, W.-H., Review on polymer/graphite nanoplatelet nano-composites. *Journal of Materials Science* **2011,** *46* (17), 5595-5614.
7. Pham, H. Q.; Marks, M. J.; Epoxy Resins. In: Mark HF, ed. Encyclopedia of Polymer Science and Technology. 3 ed: John Wiley & Sons **2004**.
8. Harnby, N.; Edwards, M. F.; Nienow, A. W., *Mixing in the process industries*. Butterworth-Heinemann: Oxford, **1997**.
9. Jorio, A.; Pimenta, M. A.; Filho, A. G. S.; Saito, R.; Dresselhaus, G.; Dresselhaus, M. S., Characterizing carbon nanotube samples with resonance Raman scattering. *New Journal of Physics* **2003,** *5*, 139.
10. Rusli, R. Interfacial micromechanics of natural cellulose whisker polymer nano-composites using Raman spectroscopy. PhD thesis, The University of Manchester, **2011**.
11. Childres, I.; Jauregui, L. A.; Park, W.; Cao, H.; Chen, Y. P.; Raman Spectroscopy of graphite and related materials, Purdue University, IN, USA, Nova Science Publishers **2013**.
12. Bussu, G.; Lazzeri, A., On the use of dynamic mechanical thermal analysis (DMTA) for measuring glass transition temperature of polymer matrix fibre reinforced composites. *Journal of Materials Science* **2006,** *41* (18), 6072-6076.
13. Menard, K. P., *Dynamic Mechanical Analysis. A Practical Introduction* . 2nd ed.; CRC Press: New York, **2008**.
14. Czichos, H.; Saito, T.; Smith, L.; Springer Handbook of Materials Measurement Methods, **2006**, ISBN: 978-3-540-20785-6.
15. Pham, H. Q.; Maurice, J. M.; Eproxy Resins: Encyclopedia Of Polymer Science and Technology. **2004**.
16. Huang, Y. Y.; Ahir, S. V.; Terentjev, E. M., Dispersion rheology of carbon nanotubes in a polymer matrix. *Physical Review B* **2006,** *73* (12), 125422.
17. Othman, R. N. R.; Synthesis and Characterisation of Hybrid Carbon Nanotube–Silica Microparticles. PhD Thesis, The University of Manchester, **2012**.
18. Kinloch, I. A.; Roberts, S. A.; Windle, A. H., A rheological study of concentrated aqueous nanotube dispersions. *Polymer* **2002,** *43* (26), 7483-7491.

CHAPTER 4 STRUCTURAL CHARACTERISATION OF M5 AND M25 EPOXY COMPOSITES

4.1 Introduction

This chapter focuses predominantly on the characterization of the dispersion and orientation of the fillers in the polymer composites prepared by shear mixing. Then a comparative study will be presented for samples fabricated by three-roll mill and solvent-assisted compounding.

4.2 Raman Characterisation of GNP

Three grades of graphene nanoplatelets from XG Sciences™, M5, M15 and M25, were used as fillers in this thesis. It is therefore important to characterise independently the as-received GNP using Raman, AFM, XRD and SEM. These data were then compared to the company's own datasheet.

The Raman spectroscopy data provided by the product manufacturer (Figure 4.1b) shows a very small D band, indicating a nearly defect-free structure.

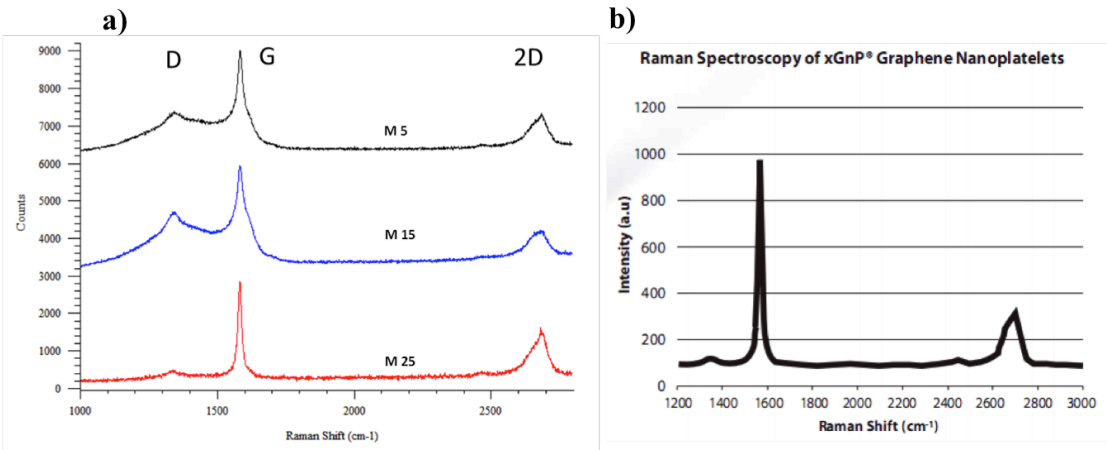

Figure 4.1 Raman spectroscopy of M5, M15 and M25 (a) obtained from experiment and (b) the data of grade M graphene nanoplatelets adapted from XG Sciences data sheet.

Raman spectra of the XG nanoplatelets (Figure 4.1) had the D, G and 2D bands expected for sp^2 materials with a high degree of crystallinty. M25 possessed the

highest G/D ratio out of the samples, possible due to its large size meaning that there was less chance that an edge of the platelet was under the laser spot. Whereas the M5 and M15 had more edges compared to the basal plane due to their smaller diameter. The 2D bands for the samples were comprised two peaks with the lower wavenumber being less intense, which is more characteristic of graphite than graphene, confirming that the platelets were > 10 layers thick. These Raman spectra were consistent with the datasheet.

4.3 AFM Characterisation of GNP

AFM was used to measure the thickness of graphene nanoplatelets fillers. The red dash lines in Figure 4.2b and d are drawn manually for the average of the height by eliminating effects of sharp noises. It is found that M5, and M25 have similar thickness of 4 ~ 7 nm, indicating a thickness of 10 ~ 20 layers of graphene (Figure 4.2). The diameters of the flakes were found to be consistent with the manufacturer's data sheet with M5 and M25 having around a diameter of approximately 10 μm, and 25 μm respectively.

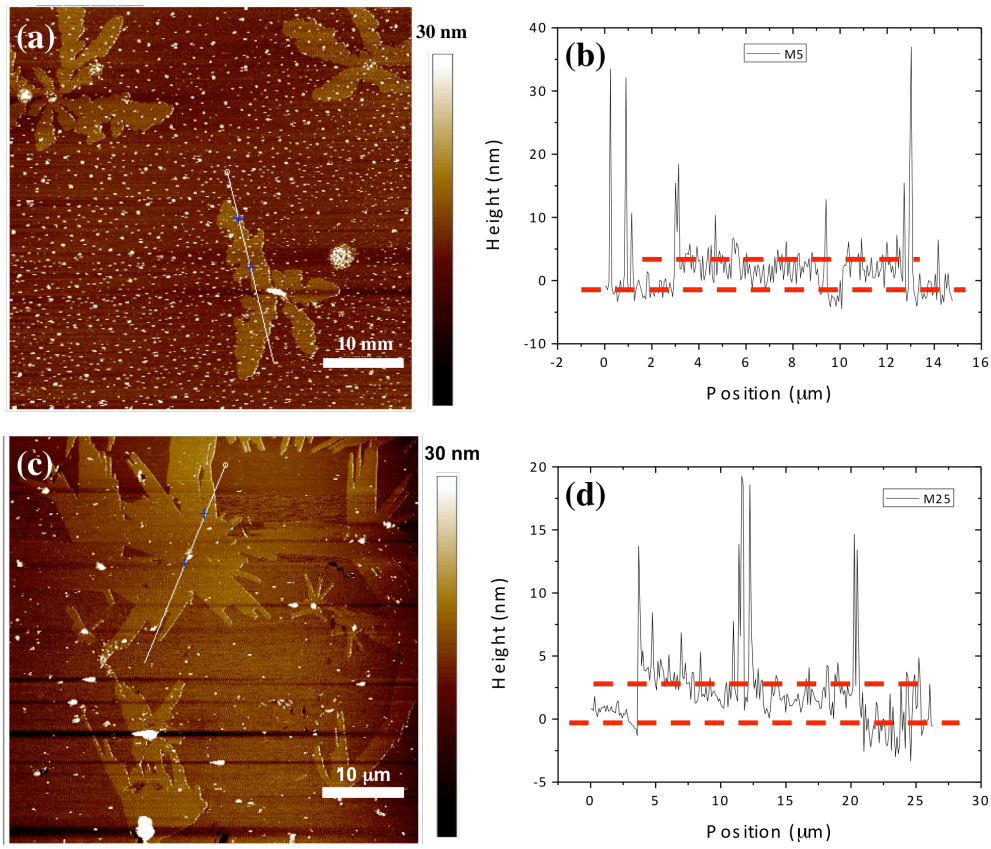

Figure 4.2 AFM images and height profiles of M5 (a) and M25 (b). The red dash lines in (b) and (d) are a guide to the eye.

4.4 Preliminary Characterisation of the GNP/epoxy Composites Produced by Shear Mixing

4.4.1 Rheology of Epoxy-GNP Dispersions

Figure 4.3 shows the modulus data for the epoxy containing the M5 and M25 measured during a strain sweep, in which the strain was increased stepwise and the moduli measured at each strain step. G′ and G″ represent the elastic and viscous response of the sample, respectively. In the case of neat epoxy, G′ decreased by over two orders of magnitude with increased strain up to the highest strain limit (γ = 1000 %), indicating a typical shear thinning response. Shear thinning properties can provide desirable attributes to a suspension, such as stability when at rest but ease of application or pouring when a stress is applied, which is good for dispersion and processing. The G″ however was constant throughout the whole range of γ tested. G″ dominated over G′ in the neat epoxy, suggesting liquid-like behaviour and no internal network formation in the epoxy. The 1 wt.% M5 and M25 samples had similar trends to the neat epoxy. However, the addition of 3 wt.% and 5 wt.% the GNPs into epoxy changed slightly the behaviour of G′ with the appearance of small plateaus at low strains. These plateaus mean that G′ was independent of γ, demonstrating some internal structure has been formed which remained stable under low shear. This plateau region is known as the linear viscoelastic region (LVR), in which the sample's response is independent of the strain applied. The elastic structure was fragile and broken upon the application of a small increase of strain. G″ was found to dominate over G′ until 8 wt.% of the M25 GNP had been added to epoxy, for which a crossover between G′ and G″ occurred. This crossover characterises the transition from elastic to viscous behaviour the strain at which is occurs is known as the crossover strain, γ_c [1-2].

Figure 4.3 shows the dependency of G′ and G″ with strain amplitude as measured by oscillatory shear measurements for dispersions of M5/epoxy and M25/epoxy.

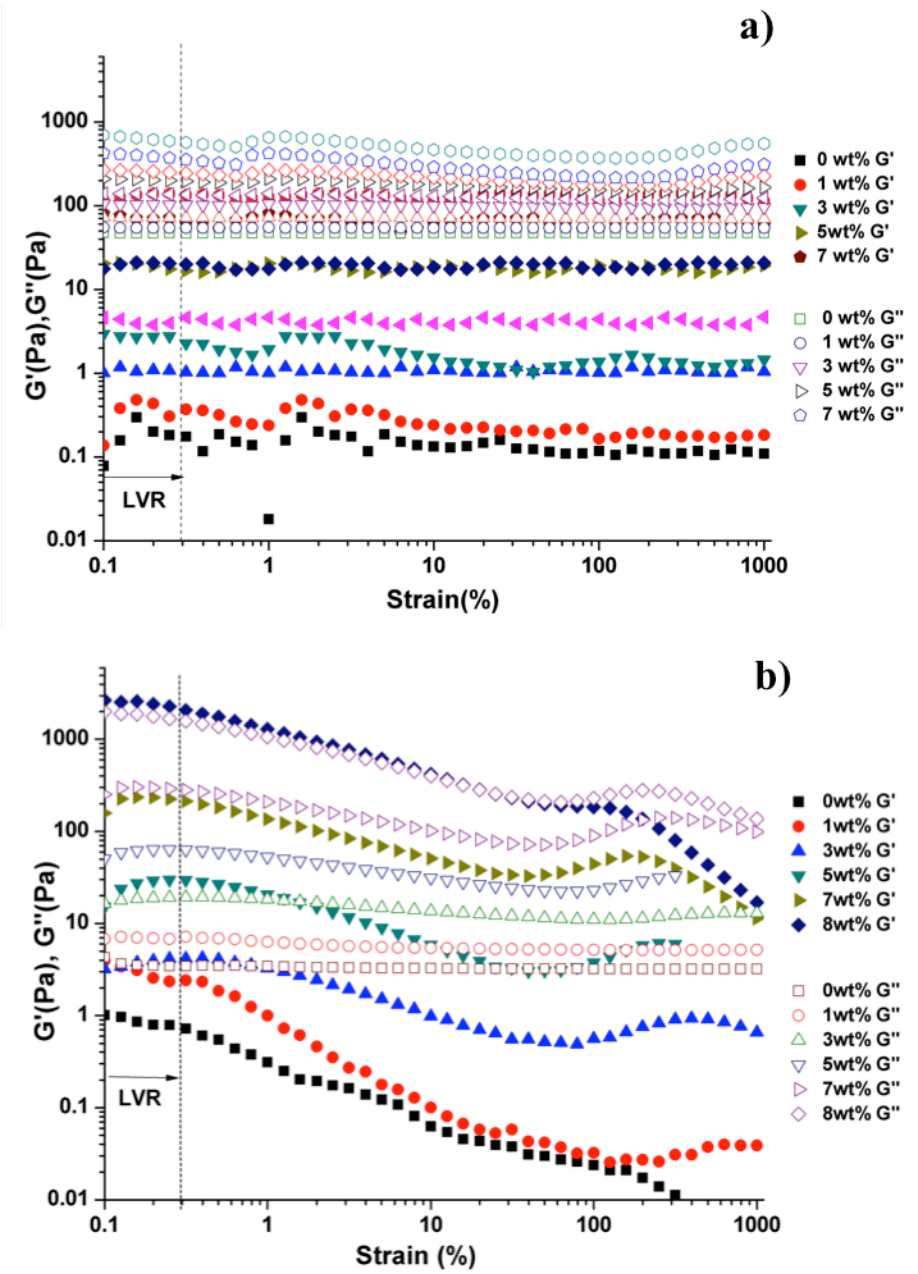

Figure 4.3 The dependency of G' and G'' with strain amplitude as measured by oscillatory shear measurements for dispersions of M5/epoxy (a) and M25/epoxy (b). The experiments were conducted at room temperature and a fixed frequency of 1 rad/s.

For all the loadings, there is no dramatic increase of G' or G'', which means no rheology percolation was observed. There is no big difference between the M5 and M25 epoxy suspensions, except that the viscosity of M25/epoxy mixture is higher than that of M5 due to M25's larger aspect ratio.

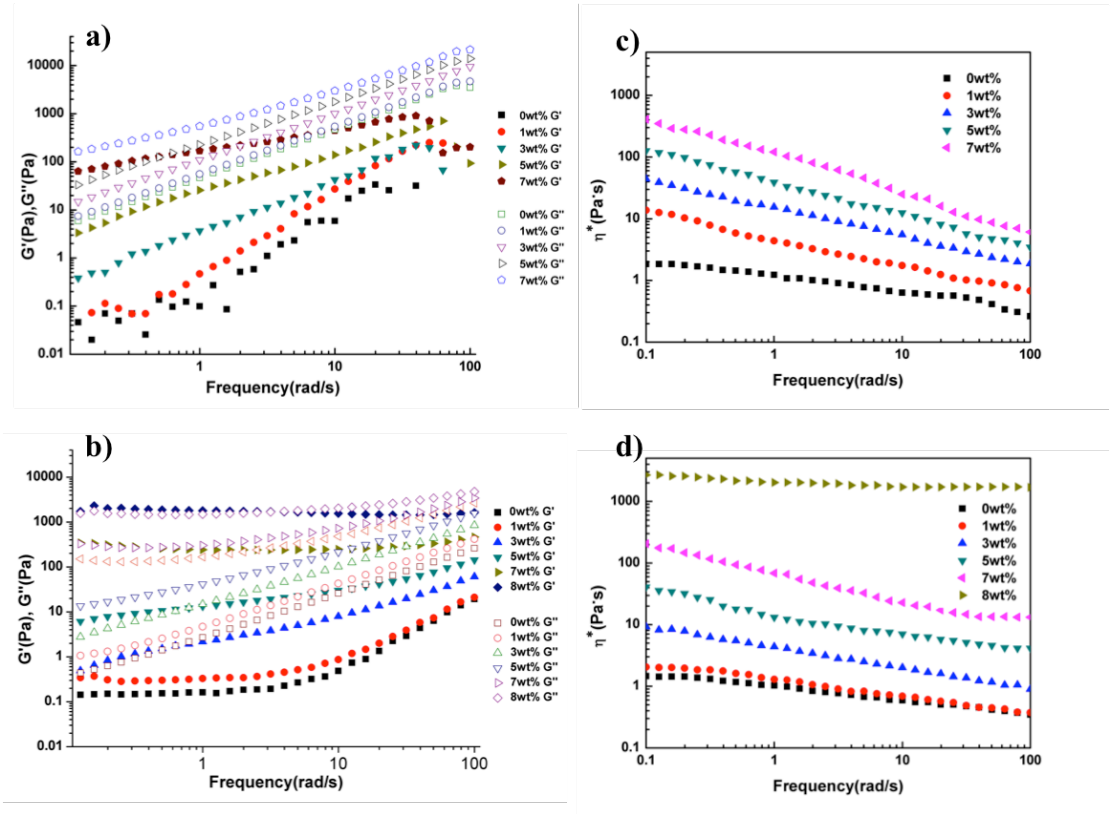

Figure 4.4 Frequency sweep measurements conducted within LVR (γ = 0.2%), showing G' and G'' vs. frequency for M5 (a) and M25 (b)/epoxy composites, and their complex viscosity (η) of M5 (c) and M25 (d)/epoxy composites.*

A frequency sweep was carried out on the samples within LVR (as shown in Figure 4.3a) to provide information regarding the structure of the dispersion [3-5]. Based upon Fig 4.3, it was decided that a strain of $\gamma_0 = 0.2$ % was appropriately within the LVR. The modulus behaviour and complex viscosity (η^*) of epoxy composites obtained under the frequency sweep are shown in Figure 4.4. The η^* and dynamic modulus of epoxy composites both increase significantly with incorporation of stuff M5 and M25. The rheological behaviour was similar for all the samples with a GNP loading of < 7 wt.% with G' and G'' values increasing with frequency and G' < G''. These spectra are typical for a viscous dispersion. However, for the 7 wt.% sample, G' is almost equal to G'' and independent of frequency whereas G'' only slightly increases and then only at very high frequency. The moduli for the 8 wt.% samples were independent of frequency. These data show that a stable, elastic internal network formed at loadings ≥ 7 wt.%, leading a solid-like elastic behaviour.

It can be concluded overall that the GNPs formed an elastic network within the epoxy upon increasing loadings. The complex viscosities of M5 and M25

composites, increased by two and three orders of magnitude respectively upon 8wt.% filler loadings. The η^* of 8 wt.% M25/epoxy composite is independent of frequency, showing an elastic behaviour.

4.4.2 XRD Characterization of GNP and Composites

The XRD patterns (as shown in Figure 4.5) of the M25 samples showed a strong peak at $2\theta = 26.54^{o}$ (corresponding to a d spacing = 0.336 nm) which is from the basal reflection of (0 0 2)) and identical with pristine graphite. Pure epoxy gave a strong peak around $2\theta = 18°$ and a weak and broad peak around $2\theta = 43°$, which show epoxy is amorphous. The XRD patterns of the composite were obviously a combination of the spectra of pure GNP and epoxy, indicating that shear mixing and curing process have no effect on the crystal structure of the M25 graphene nanoplatelets.

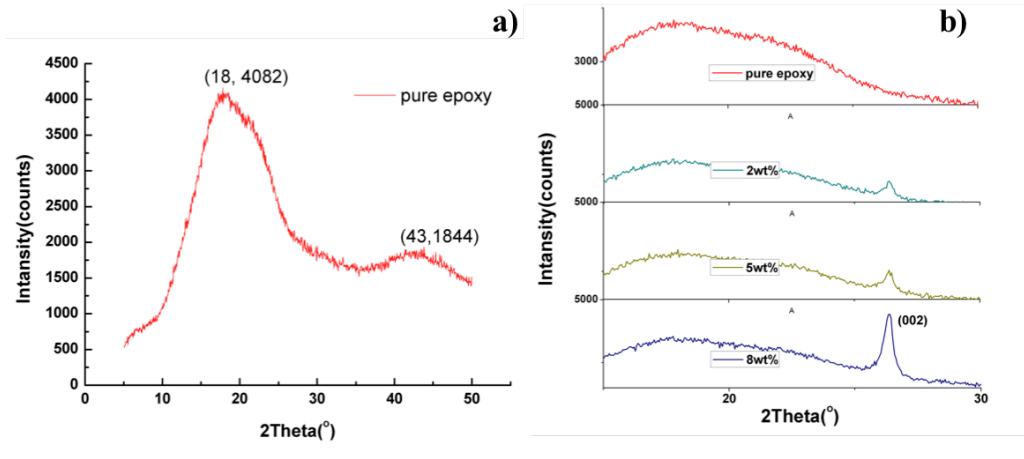

Figure 4.5 XRD patterns of GNP M25 (b), pure epoxy (a) and composite samples (b) with 2, 5 and 8 wt.% M25 graphene nanoplatelets loading.

4.4.3 Optical Characterization of the Composites

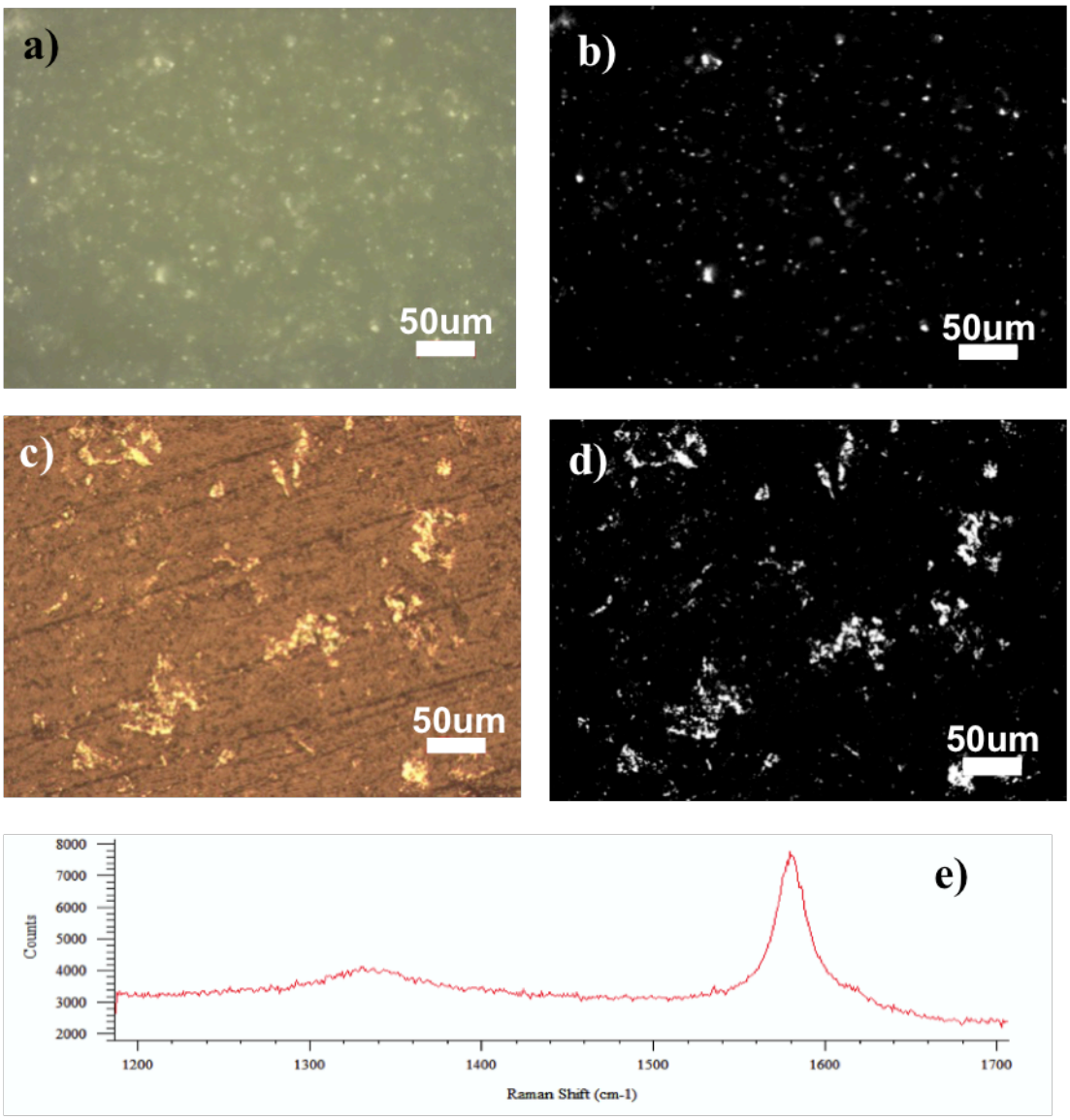

Figure 4.6 Typical optical micrographs of the GNP/epoxy composite samples. (a) is of the uncured, liquid system where (c) is of the cured composite. (b) and d) are digitally processed versions of (a) and (c) respectively where a cut-off mask has been applied. Scale bar is 50 µm. (e) Raman spectrum one of the white regions in (c).

Figure 4.6 a and c show optical images of the uncured and cured epoxy-GNP dispersions respectively. To aid analysis of the images a dark mask using a threshold brightness value was applied to enhance the contrast for easier viewing of the dispersion of M25. Raman spectroscopy confirmed that the white regions in the masked images (b and d) were aggregates of the nanoplatelets, with the Raman spectrum showing the typical D and G bands (Figure 4.6e). Henceforth in the

following discussion, dark mask applied images will be used to compare the dispersion and distribution of GNP.

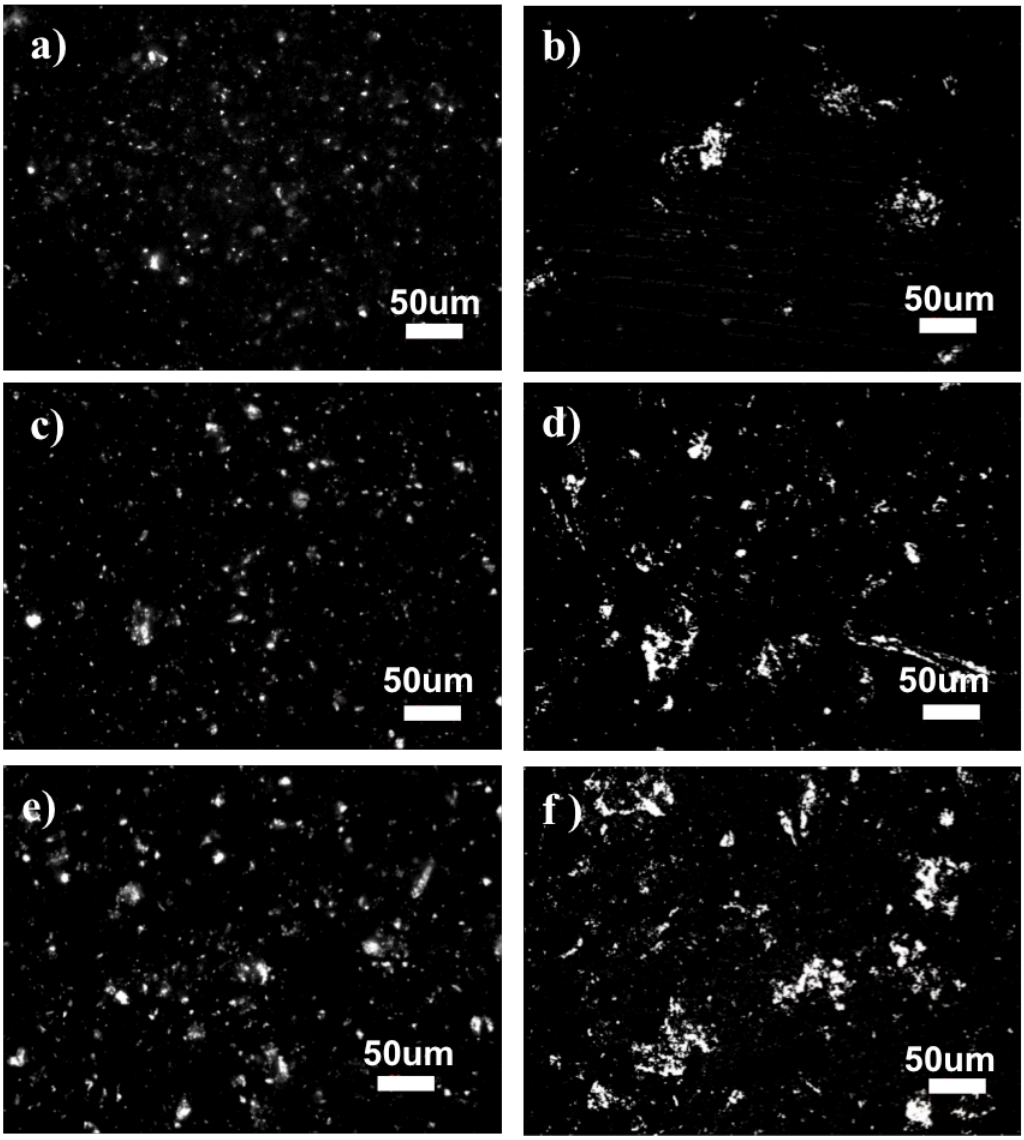

Figure 4.7 Typical dark masked optical images for uncured (a, c and e) and cured (b, d and f) M25/epoxy composites with 1 wt.% (a,b), 5 wt.% (c,d) and 8 wt.% (e,f). All of the images have the same scale bar 50 μm.

It should be noted that the loading is discussed in weight fraction, while the white and black part areas represent (projected) volume fraction. Thus Table 4.1 quotes not the weight, but the volume fractions of the compositions calculated by using the density of the GNP and the epoxy. The percentage of light pixels (*i.e.* aggregates) was found to increase very slightly after curing when compared with uncured samples. Furthermore the percentage of the white pixels was found to be

similar to that overall volume percentage of platelets in the sample, suggesting that all the platelets are represented by the white regions.

Table 4.1 ImageJ analysis of the ratio of the number of white to black pixels in the dark masked optical images in Figure 4.7.

	Black part area (%)	White part area (%)
1 wt.% (0.52 vol.%)[a] Before curing	99.4	0.6
1 wt.% After curing	99.4	0.6
5 wt.% (2.64 vol.%) Before curing	97.6	2.4
5 wt.% After curing	97.5	2.5
8 wt.% (4.29 vol.%) Before curing	95.7	4.3
8 wt.% After curing	95.4	4.6

a: volume fraction of fillers

In the literature [6-7], researchers found that nanofillers tend to attract one another due to the van der Waal's forces and Coulomb's attractions to form aggregates within the uncured polymer, which is not the case in this project. The white parts are uniformly dispersed in the epoxy matrix before curing. But after curing, the white regions are aggregated (Figure 4.7 b, d and f), similar that reported previously by Tang *et al.* [8]. Tang suggested the high temperature for curing induces the graphene nanoplatelets sheets to aggregate. This may be due to the decrease in the polymer's viscosity at the high temperatures prior to the crosslinking. Aggregation is still a significant challenge for preparation nano composite materials, which will have great impact on the final performance, especially mechanical properties.

Apart from aggregation, some researchers [9-10] have also reported that large graphene nanoparticles prefer to settle at the bottom of an epoxy composite moulding due to gravity during the curing treatment. They observed this phenomenon by taking

optical micrographs of cross-section taken at different depths of the sample (Figure 4.8).

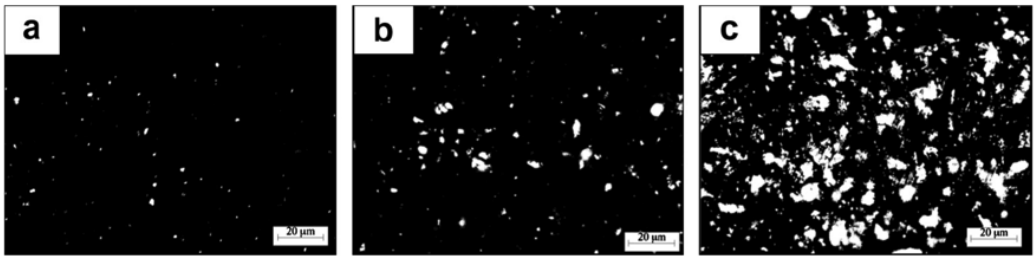

Figure 4.8 Applied mask of graphite/epoxy composites at different sample depths: top (a), middle (b) and bottom (c), ref [10].

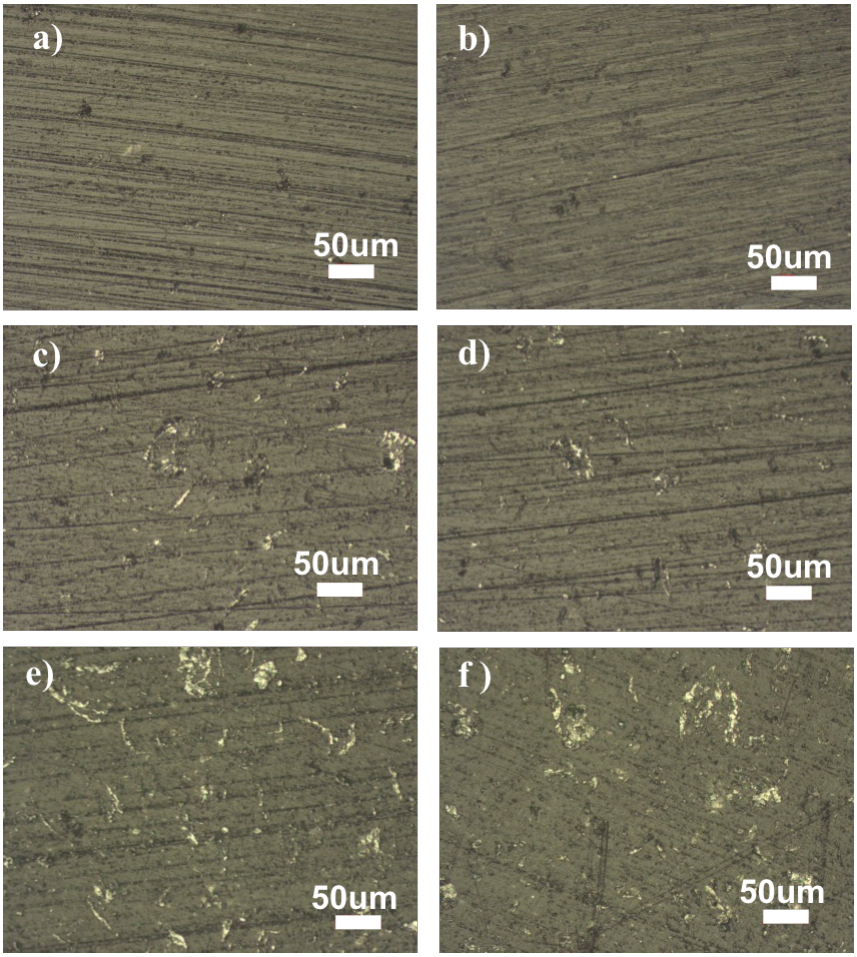

Figure 4.9 Typical optical images of M25/epoxy composites with loading of 1 wt.% (a, b), 5 wt.% (c, d) and 8 wt.% (e, f). Left images: Top side. Right images: Bottom side of the composites.

In order to evaluate the potential settling of the GNPs in this work, optical images of the top and bottom surface of composites were obtained (Figure 4.9). No significant difference was found between the top and bottom surfaces. For example,

analysis using ImageJ found that the white areas in Figure 4.9e and f were 0.53 vol% and 0.46 vol% respectively. It was decided that since no significant difference was found between top and bottom surfaces, there was no need to go to the difficulty of examining a middle slice of the sample. The difference in the settling behaviour between this thesis and the literature can be explained by the GNP having a larger dimensions than that in the reports (<10 μm and 4.5 μm for [9] and [10]), making it more difficult to move in the viscous epoxy system, preventing self-stratification. Also the preparation procedure is different. In this project, degasing is done at 100 °C for 15 mins, which is beneficial for degasing and keep the GNPs uniformly in matrix.

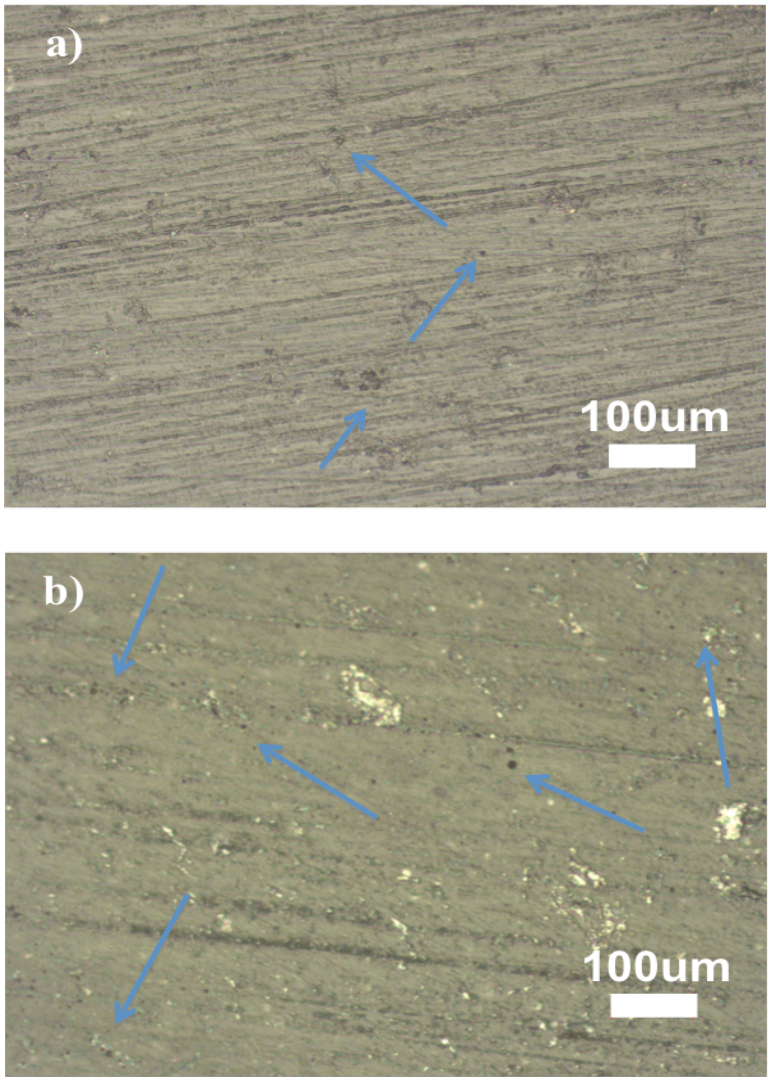

Figure 4.10 Optical images of micro voids within samples containing (a) 1wt.% and (b) 8wt.% M25 GNP.

Figure 4.10 shows micro voids (pointed out by blue arrows) formed in the composites at both low and high GNP loadings due to the formation of gas bubbles. These voids are dispersed unevenly in the composites, mainly along GNP aggregates, which may act as a restriction to gas to removal during degasing. As can be seen, the 8 wt.% loading specimen had more and larger voids than the 1 wt.% loading composite. (NB the scale bar is different in the two images). This observation indicates that the GNP loading and mixture viscosity had significant impacts on the formation of micro voids.

Micro voids were mainly generated during the high rate shear mixing process. After blending, various methods were attempted to remove the bubbles. These methods included:

i. Ultrasounding the mixture in a sonic bath at a temperature of 40 °C. This work worked for the low viscosity mixtures (< 3 wt.%). However, when the mixture became higher viscosity, it took a long time to get rid of the bubbles, during which curing occurred and increased the viscosity even more. In addition, sonication may damage the GNPs and reduce thei r aspect ratio.
ii. Spraying acetone on the surface of the mixture while it was sonicated, with the aim of decreasing the surface tension and hence making the degassing easier and quicker. However, the improvement was not significant, and it may affect the properties of composites.
iii. Sonication at a high temperature (65 °C) in order to lower the viscosity, but the increased temperature led to a higher curing rate.

Eventually, vacuum degassing was selected as the optimum method to degas the samples. Vacuum degassing at room temperature worked well for mixtures with < 4 wt.% nanoplatelets but was not satisfactory at the higher loadings. Hence the vacuum was applied at a 100 °C over a short time (15 min). 15 min was far from long enough time to remove all the gas trapped in the higher viscous mixture, and the remaining gas formed micro voids after curing. The samples with the higher loading had the highest void volume fraction due to their higher viscosity. The micro voids may disrupt the GNP network formed in the epoxy matrix and hence have a significant influence on the electrical, thermal and mechanical properties, which will be discussed in the following chapters.

4.4.4 SEM Characterization of GNP and Composites

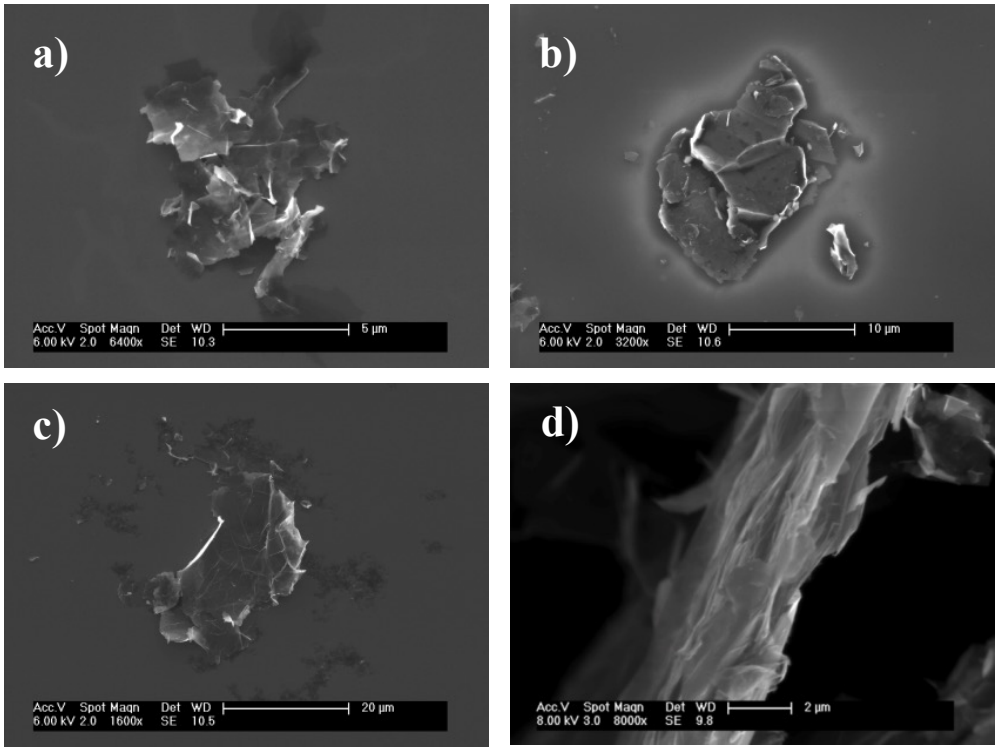

Figure 4.11 SEM images of M5 (a), M15 (b) and M25 (c). Note the scale bars are different for clearer view.

SEM was conducted to provide further information about the shape and structure of GNP. Figure 4.11 shows SEM images of the GNP nanoplatelets on a silicon substrate. The dimensions of M5, M15 and M25 were found to be 5~7 µm, 13 ~17 µm and 23~27 µm respectively upon multiple measurements, which is reasonable consistent with the data provided by the manufacturing company. The GNPs were found to have a wrinkled surface, reduces the GNPs' rigidity and may result in a lower aspect ratio. Also some graphene nanoplatelets can be observed in the images, especially in Figure 4.11d due to van der Waals force between the nanoplatelets. The thickness is in the micron scale, which is much thicker than expected (6-8 nm thickness), leading to greatly reduced aspect ratio than the data from the manufacturer. During composite preparation, no pre-treatment was done to further exfoliate the as-received GNP, this may dramatically affect the resulting electrical and thermal performance, because aspect ratio is critical for forming conductive networks in the epoxy matrix.

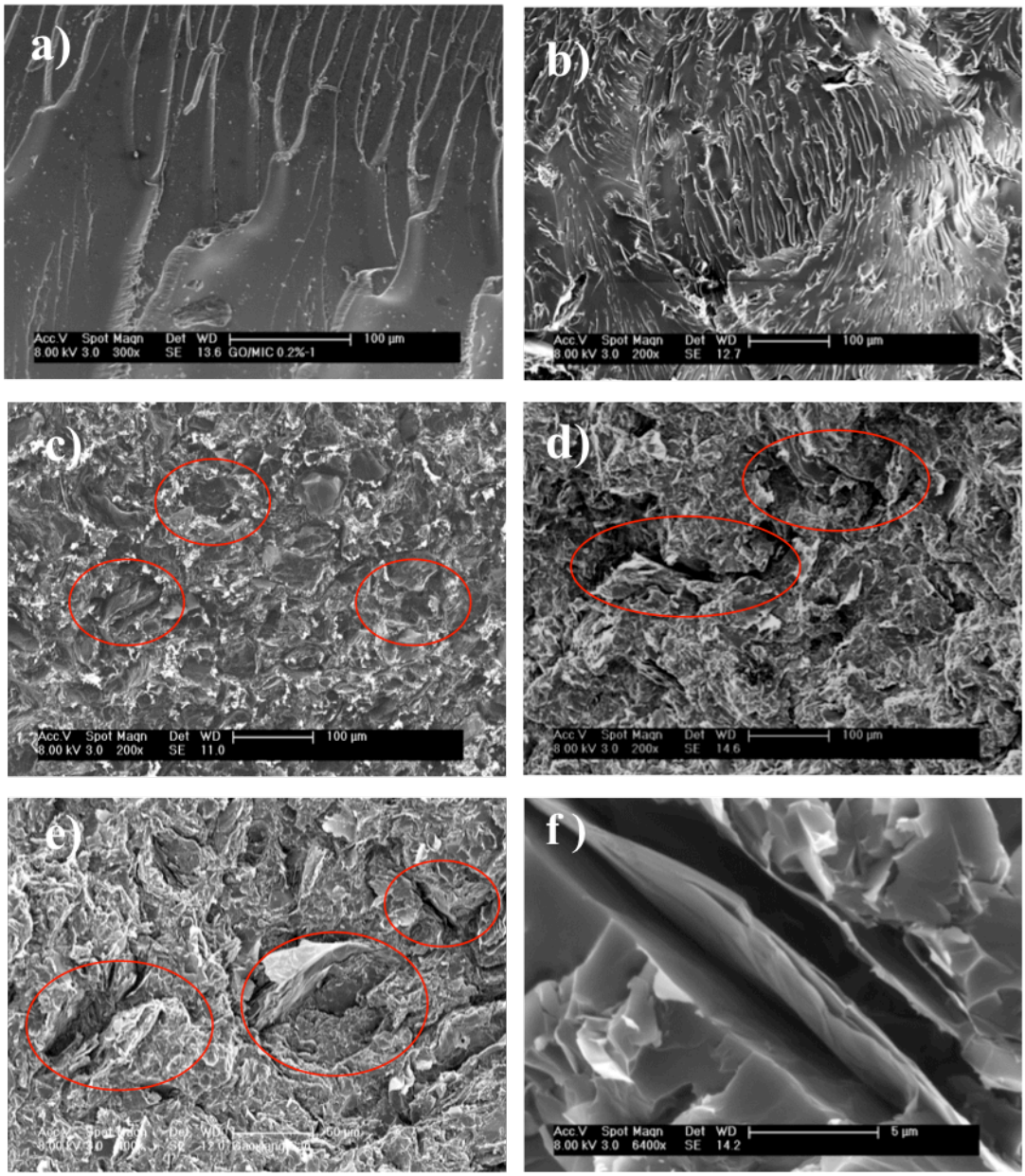

Figure 4.12 SEM images of fracture surfaces of (a) pure epoxy, and M25/epoxy composites prepared by shear mixing with loadings of (b) 0.8 wt.%, (c) 2 wt.%, (d)5 wt.%, (e) 8 wt.%, and (f) an enlarged area of M25 GNP in the composite with 2 wt.% loading.

The fracture surface of neat epoxy was reasonably smooth with a few line patterns, which is a typical characteristic of brittle fracture. The surface of the 0.8wt.% sample was similar to the neat epoxy and shows some aggregation of the GNPs, but most of GNPs were uniformly dispersed and there were not enough GNPs to contact with each other to form conductive network. The 2 wt.% sample has a much higher degree of aggregation. There were also voids (indicated by the red circle areas in Figure 4.12c) that may prevent the entry of hardener into GNP aggregates and

act as stress concentrations, affecting the degree of curing and mechanical performance. The 5 wt.% and 8 wt.% loading samples had the highest degree of aggregation with micro cracks and voids present (indicated by the red circle areas in Figure 4.12d and e). Figure 4.12f demonstrates that the GNP in the epoxy is consistent with the SEM observations of the raw materials.

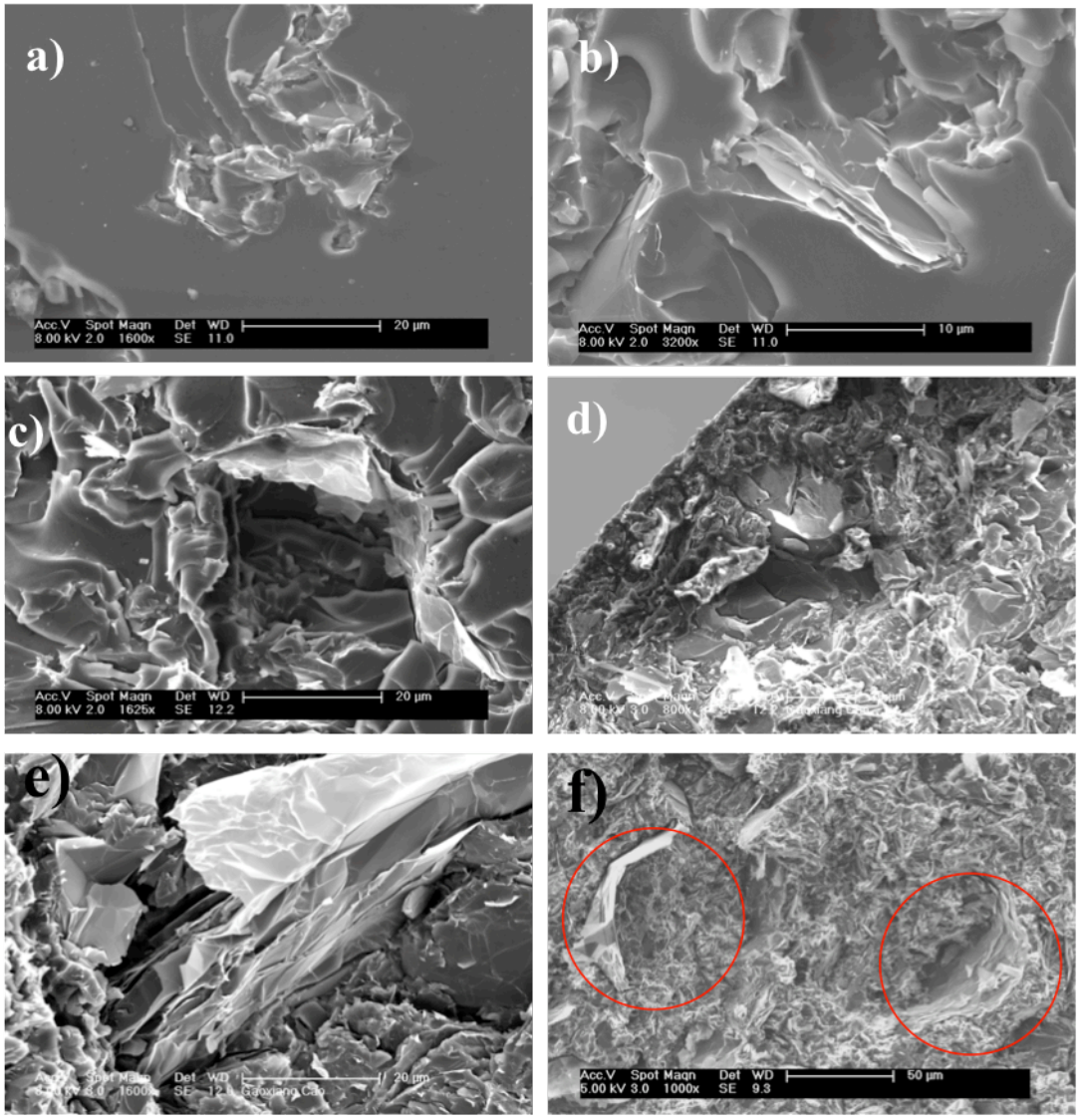

Figure 4.13 GNP interaction with matrix and aggregations in cross section areas of 1 wt.% (a, b), 5 wt.% (c, d) and 8 wt.% (e, f) epoxy/M25 composites prepared by shear mixing.

For the 1 wt.% sample (Figure 4.13a,b), most parts of the surface are smooth with some filler aggregation. The interaction between GNP and matrix was strong, confirmed by the compact structure from SEM image (Figure 4.13 a and b). When the loading rises to 5 wt.%, micro voids appeared due to GNP aggregation. When tension was applied, it is estimated that the efficiency of load transfer from matrix to the GNPs is poor due to the weak attractive force in GNP aggregates. The 8 wt.% sample

(Figure 4.13c, d) has the severest aggregation, which may result in poor mechanical properties. Figure 4.13f shows buckling GNPs due to their high aspect ratio, which makes it easier to curl/bend/buckle or roll up, reducing thus the resistance to the liquid flow.

4.4.5 Polarized Raman Spectroscopy Measurement of GNP Orientation in Epoxy Matrix

In addition to GNP dispersion, which has great effects on the resulting composites, the orientation of GNPs in the matrix is also of great importance. If GNP has a preferred orientation, the composites would be anisotropy due to its two dimensional structure, causing dramatically different mechanical and electrical performance in different direction [11-12]. Raman spectroscopy is a powerful and non-destructive tool to characterize carbon materials for years to study structural features and the presence of defects [13-14]. It has been found that the intensity of the D and G bands follow a $\sim\cos^4$ dependence upon the angle of laser polarization relative to a graphene edge, reaching a maximum value when the polarization direction is parallel to the edge [15-16]. This technique can therefore be used to detect the orientation of GNP in the matrix.

In this work polarized Raman spectra were obtained using Renishaw 1000/2000 spectrometers with a HeNe laser (k = 633 nm) with a laser spot around 1~2 μm diameter, using the so-called 'VV' polarization configuration, where the polarization of incident and scattered radiation are parallel to each other.

The experimental design is shown in Figure 4.14. As can be seen, polarized Raman spectra were obtained from both the transverse section and the top surface of the composite materials using the 'VV' polarization configuration, with the polarization of incident and scattered radiation both parallel to each other. At first, the Raman spectra were obtained when the incident laser was parallel to the Z-axis. The specimens were rotated to angle θ_Z in steps of 10°, and then spectra were obtained from sections of the specimens with the direction of laser propagation along the X-axis. Samples were rotated to angle θ_X in steps of 10°. For each of the specimens prepared by three different methods, five randomly picked points of each side were tested. The points picked should not have any aggregation of GNPs under optical microscopy but should be easy to locate and with a visible Raman peaks of GNP.

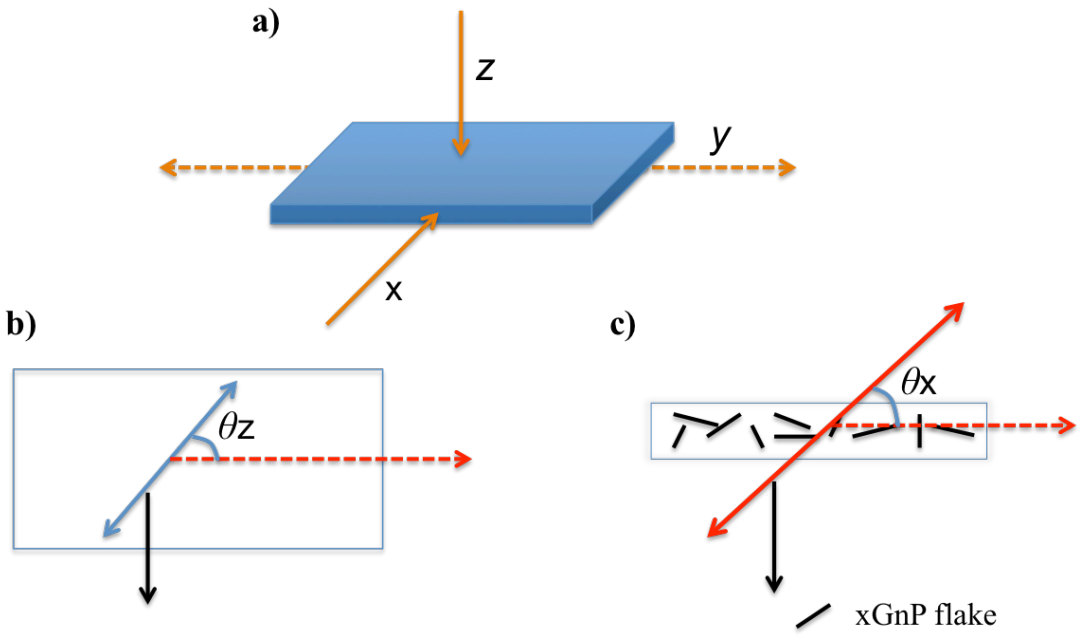

Figure 4.14 Schematic illustration of the geometry of the Raman spectroscopic analysis of the GNP/epoxy nano-composites with (b) the laser beam parallel to z, and (c) the laser beam parallel to x. (The double headed arrows in b and c indicate the axes of laser polarization). The black lines in the rectangle of c represent GNP flakes dispersed in the matrix.

Figure 4.15 shows the results of polarized Raman spectral analysis of GNP (M25) in the epoxy matrix prepared by shear mixing. The intensity of the G band (I_G) was chosen as an indication of orientation as M25 has a very weak D band, and the strongest peak was normalized as 1.

It is clearly seen that I_G is independent of θ_Z and θ_X, no matter the direction of laser propagation parallel to the Z-axis or X-axis, indicating that there is no preferred orientation for GNPs in the epoxy matrix, which has also been shown by measuring the same electrical conductivity along different directions (this will be confirmed by fitting to the Halpin-Tsai mechanical model in the next chapter). However, there are reports showing that during the curing process graphene nanoplatelets with a large aspect ratio tend to lie regularly in the resin because of the surface tension, indicating a self-orientation [10, 17-18]. Song *et al.*[18] and Kim and Makosco [17] have confirmed that this effect of self-orientation is mainly in highly concentrated composites with high graphene nanoplatelets concentration. Prolongo *et al.* [10] showed that self-orientation of nanoparticles could lead to a structural anisotropy of composites by measuring the coefficient of thermal expansion (CTE) in two different

directions and obtaining different values. The different results may be due to the different GNPs used. In this work, M25 of 25 μm in lateral dimensions was used compared to the 4.5 μm graphene nanoplatelets used in Prolongo's experiments, in which the same epoxy resin Araldite LY556 and hardener as mine were used. It takes more energy and time to orientate in a preferred direction as the GNPs become larger.

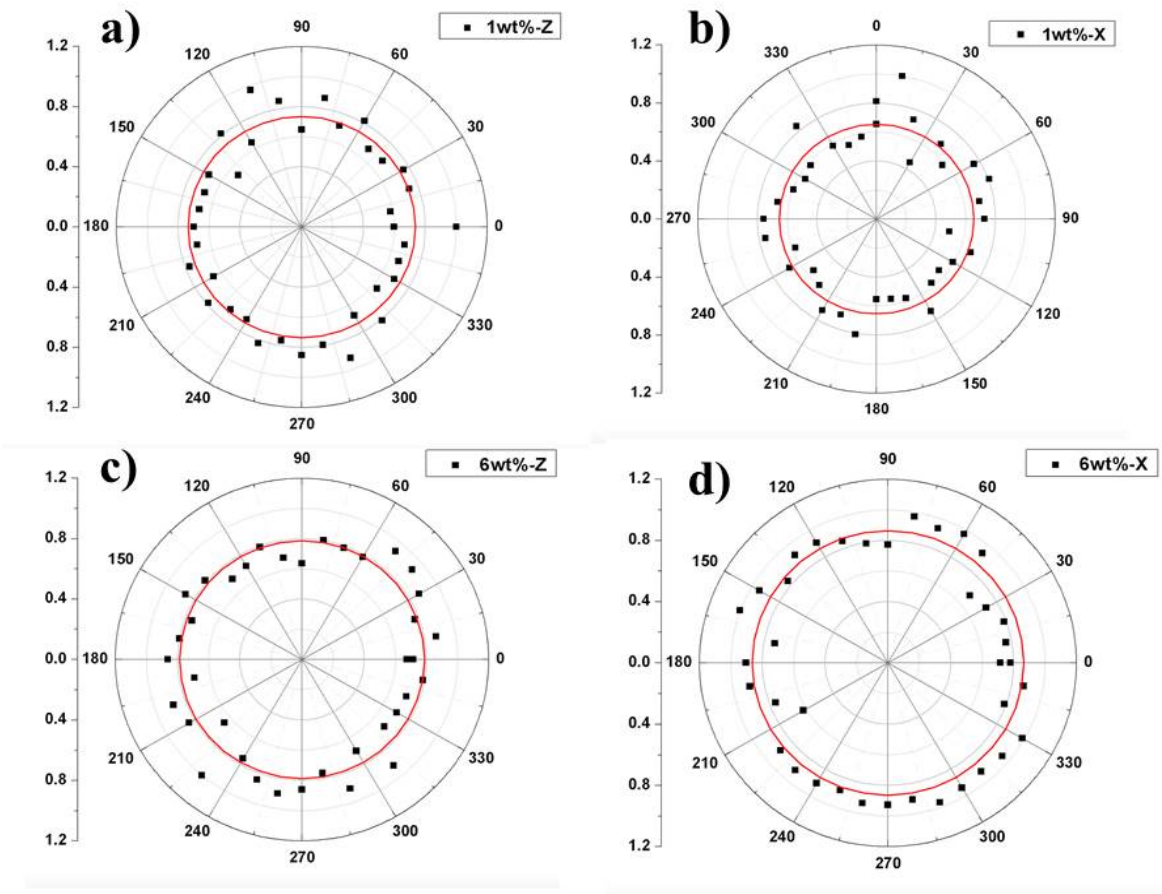

Figure 4.15 (a,c) I_G (the intensity of the G band) variation with the laser beam parallel to the Z-axis as a function of the angle θZ. (b,d) I_G variation with the laser beam parallel to the X-axis as a function of the angle θX. Samples were prepared by shear mixing.

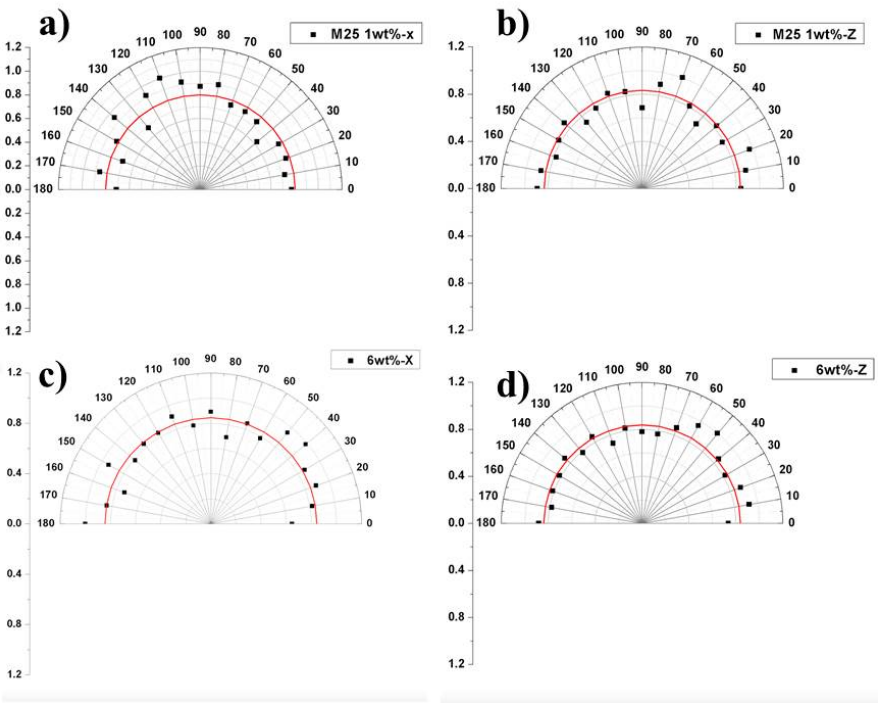

Figure 4.16 Fig (a,c) I_G variation with the laser beam parallel to the Z-axis as a function of the angle θ_Z. (b,d) I_G variation with the laser beam parallel to the X-axis as a function of the angle θ_X. Samples were prepared by three-roll milling with a 0.08 mm gap.

The results of polarized Raman spectral analysis of GNP in the epoxy matrix prepared by three-roll milling (0.08 mm gap between rollers) is shown in Figure 4.16. The I_G is independent of θ_Z and θ_X, suggesting a non-prefered distribution of GNP in epoxy. It is expected that a composite mixed by three-roll milling might show more uniform dispersion, or even a self-orientated distribution of GNP considering the small gap between the rollers. However, the results show no big differences in dispersion between the two methods. This can be explained in that the small roller gap (0.08 mm) is still larger than 25 μm and thus cannot force the GNP to align.

4.5 Comparative Study of Composites Prepared by Three-roll Milling and Solvent-assisted Mixing

The rheology behaviour, optical GNP dispersion and Raman spectroscopy for GNP orientation in composites fabricated by three-roll milling and solvent-assisted mixing was not studied due to time restraints. However, SEM was used to understand the differences in the microstructures between all three preparation methods.

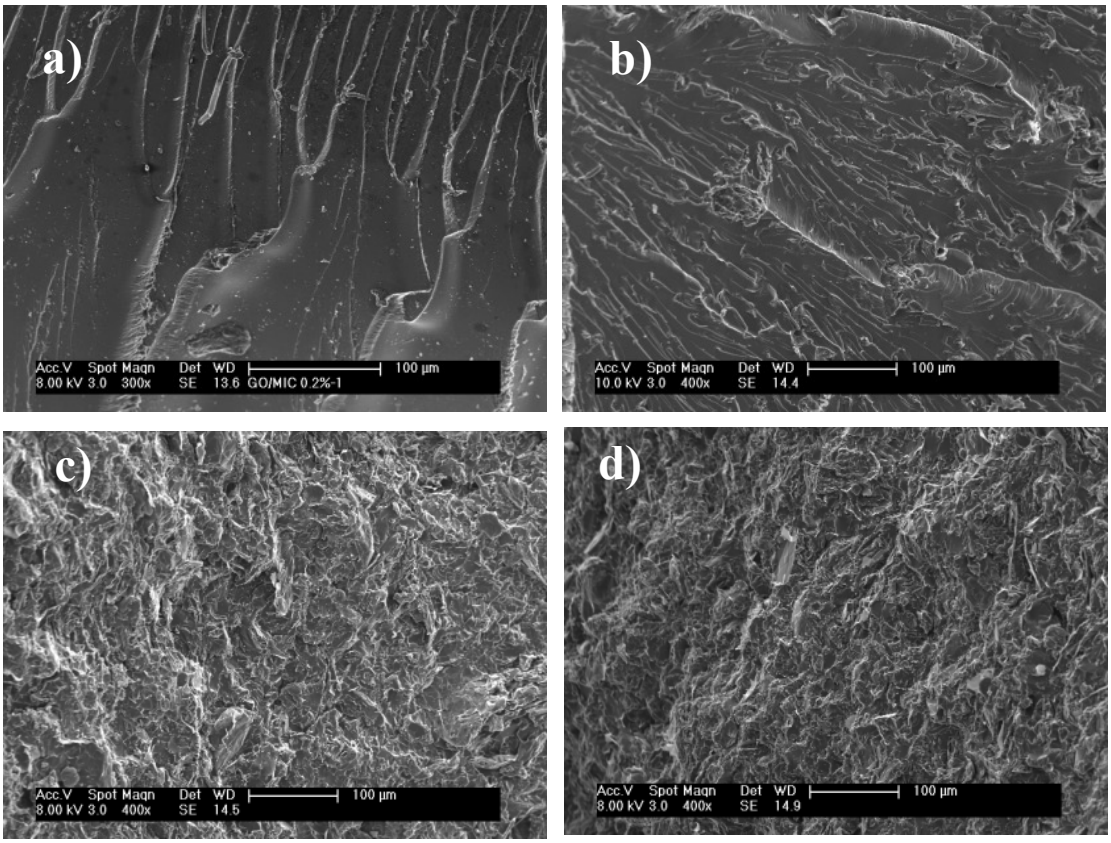

Figure 4.17 SEM images of (a) pure epoxy, and M25/epoxy composites prepared by solvent-assisted blending with loadings of (b) 0.8 wt.%, (c) 5 wt.%, (d) 8 wt.%.

Figure 4.17 shows the fracture surfaces of composite samples made by solvent-assisted blending. The lowest loading sample (0.8 wt.%) has a similar smooth surface to the equivalent shear mixed sample. As loading increases, aggregation can be clearly observed. However, the aggregation is less severe when compared with equivalent samples fabricated by shear mixing. The solvent played an important role in more uniformly distributing the GNPs in the epoxy resin, which may greatly affect the resulting properties of the composites.

SEM images of the fracture surfaces of three-roll mill mixed samples (Figure 4.18) show a surface roughness between that of the shear mixed and solvent-assisted blended samples. The small gap between the rollers gives an advantage over shear mixing in dispersing GNP uniformly in epoxy matrix, but not as good as solvent-assisted blending. Through investigating the surfaces of samples prepared by these three different methods, it is interesting to find out that there are mainly four types of GNP aggregation.

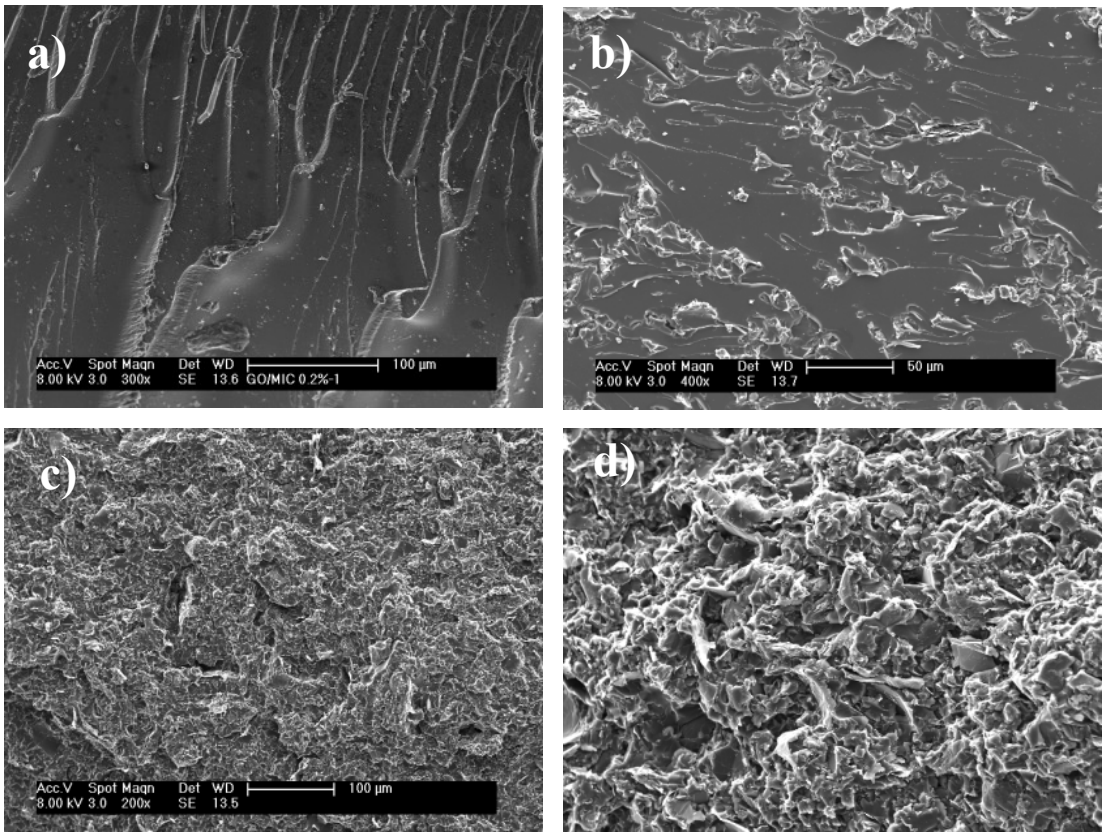

Figure 4.18 SEM images of (a) pure epoxy, and M25/epoxy composites prepared by three-roll mill mixing with loadings of (b) 0.8 wt.%, (c)5 wt.%, (d) 7 wt.%.

Studying the GNP types may give us some insight into the mechanical properties of composites. Figure 4.19 showed four types of GNP aggregate found in all three methods. The first shown in Figure 4.19a shows the graphene nanoplatelets layers parallel to the applied tension direction, which in theory gives the best mechanical reinforcement due to the strength of the carbon atomic layers along this direction. Figure 4.19b shows another completely different GNP aggregate, whose graphene nanoplatelets layer stacking orientation is perpendicular to the tension direction. In this case, when a stress is applied, the GNPs will easily part due to the weak forces between graphene nanoplatelets layers, and this type of aggregate can barely contribute to the reinforcement of the epoxy matrix. The third type of aggregation (Figure 4.19c) shows a layer stacking direction between the first and second type, and is expected to have moderate load transfer efficiency. Figure 4.19d displays an aggregation, combining three types of aggregates mentioned before. It is like a long crack, which can severely compromise the mechanical properties of the composite.

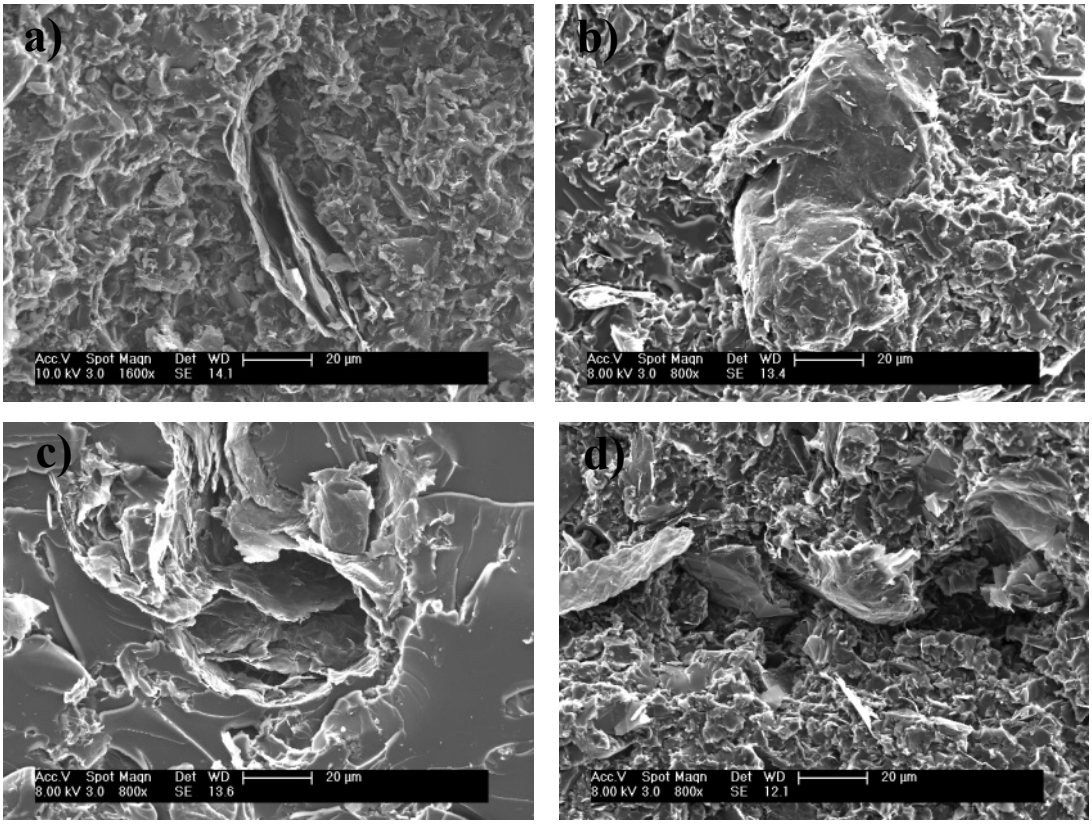

Figure 4.19 Various GNP aggregate types found in composites.

4.6 Summary

The structure of a composite has a strong relationship with the final properties. Therefore, this chapter mainly aimed to investigate the structure of the original GNPs, as well as the dispersion, orientation and aggregation of GNP in the matrix. It was found that the dimensions of the as-received GNPs are consistent with the data sheets provided. When GNP was dispersed in epoxy, the viscosity increases significantly, which may produce difficulty for processing. The curing processing causes GNP to aggregate and reduces the aspect ratio largely, which may greatly compromise the properties. Polarized Raman spectroscopy showed the GNPs were randomly distributed in the epoxy matrix.

The next chapter presents the characterisation of the properties of the composites and the discussion of the results based on observations of this chapter.

References

1. Hough, L. A.; Islam, M. F.; Janmey, P. A.; Yodh, A. G., Viscoelasticity of Single Wall Carbon Nanotube Suspensions. *Physical Review Letters* **2004,** *93* (16), 168102.
2. Othman, R. N. Synthesis and Characterisation of Hybrid Carbon - Nanotube Silica Microparticles. PhD thesis, The University of Manchester, **2012**.
3. Kinloch, I. A.; Roberts, S. A.; Windle, A. H., A rheological study of concentrated aqueous nanotube dispersions. *Polymer* **2002,** *43* (26), 7483-7491.
4. Dae-Weon, K.; Eui-Yun, J.; Seung-Min, L.; Wal-jun, K.; Jong-Hoon, L.; Jacob, K., Improvement of Carbon Nanotubes using Cryogenic Treatment. *Japanese Journal of Applied Physics* **2007,** *46* (12L), L1096.
5. Nguyen Van, Q.; Nguyen Duc, H.; Myungchan, A.; Yousuk, C.; Dojin, K., A high-performance triode-type carbon nanotube field emitter for mass production. *Nanotechnology* **2007,** *18* (34), 345201.
6. Ma, P.-C.; Mo, S.-Y.; Tang, B.-Z.; Kim, J.-K., Dispersion, interfacial interaction and re-aggregation of functionalized carbon nanotubes in epoxy composites. *Carbon* **2010,** *48* (6), 1824-1834.
7. Kim, S. W.; Kim, T.; Kim, Y. S.; Choi, H. S.; Lim, H. J.; Yang, S. J.; Park, C. R., Surface modifications for the effective dispersion of carbon nanotubes in solvents and polymers. *Carbon* **2012,** *50* (1), 3-33.
8. Tang, L.-C.; Wan, Y.-J.; Yan, D.; Pei, Y.-B.; Zhao, L.; Li, Y.-B.; Wu, L.-B.; Jiang, J.-X.; Lai, G.-Q., The effect of graphene dispersion on the mechanical properties of graphene/epoxy composites. *Carbon* **2013,** *60*, 16-27.
9. Yasmin, A.; Luo, J.-J.; Daniel, I. M., Processing of expanded graphite reinforced polymer nano-composites. *Composites Science and Technology* **2006,** *66* (9), 1182-1189.
10. Prolongo, S. G.; Moriche, R.; Sánchez, M.; Ureña, A., Self-stratifying and orientation of exfoliated few-layer graphene nanoplatelets in epoxy composites. *Composites Science and Technology* **2013,** *85*, 136-141.
11. Lee, C.; Wei, X.; Kysar, J. W.; Hone, J., Measurement of the Elastic Properties and Intrinsic Strength of Monolayer Graphene. *Science* **2008,** *321* (5887), 385-388.
12. Malard, L. M.; Pimenta, M. A.; Dresselhaus, G.; Dresselhaus, M. S., Raman spectroscopy in graphene. *Physics Reports* **2009,** *473* (5–6), 51-87.
13. Wang, F.; Drzal, L.; Qin, Y.; Huang, Z., Mechanical properties and thermal conductivity of graphene nanoplatelet/epoxy composites. *Journal of Materials Science* **2015,** *50* (3), 1082-1093.
14. Kalaitzidou, K.; Fukushima, H.; Miyagawa, H.; Drzal, L. T., Flexural and tensile moduli of polypropylene nano-composites and comparison of experimental data to Halpin-Tsai and Tandon-Weng models. *Polymer Engineering & Science* **2007,** *47* (11), 1796-1803.
15. Gupta, A. K.; Russin, T. J.; Gutierrez, H. R.; Eklund, P. C., Probing graphene edges via Raman scattering. *ACS Nano* **2009,** *3* (1), 45-52.
16. Li, Z.; Young, R. J.; Kinloch, I. A.; Wilson, N. R.; Marsden, A. J.; Raju, A. P. A., Quantitative determination of the spatial orientation of graphene by polarized Raman spectroscopy. *Carbon* **2015,** *88*, 215-224.

17. Kim, H.; Macosko, C. W., Processing-property relationships of polycarbonate/graphene composites. *Polymer* **2009,** *50* (15), 3797-3809.
18. Song, Y.; Yang, C.; Liu, D.; Lin, Y.; Nan, C. W., Self-orientation of graphite-nanoplates induces anisotropy of nanoplates-epoxy composites. *Ceramics International* **2012,** *38, Supplement 1*, S91-S94.

CHAPTER 5 MECHANICAL PROPERTIES OF GNP COMPOSITES

5.1 Introduction

The structure of the GNP nanoplatelets and the GNP-epoxy composite were studied in the previous chapter using a combination of AFM, XRD, SEM and Raman spectroscopy. This chapter focuses on the mechanical properties of these composites, with the *in-situ* Raman spectroscopy being used to assess the degree of stress transfer on the nanoscale, DMTA being used to measure the viscoelastic properties and tensile testing to obtain the stress-strain behaviour. Analytical models are then applied to the data obtained.

5.2 *In-situ* Raman Spectroscopy to Evaluate the Degree of Stress Transfer

The degree of stress transfer from the matrix to the nanoplatelets strongly influences the degree of reinforcement that the nanoplatelets impart to the composite. Raman spectroscopy measures the energy of the phonons in a material. As a material undergoes strain, the bond energy changes, leading to the Raman bands shifting to lower wavenumbers with increasing strain. In general, the rate of the shift in the Raman band with strain is proportional to the effective modulus [1-2]. The G band and 2D band in carbon materials [3] have been used in carbon-based reinforcement [4-7], with a shift rate of 60 cm^{-1}/% corresponding to a 1 TPa effective modulus.

In situ Raman deformation analysis of the nano-composites was conducted using a Renishaw 2000 Raman spectrometer system with a HeNe laser (633 nm excitation). A neat epoxy resin beam was prepared and then an epoxy/M25 film mixed by a high shear mixer was coated on the surface. The specimens were tested in a four-point bending rig placed on the Raman microscope stage. The surface strain was measured using a resistance strain gauge bonded to the specimen surface using cyanoacrylate adhesive. Force is applied through four-point bending to deform the beams stepwise (0.1 % strain each time) and the Raman spectra were collected from

the central area of the nano-composite at each strain level. The polarization of the incident laser was parallel to the tensile direction.

For the Raman test, the lower aggregations of composite samples are, the better the results of load transfer would be. Therefore only 0.5 wt.% and 1 wt.% loading composites were tested. For each of the specimens, three randomly picked points on the top surface were tested. The points chosen did not have apparent any aggregation of GNPs under optical microscopy but did give GNP Raman spectra.

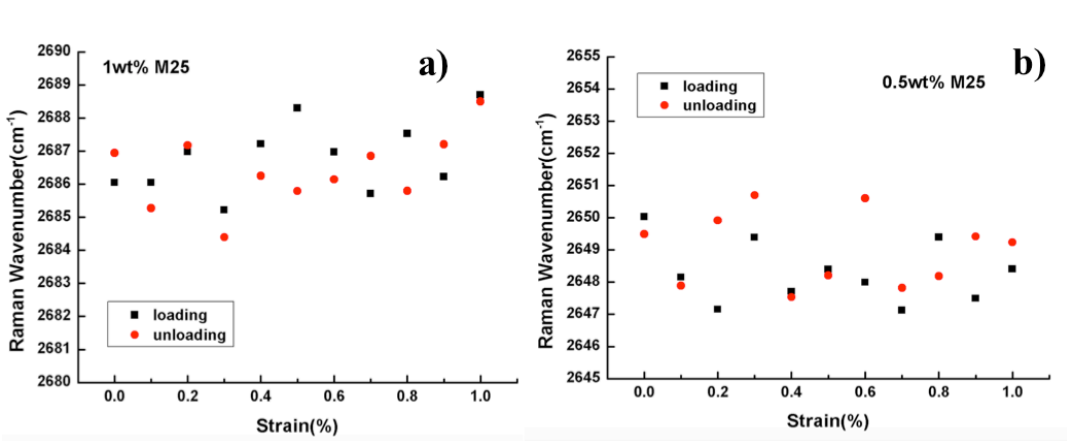

Figure 5.1 The position shift of the 2D band with as a function of strain for the 1 wt.% (a) and 0.5 wt.% (b) epoxy/M25 nano-composites. The composites were loaded stepwise to 1 % strain follow by step-wise unloaded.

Figure 5.1 shows the Raman shift of the G band for the 1 wt.% (a) and 0.5 wt.% epoxy/M25 nano-composites. There was no apparent shift in the Raman spectra upon deformation of the sample, with an apparent random scatter in the 2D band's position. The largest difference between the wavenumber from 0 % strain to 1 % strain is only about 4 cm^{-1}, which may be due to the laser spot drifting from one platelet to another, with the platelets varying in their residual strain. It can thus be concluded that the load transfer between the M25 GNP and the matrix is quite poor. It is known that functionalized graphene-based fillers have strong interaction between filler and matrix due to covalent bonding. However, this is not the case for pristine GNP. The smooth surface of GNP makes it hard to form strong bonding with polymer matrix leading to poor interfacial interaction. Also the slippage between graphene nanoplatelets layers of GNP due to its weak in-plane forces may be another reason for the results, as no stress can be transferred to the internal graphene nanoplatelets layers.

Given that no stress transfer was observed in these high-shear mixed samples, and that similar GNP and matrix interactions and GNP orientations were observed by SEM for the three-roll mill mixed and solvent-assisted mixed samples, only shear mixed composites were studied by Raman for stress transfer.

5.3 Dynamic Mechanical Thermal Analysis

Some reports [8-10] suggested that the mechanical properties of epoxy composites have been slightly compromised with incorporation of nano-carbon fillers, in that T_g drops a little when compared to pure epoxy. For the epoxy system used in this project, it is necessary to understand how the GNP addition and loading level will affect the dynamic mechanical properties of GNP/epoxy composites as a function of temperature. Thus, DMTA was used to measure the modulus and T_g of the composites as a function of loading and processing technique. The storage modulus (E') and loss factor (tan δ) profiles of the GNP based composites are compared in Figure 5.2 and Figure 5.3, respectively.

Only one representative DMTA curve for each composite has been plotted for clarity, although at least three samples were tested (giving a figure of one sample showing all three data). The storage modulus was found to drop slightly with increasing temperature until 150 °C, after which E' decreased by approximately two orders of magnitude until T = 170 °C, after which E' remains almost constant with temperature. As can be seen in the glassy region, the incorporation of the GNP into the epoxy, E' increased and reached the highest values with the addition of 8 wt.% M5. It is interesting to notice that there was no significant difference between the moduli of the M5 and M25 composites despite the factor of five differences in their aspect ratio. Some researches showed that bigger aspect ratio benefited the improvement of mechanical properties [11-13], which is not the case in this project. This is probably due to aggregation (shown by SEM in Figure 4.11) of the GNP reducing the aspect ratio significantly, minimizing its effects on mechanical properties.

The samples prepared by solvent-assisted and three-roll mill mixing (0.15 mm roller gap), had higher moduli than equivalent samples prepared by high shear mixing. This difference can be explained by the more uniform distribution of GNPs in

the matrix due to the used solvent and the small gap between rollers (shown by SEM images Figure 4.17 and Figure 4.18).

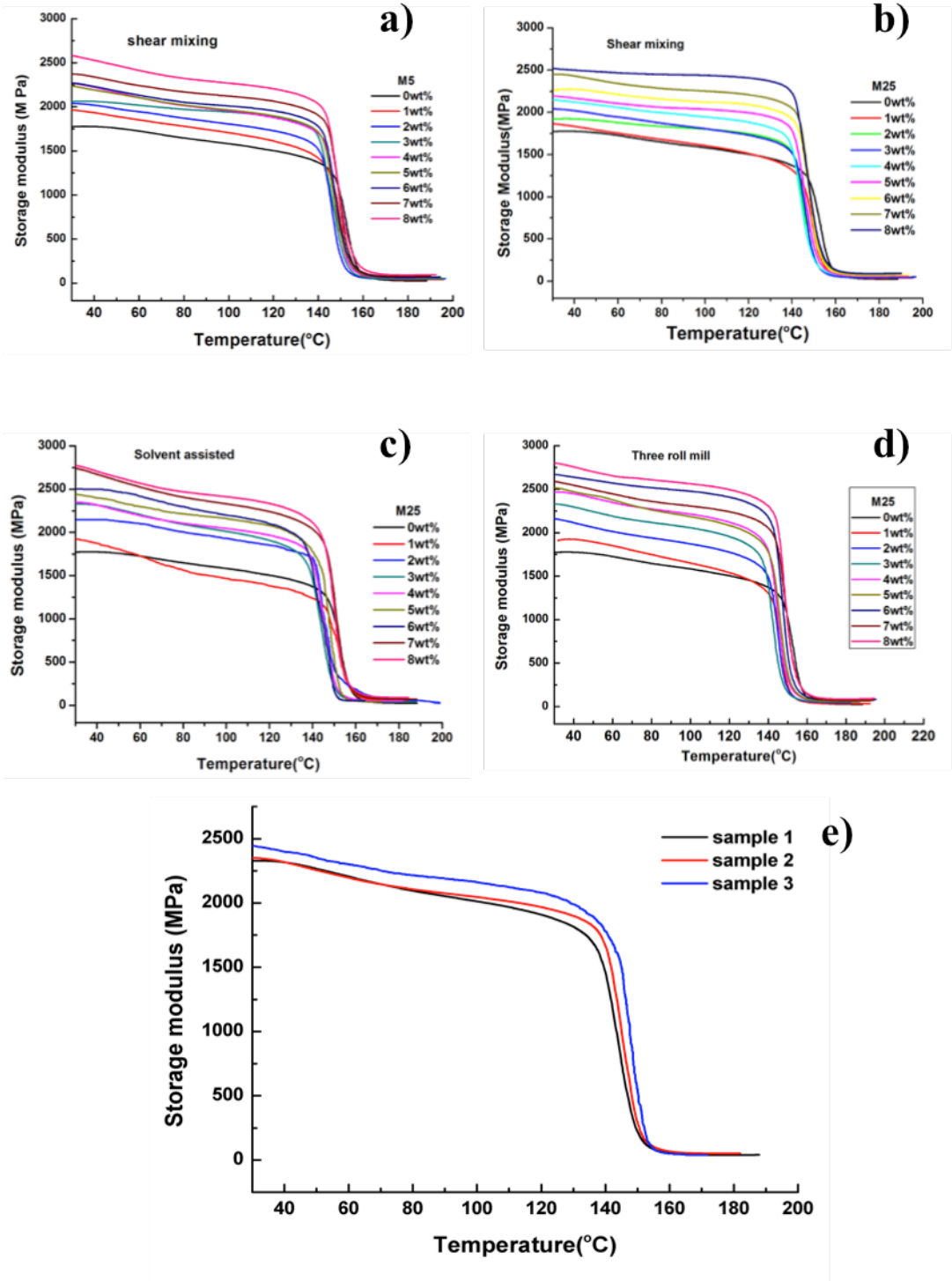

Figure 5.2 Storage modulus for M5 (a) and M25/epoxy (b) composites prepared by shear mixing, and M25/epoxy composites prepared by solvent-assisted mixing (c) and three-roll mill mixing (d); (e) shows three storage modulus curves of 7 wt.% M5/epoxy composites.

The largest improvement in storage modulus was found for the 8 wt.% M25/epoxy sample prepared by three-roll mill mixing, with a 58 % increase from 1.8 GPa (neat epoxy) to 2.8 GPa (8 wt.%) at 35 °C. Solvent-assisted samples have similar enhancement with the highest increase of 56.6 % for the 8 wt.% sample. The rise in E' is larger than that reported in [11], which also use the GNP fillers in an epoxy matrix. This difference is probably due to the stiffness of the matrix. To clarify this aspect, a systematic investigation on the effect of matrix stiffness and addition of carbon nanofillers on the mechanical properties of composites was done by Her and Yeh [14]. In their experiments, the stiffness of the epoxy matrix was controlled by changing the ratio of the epoxy to hardener. Experimental data showed that the reinforcement efficiency of multi-walled carbon nanotubes decreased upon increasing the stiffness matrix. Ci and Bai in [15] also found the same effect. The authors also noted that the interface between carbon nanotubes and the matrix in the stiff composite was poor, and hence the nanotubes contributed less the mechanical properties of the composite.

Figure 5.3 shows the loss factor (tan δ) curves for both the M5 and M25 epoxy composites, with the peak being taken as glass transition temperature. The value of T_g has a close relationship with the crosslink density; in that the better the degree of crosslinking occurs, the higher the T_g achieved. Crosslinking is very important for the mechanical properties of polymer, therefore it is important to investigate the effect that the incorporation of GNP will have on the T_g of the resultant composites.

Overall, the T_g decreased with increasing loading for the both the M5 and M25 composites. For the M5/epoxy samples, T_g shifted to lower values with increasing loadings until 3 wt.%, after which it began to rise. However even for the highest loading (8 wt.%), T_g (165.7 °C) is still lower than neat epoxy (167.2 °C). This drop in the T_g is believed to be due to the formation of GNP aggregates. Liu *et al.* [10] investigated the effect of nano- and micro- fillers on the T_g and showed that aggregated fillers are not only coated in epoxy but epoxy also penetrates the aggregates, which inhibits the diffusion of the hardener molecules into the resin during mixing, affecting the extent of curing, and consequently lowers T_g. However, the addition of rigid fillers also restrains the movement of the polymer chains, which in turn will increase the T_g. The poor interaction between fillers and matrix (as shown in SEM images in Figure 4.13 and Figure 4.19), though, means that this is not expected to contribute significantly to the T_g of the composites present herein. Thus at

lower filler fractions, the crosslinking density effect dominates, lowering T_g, leading to a drop in T_g; when the loadings increased, the restraining effects dominates and increases the T_g.

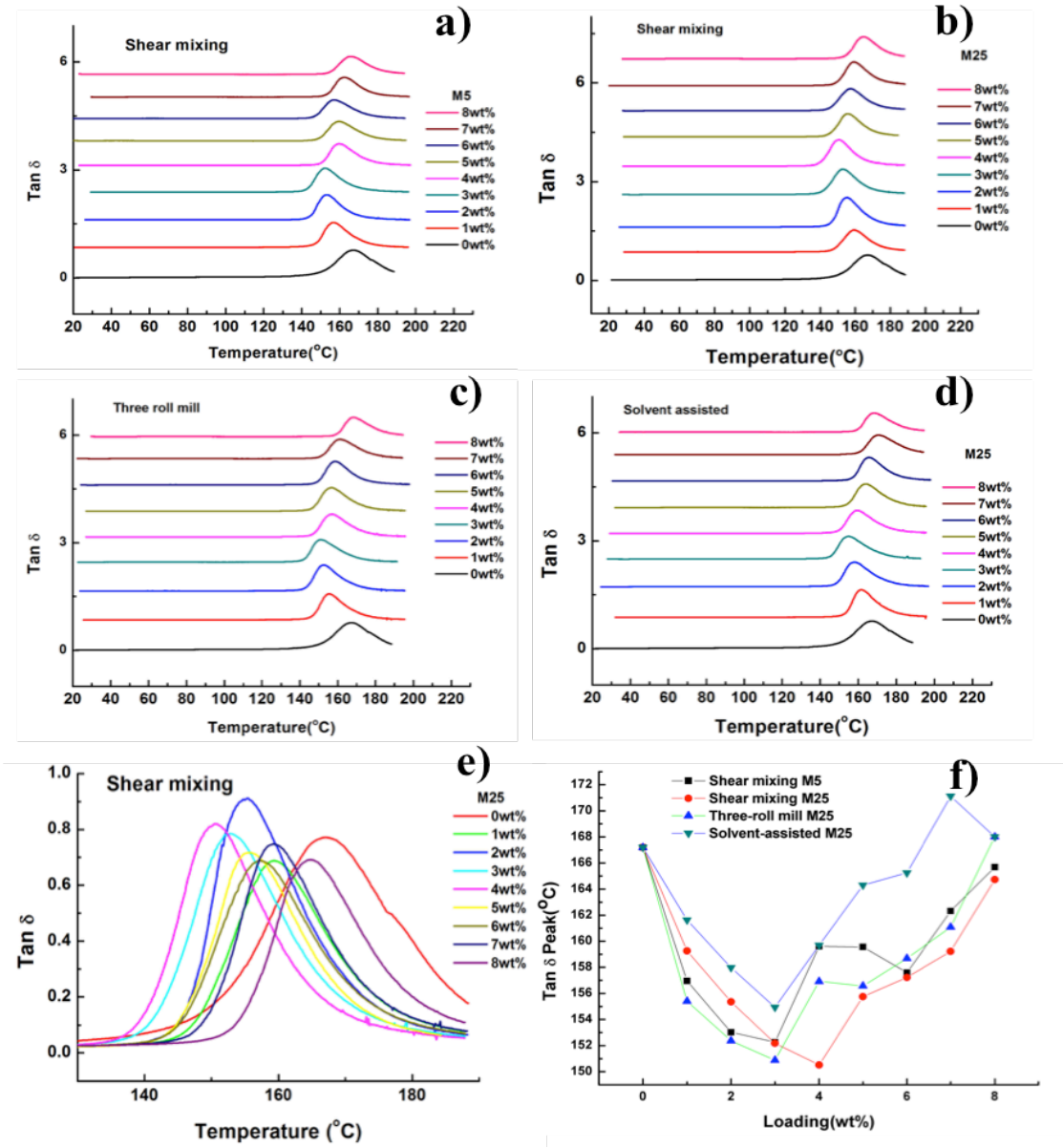

Figure 5.3 Loss factor (tan δ) curve for M5 (a) and M25 (b) composites prepared by shear mixing, and M25 based composites fabricated by three-roll mil mixing (0.15mm roller gap) (c) and solvent-assisted blending (d). The loss factor (tan δ) profile (e) for M25/epoxy to show the peak height and peak width at half height. (f) Tan δ peaks as a function of filler loadings.

Similar trends are observed for the three-roll mill and solvent-assisted mixing samples, with the difference that in these samples, the highest loadings of GNPs lead to the T_g increasing beyond that of the neat epoxy. Although a relatively large number of aggregations of GNP were observed in the solvent-assisted and three-roll mill

samples, the aggregation size is smaller compared to the shear mixed specimen (as shown in Figure 4.17 and Figure 4.12). Therefore, the crosslinking density is not dramatically jeopardized and smaller aggregations contribute more t o the restraint of polymer chain movements, causing increase of T_g. All samples exhibit similar trends of T_g with a large drop at low loadings, followed by gradual increase afterwards (as shown in Figure 5.3f).

Table 5.1 Summary of tan δ peak position and peak height from DMTA.

Loading (wt.%)	Shear mixing M5			Shear mixing M25		
	Peak position (°C)	Half-Peak width (°C)	Peak height	Peak position (°C)	Half-Peak width (°C)	Peak height
0	167.2±1.5	22.0±0.8	0.77±0.11	167.2±1.5	22.0±0.8	0.77±0.11
1	156.9±2.4	17.5±0.9	0.71±0.08	159.3±2.3	16.9±1.2	0.69±0.05
2	153.0±2.5	15.0±1.2	0.72±0.10	155.4±2.0	14.6±1.2	0.91±0.05
3	152.3±3.1	16.1±1.3	0.68±0.12	152.2±3.2	15.9±1.4	0.78±0.09
4	159.6±2.3	15.6±1.5	0.63±0.09	150.5±2.7	15.2±2.3	0.82±0.07
5	159.6±1.8	14.1±2.1	0.57±0.13	155.8±2.3	15.2±2.1	0.72±0.11
6	157.6±3.4	16.3±1.4	0.55±0.13	157.2±3.1	17.1±2.0	0.69±0.10
7	162.3±3.1	16.2±2.3	0.58±0.15	159.2±3.2	15.6±1.9	0.75±0.12
8	165.7±2.6	15.6±2.4	0.53±0.17	164.7±2.5	17.4±1.7	0.69±0.13
	Three-roll mill M25 (0.15mm roller gap)			**Solvent-assisted M25**		
0	167.2±1.5	22.0±0.8	0.77±0.11	167.2±1.5	22.0±0.8	0.77±0.11
1	155.4±2.3	16.5±0.7	0.74±0.10	161.6±1.7	17.3±0.5	0.79±0.05
2	152.4±2.5	16.2±1.1	0.74±0.07	157.9±1.9	15.3±1.5	0.70±0.09
3	150.9±2.1	17.1±1.4	0.65±0.11	154.9±2.3	16.2±1.0	0.65±0.13
4	156.9±1.8	16.1±1.5	0.66±0.14	159.7±2.1	16.0±1.3	0.66±0.12
5	156.6±1.8	15.1±1.7	0.68±0.09	164.3±2.5	14.9±2.5	0.67±0.15
6	158.7±2.6	15.7±1.7	0.68±0.09	165.2±3.2	15.9±2.0	0.68±0.09
7	161.1±2.7	16.7±2.1	0.57±0.13	171.1±3.1	16.2±1.6	0.58±0.12
8	168.0±3.2	16.3±2.0	0.56±0.15	168.0±2.5	16.9±1.9	0.55±0.11

The ratio of the loss modulus to the storage modulus, i.e. the tan δ peak height, in hybrid composites have been reported as an indirect measurement of the segmental

mobility [16], with higher tan δ peak height being related to higher segmental mobility. As can be seen in Table 5.1, the tan δ peak height dropped from neat epoxy to GNP loaded samples, indicating that the addition of the GNP reduced the polymer chain movement, consistent with previous discussion. The width of tan δ peak at half height also drops upon filler addition, indicating a more heterogeneous system is obtained.

5.4 Tensile Testing

Figure 5.4 shows typical stress-strain curves for the neat epoxy and composites filled with the M5 and M25 nanoplatelets. Typically, the stress increased linearly with strain until fracture, which is brittle fracture behaviour. This brittleness correlates to the fracture type observed in the SEM images in Chapter 4. A closer inspection reveals that the slope in these curves decreases with the strain, meaning reduction of elastic modulus. Vega *et al* [17] have found that thermoset resins exhibit elastic nonlinear behaviour before yielding. Moreover, viscoelastic effects occur in epoxy-based composites, even at relatively low strain conditions. According to Northolt's theory [18], the stress acting on the domain in the polymer causes not only extension of the domain along the chain direction but also the rotation of the chain axis which is brought about by the shear stress between adjacent domains that possess different molecular orientations.

The strain at failure decreased significantly with the addition of GNP. The M5/epoxy composites were the most brittle, with the strain to failure dropping from 4.5 % to 0.9 % (decreased by 81 %) as weight fraction goes up from neat resin to 8 wt.%. The M25/epoxy composites were less brittle, but still the strain at failure still declined by 64 % for 8 wt.% samples. This embrittlement is typical when rigid fillers are added to a polymer matrix, and has been observed by other researchers [19-20].

Composite analytical theories are derived using the volume fraction of reinforcement rather than weight fraction. Thus in order to compare the experimental data for the Young's moduli with the theoretical data predicted by the Halpin-Tsai model, the experimental loadings were transformed into weight loading taking the densities as:. ρ_{epoxy} = 1.17 g/cm^3, $\rho_{hardener}$ = 1 g/cm^3 and ρ_{GNP} = 2.2 g/cm^3. The converted data is given in Table 5.2.

The tensile modulus was calculated from the initial linear portion of the stress–strain curve (up to 1.5 % strain) and is given in Figure 5.5. The highest loading studied experimentally was 8 wt.% (4.3 vol.%), as the increase in the viscosity of the system at any higher loading meant that the composite was un-processable. Overall, the Young's modulus of composites increased linearly with adding of GNP filler, and the highest increase was 45 % with inclusion of 8 wt.% GNP. The results are much lower than expected given the high modulus and strength of GNP, which may be due to the filler aggregations in composites; reducing GNP's enhance efficiency. The results are similar tot those reported in the literature [21].

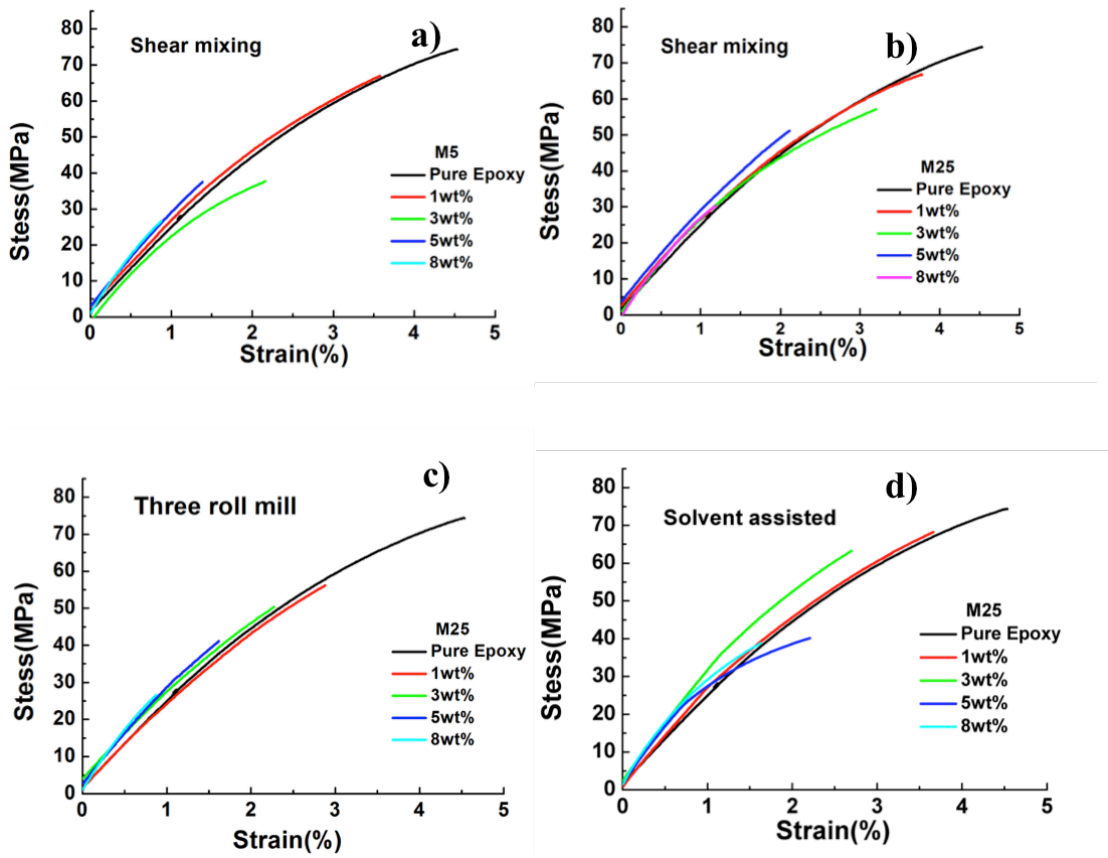

Figure 5.4 Typical stress-strain curves from: (a) epoxy/M5 composites produced by shear mixing, (b) epoxy/M25 composites produced by shear mixing, (c) epoxy/M25 composites produced by three-roll mill mixing, and (d) epoxy/M25 composites produced by solvent-assisted mixing.

Taking a closer analysis, the solvent-assisted mixed samples gave the best enhancement of Young's modulus up to 5 wt.%, which is correlated to the relatively uniform dispersion of M25 achieved by use of the solvent. When it comes to higher

filler concentrations, aggregation is unavoidable for different GNPs and fabricating methods, therefore 8 wt.% samples have similar tensile moduli.

It is interesting to find that there is no difference between M5 and M25 GNP fillers. These have different aspect ratio which is expected to have an influence on the mechanical properties according to literature [22]. One explanation would be that M25 has greater aggregation than M5 in the matrix due to the fact that the larger M25 platelets are more flexible/less stiff than the smaller M5. Furthermore under shear stress, it is easier for the high aspect ratio GNPs to bend/buckle or roll up, reducing the dimension and the resistance to dispersion flow (Figure 4.13f). While the smaller M5 fillers are more rigid and since they require more energy to bend or roll-up.

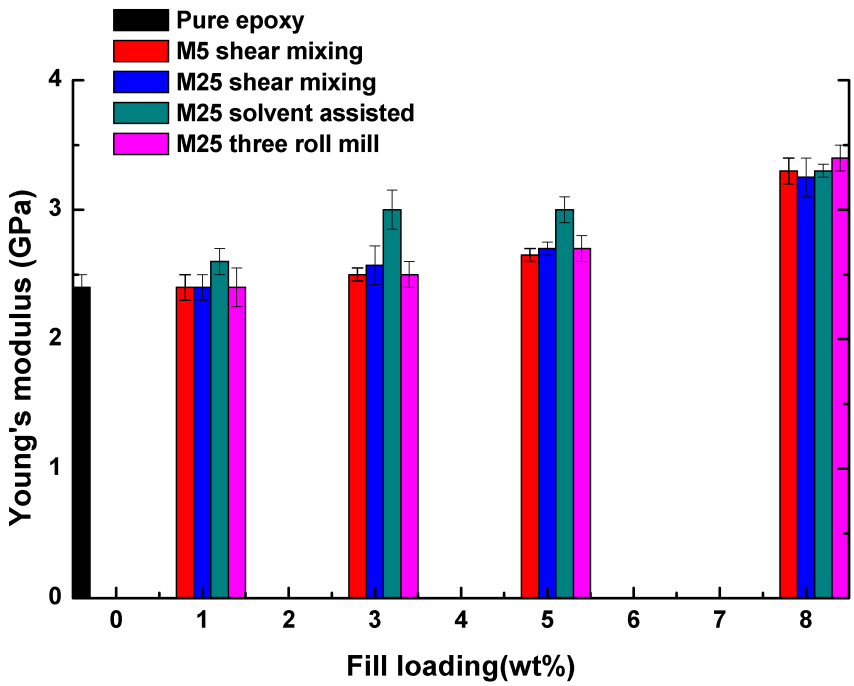

Figure 5.5 Young's modulus as a function of filler loading for M5 and M25 epoxy composites prepared by various methods.

The improvement of Young's modulus is not as high as one would expect given the high tensile modulus of GNP (1000 GPa). On average, GNP is a round-shape platelet with an average diameter of 5-25 μm and thickness of <10 nm, which gives aspect ratios of 500-2500. However, the real aspect ratio in the epoxy matrix is much smaller, as shown in Figure 4.12 f, the GNP does not maintain its separated platelet structure but forms aggregates that can be as large as 200-300 nm as a result of their large surface area and van der Waals forces between GNP flakes during the

fabrication of the composites. This phenomenon has also been observed by Kalaitzidou *et al.* in a PP matrix [13]. Their morphological examination of the GNP-15/PP nano-composites found that the graphite platelets aggregate at all loading for their 15 micron diameter GNP whereas a 1 μm diameter GNP was better dispersed. They stressed that the reinforcement's dispersion, the presence or absence of aggregation and the degree of alignment all strongly effect the degree of reinforcement.

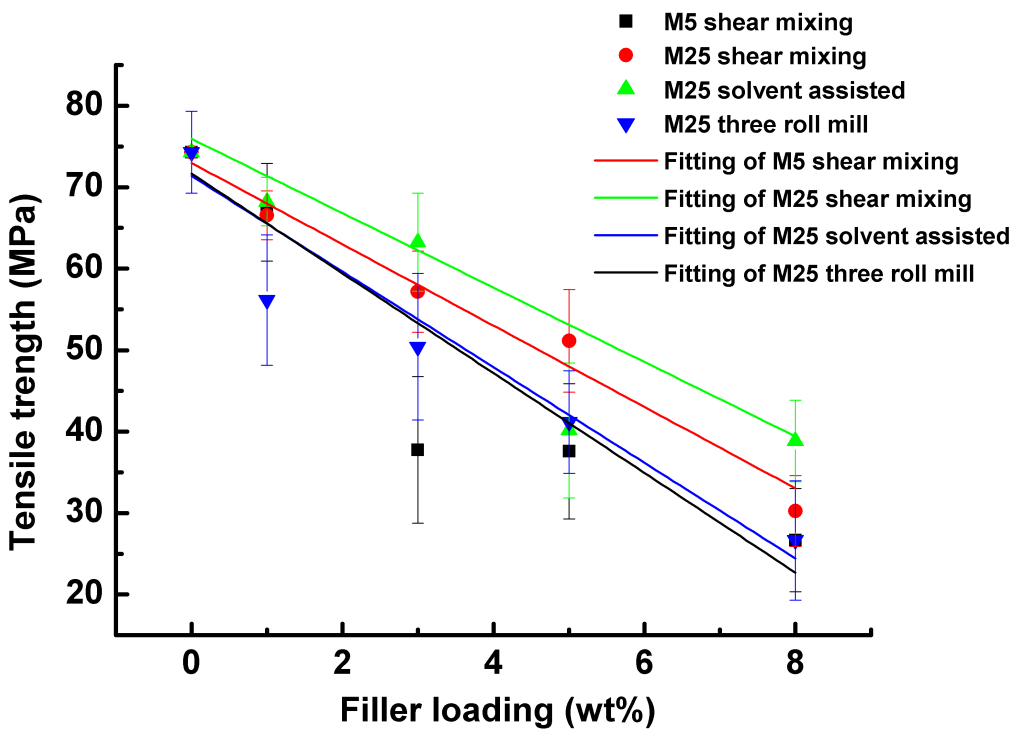

Figure 5.6 Tensile strength as a function of filler loading for M5 and M25 epoxy composites prepared by various methods.

Figure 5.6 reveals that although there is a good reinforcement of tensile modulus, the tensile strength of all the composites reduced with increasing loading of GNP. Overall, the solvent-assisted mixed specimens have the lowest decrease compared with those fabricated by shear mixing and three-roll mill mixing. However, although the decrease in the strength of the solvent-assisted mixed samples was the lowest reduction of tensile strength at 8 wt.%, it still decreased by 44 %.

The significant decrease in the tensile strength can be attributed to the poor interfacial adhesion between the reinforcement (GNP) and the epoxy matrix and severe aggregation of the GNPs. Strong interfacial interaction plays a crucial role an

achieving high strength of the polymer composites [23-24]. However, the clean smooth surface of GNP makes it rather difficult to get a good interfacial adhesion with the matrix, which is confirmed by the SEM images (Figure 4.12 and Figure 4.13) taken of the tensile fracture surface. Hence, load transfer from the polymer to the GNP is not sufficient to reach the tensile strength of the nanoplatelets under loading. Thus, the GNP aggregates effectively act as voids and may serve as stress-concentration points. SEM of the fracture surfaces in the previous chapter found cracks along the GNP/epoxy interface, pull-out of GNP, and cavities around the aggregate indicate an early interfacial debonding.

Table 5.2 Summary of composite mechanical properties.

Filler Type	**Filler loading (wt.%)**	**Young's modulus, *E* (GPa)**	**Tensile strength, σ_t (MPa)**	**Strain at Failure strain, ε_t (%)**
M5 shear mixing	0	2.4 ± 0.1	74.3 ± 5.0	4.5 ± 0.2
	1 (0.52)[a]	2.4 ± 0.2	66.9 ± 6.0	3.6 ± 0.2
	3 (1.57)	2.5 ± 0.1	37.7 ± 9.0	2.2 ± 0.3
	5 (2.64)	2.7 ± 0.1	37.6 ± 8.3	1.4 ± 0.3
	8 (4.29)	3.3 ± 0.2	26.6 ± 6.3	0.9 ± 0.3
M25 shear mixing	0	2.3 ± 0.1	74.3 ± 5.1	4.5 ± 0.2
	1 (0.52)	2.4 ± 0.2	66.6 ± 3.2	3.8 ± 0.3
	3 (1.57)	2.8 ± 0.3	57.2 ± 5.0	3.2 ± 0.3
	5 (2.64)	2.7 ± 0.1	51.2 ± 6.3	2.1 ± 0.4
	8 (4.29)	3.3 ± 0.3	30.2 ± 5.3	1.2 ± 0.4
M25 solvent-assisted	0	2.4 ± 0.1	74.3 ± 5.0	4.5 ± 0.2
	1 (0.52)	2.6 ± 0.2	68.2 ± 3.0	3.7 ± 0.2
	3 (1.57)	3.0 ± 03	63.3 ± 6.2	2.7 ± 0.3
	5 (2.64)	3.0 ± 0.2	40.2 ± 8.3	2.2 ± 0.3
	8 (4.29)	3.3 ± 0.1	38.8 ± 5.2	1.6 ± 0.4
M25 three-roll mill	0	2.4 ± 0.2	74.3 ± 5.0	4.5 ± 0.2
	1 (0.52)	2.4 ± 0.3	56.2 ± 9.9	2.9 ± 0.3
	3 (1.57)	2.5 ± 0.2	50.3 ± 9.0	2.3 ± 0.4
	5 (2.64)	2.7 ± 0.2	41.2 ± 7.3	1.6 ± 0.4
	8 (4.29)	3.4 ± 0.2	26.6 ± 7.3	0.9 ± 0.4

a : volume percentage

The drop in tensile strength of graphene platelets/epoxy composites has also been observed by other researchers [11-12, 25-26] who argued that the decrease was due to similar reasons of debonding of particles, voids in the sample and fracture initiation in some of the aggregates.

5.5 Theoretical Models *vs* Experimental Data

Due to the similarity of data from three-roll mill and solvent-assisted mixing, only shear mixing data has been fitted and is discussed. Figure 5.7 showed the experimental data of M5 and M25 epoxy composites produced by shear mixing fitted by the Halpin-Tsai theoretical model.

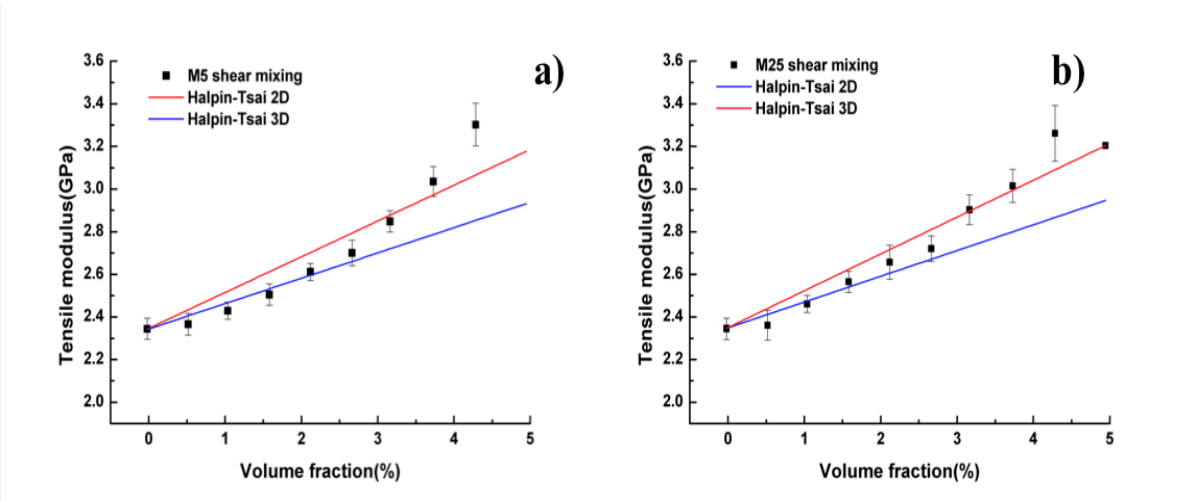

Figure 5.7 Tensile Modulus of M5 and M25 epoxy composites: Comparison of Halpin-Tsai theoretical models with experimental data.

In the Halpin-Tsai model, the aspect ratio and volume fraction of the filler, as well as the tensile moduli of the matrix and filler are used to predict the tensile modulus of composite materials [21]. For unidirectional, discontinuous filler composites, the Halpin-Tsai model predicts the composite tensile modulus using both moduli in the longitudinal direction, E_L, and the transverse, E_T, direction using eqns. (5.1) and (5.2) shown below:

$$E_C = \frac{3}{8}E_L + \frac{5}{8}E_T \qquad \text{2D Randomly oriented filler} \qquad (5.1)$$

$$E_C = \frac{1}{5}E_L + \frac{4}{5}E_T \qquad \text{3D Randomly oriented filler} \qquad (5.2)$$

Equations (5.1) and (5.2) are used for the two-dimensional (2D) random orientation of fillers and the three-dimensional (3D) random orientation of fillers respectively. E_C is the composite tensile modulus [27-28].

E_L is the longitudinal composite tensile modulus, E_T is the transverse composite tensile modulus, which are given by following equation (5.3) and (5.4):

$$\frac{E_L}{E_M} = \frac{1 + \xi\eta_L V_f}{1 - \eta_L V_f} \qquad (5.3)$$

$$\frac{E_L}{E_M} = \frac{1 + 2\eta_L V_f}{1 - \eta_L V_f} \qquad (5.4)$$

Where E_M is the tensile modulus of the matrix, *L/d* is the filler aspect ratio, V_f is the volume fraction of filler, and ξ is the filler shape factor [28-30]. For platelets, the filler shape factor, ξ, is equal to 2/3(L/d) [21].

The parameters η_L and η_T are given in eqs. (5.5) and (5.6) shown below:

$$\eta_L = \frac{\frac{E_f}{E_M} - 1}{\frac{E_f}{E_M} + \xi} \qquad (5.5)$$

$$\eta_T = \frac{\frac{E_f}{E_M} - 1}{\frac{E_f}{E_M} + 2} \qquad (5.6)$$

where E_f is the tensile modulus of the filler.

E_M, the tensile modulus of the epoxy matrix was measured experimentally to be 2.35 GPa regardless of the processing condition used. Figure 5.7 shows the experimental tensile modulus results as data points for the GNP/epoxy composites. In order to model epoxy/GNP system, assumptions need to be made about the properties of the GNPs.

Firstly, the GNP modulus is required. It is reported that graphene sheets have a modulus value of ~1000 GPa in the plane of the sheet [31], which could not be used directly in the equation cause GNP consists of multiple sheets stacked on each other.

The weak van der Waals's force between layers is likely to fail before graphitic carbon–carbon bonding within the sheets fails. Therefore, when tensile loads from the polymer matrix are transferred to the GNP particles, further exfoliation of the particle are expected, which will reduce the reinforcement effects dramatically. Hence, for the Halpin–Tsai model, the tensile modulus of GNP was equal to the modulus of exfoliation in the graphite c-axis (through-the-plane) of 36.5 GPa [32].very low

Figure 5.7 shows the results for the GNP/epoxy composites with E_f= 36.5 GPa and ξ_{M5} = 476.19, ξ_{M25} = 2380.95 (length = 5000 nm and 25000 nm for M5 and M25 respectively, and thickness = 7 nm).

The 3D Halpin-Tsai model fits the experimental data of M5 composites well at loading under 3.2 vol.% (6 wt.%). At high loadings, the Haplin-Tsai predicts values lower than the experimental data. As fillers loading increase, severe aggregation is likely to occur which pins the polymer segmental movement and increases Young's modulus, though compromising tensile strength to a large extent. This phenomenon is also observed by Liang *et al.* [23] in a graphene oxide and poly(vinyl alcohol) system, but no explanation has been given. The data of M25 composite modulus lies between the Halpin-Tsai predictions for random 2D and 3D orientations. However it is better fitted with the 3D orientation, which is consistent with the polarized Raman spectra results presented in chapter 4. In prior work, Kalaitzidou *et al.* [13]and King *et al. [21]* used the Halpin-Tsai model with ξ is equal to 0.667 (*L/d*) to successfully model the tensile modulus of GNP/polypropylene composites that were produced by extrusion and then injection moulded. These results show that the matrix and the fabricating methods have great impacts on filler dispersion.

5.6 Summary

In this chapter, DMTA, Raman and tensile testing have been carried out to characterize the mechanical properties. It is found that the efficiency of stress transfer from matrix to GNP is poor, which may be due to poor adhesion of the fillers to the epoxy matrix and easy slippage between internal graphene nanoplatelets layers. DMTA showed that T_g decreased in most cases, which is attributed to a reduction of crosslinking density. The addition of the GNPs increased the Young's modulus but the tensile strength and elongation at failure were significantly reduced. Solvent-assisted mixed sample had the largest increment of elastic modulus with lowest drops

regarding to elongation at break and tensile strength. The experimental data could be fitted reasonably by the Halpin-Tsai model, taking the modulus of the GNPs at 36.5 GPa and assuming a 3D dispersion. The latter assumption is supported by the Raman spectroscopy in the previous chapter.

References

1. Raju, A. P. A.; Lewis, A.; Derby, B.; Young, R. J.; Kinloch, I. A.; Zan, R.; Novoselov, K. S., Wide-Area Strain Sensors based upon Graphene-Polymer Composite Coatings Probed by Raman Spectroscopy. *Advanced Functional Materials* **2014,** *24* (19), 2865-2874.
2. Gupta, A. K.; Russin, T. J.; Gutierrez, H. R.; Eklund, P. C., Probing graphene edges via Raman scattering. *ACS Nano* **2009,** *3* (1), 45-52.
3. Casiraghi, C.; Hartschuh, A.; Qian, H.; Piscanec, S.; Georgi, C.; Fasoli, A.; Novoselov, K. S.; Basko, D. M.; Ferrari, A. C., Raman Spectroscopy of Graphene Edges. *Nano Letters* **2009,** *9* (4), 1433-1441.
4. Cong, C.; Yu, T.; Wang, H., Raman Study on the G Mode of Graphene for Determination of Edge Orientation. *ACS Nano* **2010,** *4* (6), 3175-3180.
5. Lee, J.-U.; Seck, N. M.; Yoon, D.; Choi, S.-M.; Son, Y.-W.; Cheong, H., Polarization dependence of double resonant Raman scattering band in bilayer graphene. *Carbon* **2014,** *72*, 257-263.
6. Liang, Q.; Yao, X.; Wang, W.; Liu, Y.; Wong, C. P., A Three-Dimensional Vertically Aligned Functionalized Multilayer Graphene Architecture: An Approach for Graphene-Based Thermal Interfacial Materials. *ACS Nano* **2011,** *5* (3), 2392-2401.
7. Li, Z.; Young, R. J.; Kinloch, I. A., Interfacial Stress Transfer in Graphene Oxide Nano-composites. *ACS Applied Materials & Interfaces* **2013,** *5* (2), 456-463.
8. Prolongo, S. G.; Burón, M.; Gude, M. R.; Chaos-Morán, R.; Campo, M.; Ureña, A., Effects of dispersion techniques of carbon nanofibers on the thermo-physical properties of epoxy nano-composites. *Composites Science and Technology* **2008,** *68* (13), 2722-2730.
9. Luo, Y.; Zhao, Y.; Cai, J.; Duan, Y.; Du, S., Effect of amino-functionalization on the interfacial adhesion of multi-walled carbon nanotubes/epoxy nano-composites. *Materials & Design* **2012,** *33*, 405-412.
10. Liu, G.; Zhang, H.; Zhang, D. J.; Zhang, H.; Zhang, Z.; An, X. F.; Yi, X. S., On depression of glass transition temperature of epoxy nano-composites. *Journal of Materials Science* **2012,** *47* (19), 6891-6895.
11. Wang, F.; Drzal, L.; Qin, Y.; Huang, Z., Mechanical properties and thermal conductivity of graphene nanoplatelet/epoxy composites. *Journal of Materials Science* **2015,** *50* (3), 1082-1093.
12. Zaman, I.; Manshoor, B.; Khalid, A.; Meng, Q.; Araby, S., Interface modification of clay and graphene platelets reinforced epoxy nano-composites: a comparative study. *Journal of Materials Science* **2014,** *49* (17), 5856-5865.

13. Kalaitzidou, K.; Fukushima, H.; Miyagawa, H.; Drzal, L. T., Flexural and tensile moduli of polypropylene nano-composites and comparison of experimental data to Halpin-Tsai and Tandon-Weng models. *Polymer Engineering & Science* **2007,** *47* (11), 1796-1803.
14. Her, S. C.; Yeh, S. W., Influence of Multi-Walled Carbon Nanotubes on the Mechanical Properties of Nano-composites. *Advanced Materials Research* **2010,** *139-141*, 9-12.
15. Ci, L.; Bai, J., The reinforcement role of carbon nanotubes in epoxy composites with different matrix stiffness. *Composites Science and Technology* **2006,** *66* (3–4), 599-603.
16. Jyotishkumar, P.; Abraham, E.; George, S. M.; Elias, E.; Pionteck, J.; Moldenaers, P.; Thomas, S., Preparation and properties of MWCNTs/poly (acrylonitrile-styrene-butadiene)/epoxy hybrid composites. *Journal of Applied Polymer Science* **2013,** *127* (4), 3093-3103.
17. de la Vega, A.; Kinloch, I. A.; Young, R. J.; Bauhofer, W.; Schulte, K., Simultaneous global and local strain sensing in SWCNT-epoxy composites by Raman and impedance spectroscopy. *Composites Science and Technology* **2011,** *71* (2), 160-166.
18. Northolt, M. G.; Baltussen, J. J. M.; Schaffers-Korff, B., Yielding and hysteresis of polymer fibres. *Polymer* **1995,** *36* (18), 3485-3492.
19. Yasmin, A.; Luo, J.-J.; Daniel, I. M., Processing of expanded graphite reinforced polymer nano-composites. *Composites Science and Technology* **2006,** *66* (9), 1182-1189.
20. Yasmin, A.; Abot, J. L.; Daniel, I. M., Processing of clay/epoxy nano-composites by shear mixing. *Scripta Materialia* **2003,** *49* (1), 81-86.
21. King, J. A.; Klimek, D. R.; Miskioglu, I.; Odegard, G. M., Mechanical properties of graphene nanoplatelet/epoxy composites. *Journal of Applied Polymer Science* **2013,** *128* (6), 4217-4223.
22. Wang, F.; Lawrence, T. D.; Qin, Y.; Huang, Z. X.; Mechanical properties and thermal conductivity of graphene nanoplatelet-epoxy composites, **2015**, Volume 50, Issue 3, pp 1082-1093.
23. Liang, J.; Huang, Y.; Zhang, L.; Wang, Y.; Ma, Y.; Guo, T.; Chen, Y., Molecular-Level Dispersion of Graphene into Poly(vinyl alcohol) and Effective Reinforcement of their Nano-composites. *Advanced Functional Materials* **2009,** *19* (14), 2297-2302.
24. Kim, H.; Miura, Y.; Macosko, C. W., Graphene/Polyurethane Nano-composites for Improved Gas Barrier and Electrical Conductivity. *Chemistry of Materials* **2010,** *22* (11), 3441-3450.
25. Zaman, I.; Phan, T. T.; Kuan, H.-C.; Meng, Q.; Bao La, L. T.; Luong, L.; Youssf, O.; Ma, J., Epoxy/graphene platelets nano-composites with two levels of interface strength. *Polymer* **2011,** *52* (7), 1603-1611.
26. King, J. A.; Klimek, D. R.; Miskioglu, I.; Odegard, G. M., Mechanical properties of graphene nanoplatelet/epoxy composites. *Journal of Composite Materials* **2014,** *49* (6), 659-668.
27. Mallick, P. K.; *Composites Engineering Handbook*. CRC Press: New York, **1997**.
28. Agarwal, B. D.; Broutman, L. J.; Chandrashekhara, K.; Analysis and Performance of Fiber Composites, **2006**, ISBN: 978-0-471-26891-8.

29. Halpin, J. C., Stiffness and Expansion Estimates for Oriented Short Fiber Composites. *Journal of Composite Materials* **1969,** *3* (4), 732-734.
30. Affdl, J. C. H.; Kardos, J. L., The Halpin-Tsai equations: A review. *Polymer Engineering & Science* **1976,** *16* (5), 344-352.
31. XG Sciences Inc. GNP® Brand Graphene Nanoplatelets Product Information, 3101 Grand Oak Drive, Lansing, MI 48911, **2010**.
32. Marsh, H.; Rodriguez-Reinoso, F., *Sciences of carbon materials.* Universidad de Alicante: Spain, **2001**, ISBN 8479085444.

CHAPTER 6 THERMAL AND ELECTRICAL PROPERTIES OF GNP COMPOSITES

6.1 Introduction

The incorporation of thermally and electrically conductive GNPs into an insulating matrix can be used to impart conductivity to a composite for applications such as anti-static coatings in fuel lines, strain sensors and thermal coatings. The electrical conductivity of a composite is predicted to increase by many orders of magnitude once the filler loading has reached the percolation threshold, whereas the thermal conductivity should increase following the rule of mixtures at low loadings. This chapter will mainly focus on the thermal and electrical performance changes brought by addition of GNP. Modelling will be applied to better understand the improvements

6.2 Thermal Conductivity of M5 and M25/epoxy Composites

The poor ability of polymers to conduct heat can limit their potential applications. Heat transfer involves the transport of energy from a hot region to a colder region by energy carriers. In solids these carrier particles are phonons or electrons. Phonons, are quantized modes of vibration occurring in a rigid crystal lattice and are the primary mechanism of heat conduction in most polymers since the free movement of electrons is not possible [1]. The Debye equation is usually used to calculate theoretically the thermal conductivity (λ) of polymers

$$\lambda = \frac{C_p v l}{3} \tag{6.1}$$

where C_p is the specific heat capacity per unit volume; v is the average phonon velocity and l is the phonon mean free path.

For amorphous polymers, l is an extremely small constant (i.e. a few angstroms) due to the phonons scattering from numerous defects, resulting in a very low thermal conductivity with values of ~ 0.2 W $m^{-1}K^{-1}$ for polymethylmethacrylate (PMMA) or polystyrene (PS) [2]. l increases with the degree of crystallinity in a polymer, thus highly crystalline polymers, such as

high-density polyethylene (HDPE) have conductivities as high as 0.5 W $m^{-1}K^{-1}$ [3]. These values, though, are still too low for most applications.

The main solution used to improve the thermal conductivity of a polymer is to blend into the matrix highly conductive fillers such as graphite, carbon black, ceramic beads or metal particles [4-7], all of which are well-known traditional fillers. Carbon-based fillers, like graphite, carbon black and carbon fibre, appear to be the most promising choice as they provide a combination of extremely high thermal conductivity, low price and lightweight. Among them, carbon nanotubes particularly show very promising enhancement of both the thermal and electrical conductivity. However, their relatively expensive production price and high viscosity during process caused by the nanotubes' entangled '*bird's nest*' structure limit the potential of nanotubes as reinforcements in polymers [8]. Thus recently, research has focused on graphene related materials to balance the price, processing and conductivity improvements.

Herein, GNP has been incorporated into an epoxy matrix to improve the thermal conductivity of the polymer. The thermal conductivity of the platelets are 3000 W $m^{-1}K^{-1}$ and 6 W $m^{-1}K^{-1}$ in-plane and out-of-plane respectively. M5 and M25/epoxy composites were prepared by three different methods as discussed in Chapter 3. The thermal conductivities were measured by steady-state method and data were plotted in Figure 6.1.

Both the M5 and M25 composite samples had an almost linear increase with filler loading independent of composite preparation method. The biggest improvement has been achieved by the solvent-assisted mixed M25/epoxy sample at 8 wt.% loading, with thermal conductivity enhanced from 0.20 W $m^{-1}K^{-1}$ (neat epoxy) to 0.76 W $m^{-1}K^{-1}$. This ~300 % improvement is less than expected considering the GNP's high thermal conductivity, as discussed in the next section. The relatively poor improvement seen experimentally is mainly attributed to the poor thermal coupling of the GNP with the polymer matrix leading to a high interfacial thermal resistance, also known as the Kapitza resistance [9], and high interfacial phonon scattering.

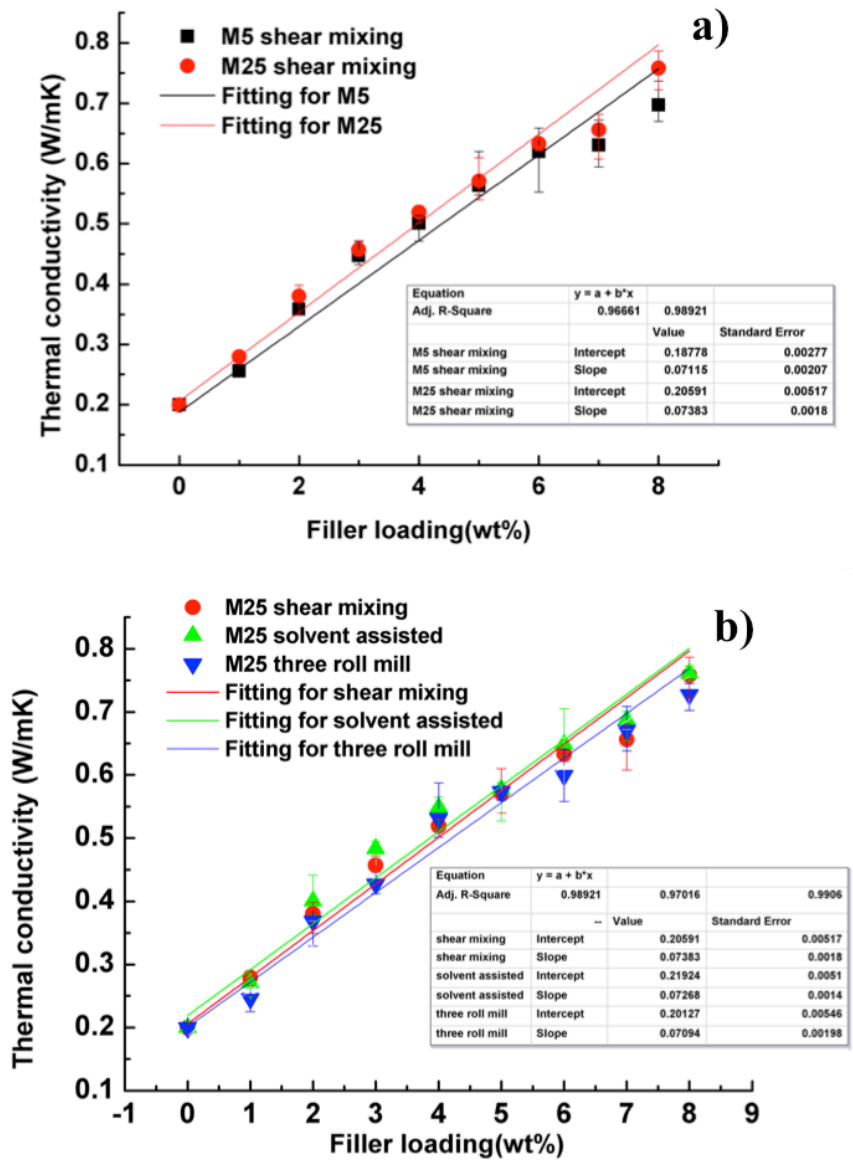

Figure 6.1 (a) M5 and M25/epoxy shear mixed composite conductivity as a function of GNP loadings and (b) thermal conductivity of M25/epoxy composites prepared by three different methods against GNP loadings.

No obvious percolation curve was observed for thermal conductivity. In the case of electrical conductivity, the aggregates formed by the GNP fillers alone contribute to the overall conductivity and there is no matrix contribution. Therefore, there is a sudden jump in electrical conductivity when the GNPs loading is high enough to connected with each other. However, thermal conductivity is a predominantly by phonons in the matrix. The large mismatch in thermal conductivity of the GNP and matrix results in large interfacial thermal resistance, leading to the lack of a percolation curve in thermal conductivity [10].

Taking a close look at the thermal conductivity curves in Figure 6.1a, it is can be seen that M25/epoxy composites have higher thermal conductivity than that of the M5/epoxy over the whole GNP loadings. This difference is due mainly to the difference in the lateral dimensional of the two GNPs. GNPs with smaller dimensions tend to form more interface with the matrix, where the majority of phonon scattering occurs [11]. Thus, the higher interface densities of M5/epoxy composites cause higher phonon scattering, leading to larger interfacial thermal resistance, which decreases its thermal transfer enhancement effect. Furthermore, a lower aspect ratio has a low efficiency in forming a thermally conductive network. However given the aspect ratio of M25 is five times of that of M5, the small difference of thermal conductivity is not as large as expected, which will be discussed later.

Comparison of thermal conductivities of samples by different fabrication methods is shown in Figure 6.1b. At low loadings (≤ 2 wt.%), no significant difference can be observed for samples fabricated by the three methods. This can be explained that no severe aggregates have formed at that GNP fraction for all three methods. As loading goes up, the solvent-assisted mixed samples exhibit better thermal conductivity over the other two methods, which can be explained by its relatively more uniform distribution of GNP assisted by organic solvent (as shown by SEM images). Unlike electrical conductivity, in which moderate aggregations can be of benefit connecting a network more effectively.

6.3 Modelling of Thermal Conductivity

Modelling is a widely used method to have a proper theoretical understanding of composite thermal conductivity behaviour as a function of various factors, which is highly desired to develop high-thermal-performance GNP composites. Xie *et al.* [12] modeled the GNP as infinitely long fibres to study the effective thermal conductivity of composites. It was shown that the predictions overestimated the thermal-conductivity enhancements due to not taking the interfacial thermal resistance into account.

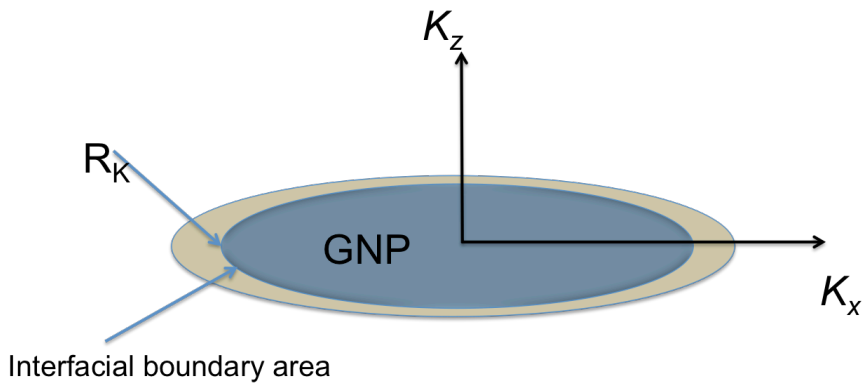

Figure 6.2 Diagram of a GNP coated with a very thin interfacial boundary layer.

Lin *et al. [13]* proposed a more rigorous model for the effective thermal conductivity of GNP composites based on a Maxwell-Garnett effective-medium-approximation (EMA) theory [14]. They took an isotropic two-phase composite as a system consisting of randomly oriented ellipsoidal GNPs embedded in a matrix, where the GNP can be considered as an oblate spheroid with very large aspect ratio, as illustrated in Figure 6.2. Furthermore, the GNP is coated with thin layer of epoxy, as a core-shell structure with an interfacial thermal resistance R_K, as illustrated in Figure 6.2. This model demonstrates the strong influences of the aspect ratio and the orientation of the GNP, and indicates that the interfacial thermal resistance plays a key role in determining the overall thermal transport of GNP composites. Since the thermal conductivity of GNP is much larger than that of the polymer matrix ($K_{X(Z)} \gg K_m$), a simplified equation for thermal conductivity was proposed:

$$\frac{K^*}{K_m} = \frac{1+2f\left(\frac{K_x}{K_m\left(\frac{2R_K K_x}{L}+1\right)}\right)/3}{1-f/3} \tag{6.2}$$

where K*, K_m and K_x are the thermal conductivities of the composite, epoxy matrix and GNP along the x direction respectively. *l* is the lateral dimension of GNP (5 μm and 25 μm are used for M5 and M25 respectively). *f* is GNP volume fraction in composite. R_K is interfacial thermal resistance between GNP and matrix. Chu *et al*. [15] extracted the R_K as 4.6×10^{-8} m^2 K/W for GNP/epoxy composites, which is in general agreement with values reported in the literature for composites with carbon nanofillers, covering the range of $3 \sim 9 \times 10^{-8}$ m^2 K/W [16].

Due to the significant difference of the in-plane and out-of-plane thermal conductivity of GNP and its random orientation in matrix, it was assumed that both thermal conductivities contribute equally to the composites. Therefore, K_x = 6 W $m^{-1}K^{-1}$and 3000 W $m^{-1}K^{-1}$are used separately to get two K^* values, and final K^* is averaged of these two K^*.

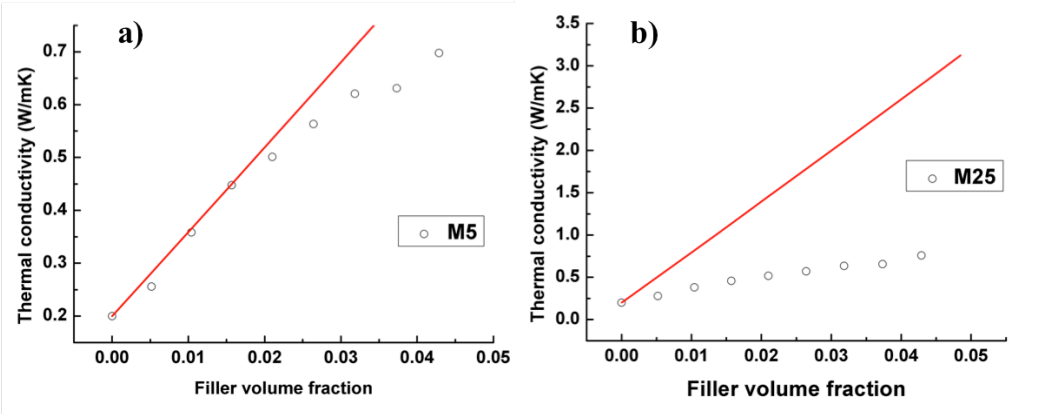

Figure 6.3 Comparison of experimental and modelling data of M5 (a) and M25 (b)/epoxy composites made by shear mixing. The dot and solid line represent experimental and modelling calculated data respectively.

Figure 6.3a shows that at low loadings (≤ 3vol%), the modeling fits well with t he experimental data of M5/epoxy composites. As volume fraction increases, experimental data is lower than the prediction from modeling, which can be explained that higher loading leads to aggregations and reduce the enhancement of thermal conductivity by GNP. Overall, the model fits very well with experimental data.

For M25/epoxy composites, modeling data has a big deviation from experimental data (Figure 6.3b). According to the model and equation, the aspect ratio plays an important role in improving the thermal conductivity. Therefore, the prediction for M25 added composites are much larger than that of M5 composites. In the real case, however although M25/epoxy composites show superior thermal conductivity performance over the M5/epoxy composites, the difference is not that big (as shown Figure 6.1). The main reason is GNP aggregation largely reduces the lateral dimension difference between M5 and M25, which has been discussed in mechanical property section and is the reason the model failed.

From the discussion above, the main route to modify thermal conductivity of polymer is to improve the interaction of filler and matrix to reduce the thermal resistance by functionalization of filler, which has been confirmed by other researchers' work [17-18].

6.4 Impedance Testing of GNP/epoxy Composites

Impedance spectroscopy was used to study the insulator-conductor transition of epoxy resin via the addition of highly conductive GNP fillers. It is also a powerful characterization tool and can be used to construct an equivalent circuit for the conductive composite, and thus provides information about the formation of a conductive network. In this section, the ability of M5 to form a conductive network was compared with M25 in terms of electrical percolation and maximum conductivity. Comparison of effects of different fabrication methods on the electrical conductivity of composites was also carried out.

Percolation threshold theory is derived by considering the volume fraction of GNPs that are connected. As such, the critical loading is traditionally referred to as the critical volume fraction. However, since the density of GNP and other nanoparticles can only be approximated, weight percentage has widely been used in the literature [19-21]. Likewise in the following discussion, weight percentage will be used instead of volume fraction.

Figure 6.4 shows the conductivity (σ) as a function of frequency for the M5 and M25 composites at various GNP loadings. There are some common features for both GNP composites. At low loadings ($\leq$ 1 wt.%), both impedance data are quite random, which means the electrical conductivity is out of the measurement range of the impedance equipment (100 mΩ ~100 MΩ) and samples can be viewed as insulators. As loading increases to 1 wt.% for M25/epoxy and 2 wt.% for M5/epoxy, there is a small plateau appearing, where σ is independent of frequency ($\leq$ 10 Hz), meaning a conductive network has formed, but there exist only a few conductive pathways, so the contribution of the capacitive junctions between the aggregates becomes important. As the frequency increases, the current passing through each capacitor increases, resulting in the enhanced conductivity of the composites. The specific conductivity increases more than two orders and three orders of magnitude for M25 and M5 composites

respectively after forming of the plateau. The plateau is followed by a steep increase of specific conductivity with the frequency of the applied AC, which occurs when capacitive elements dominate the resistive elements in the sample [22]. Further loading increase leads to an extended plateau, indicating the sample is more close to a pure resistor, as the conductivity is determined mainly by the numerous paths of the percolating GNP aggregates rather than the capacitors when the loading is significantly higher than the percolation threshold. Therefore, the specific conductivity will not change with frequency until the contribution of the capacitors becomes dominant again at very high frequencies.

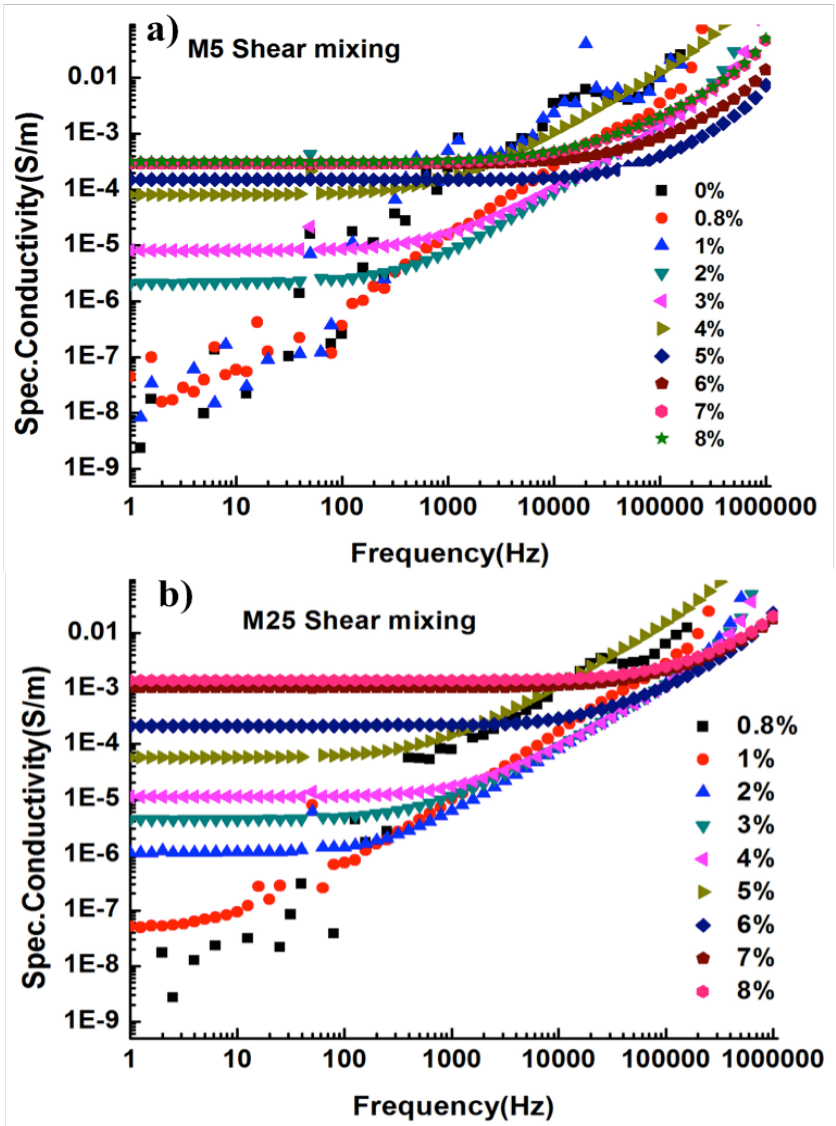

Figure 6.4 Specific conductivity as a function of frequency for M5 (a) and M25 (b)epoxy composites at various GNP loadings.

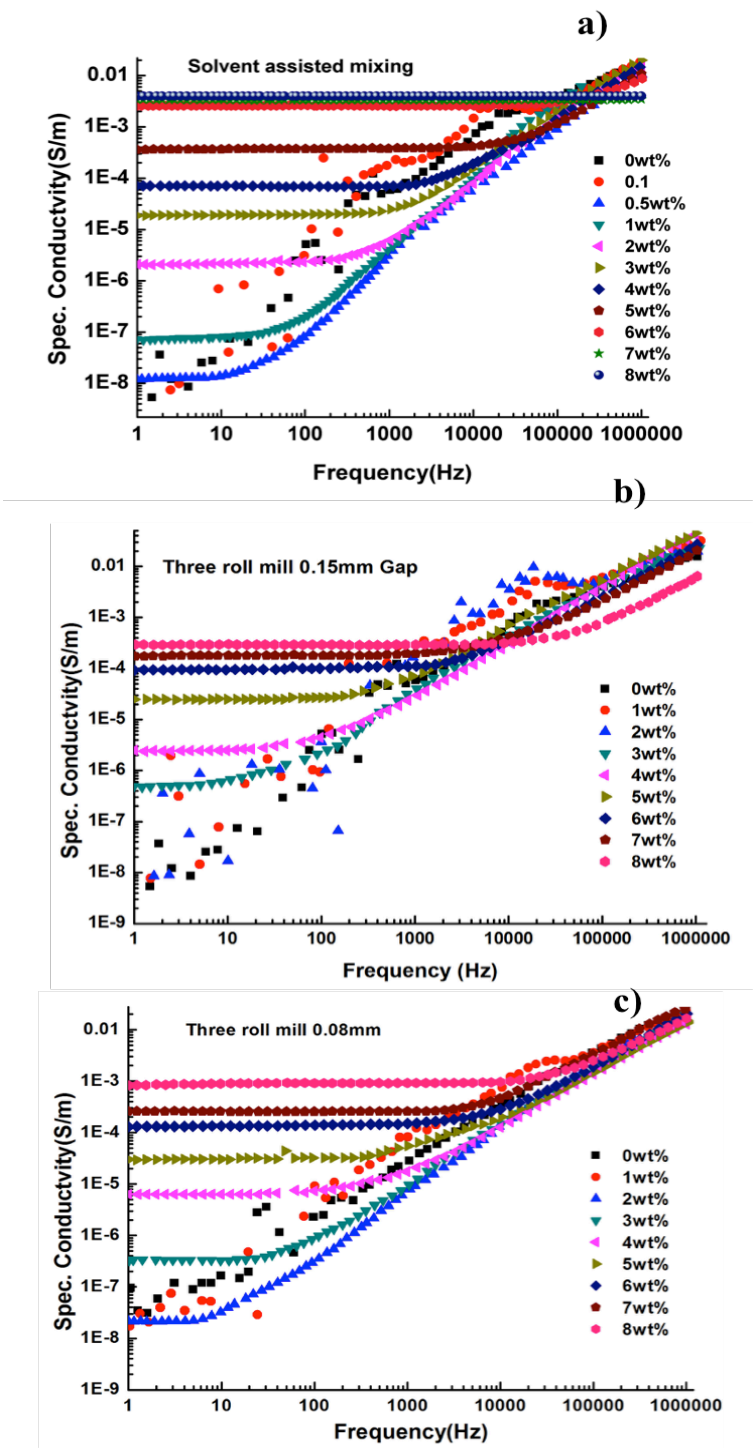

Figure 6.5 Specific conductivity as a function of frequency for M25 epoxy composites fabricated by solvent-assisted mixing (a) and three-roll mill mixing at 0.15mm roller gap (b) and 0.08mm roller gap (c).

Figure 6.5 shows specific conductivity results for M25 epoxy composites fabricated by solvent-assisted mixing and three-roll mill mixing at various loadings. Similar trends have been observed for both methods. For solvent-

assisted samples, σ begins to show independence of frequency at low frequency at the loading of 0.5 wt.%. For 8 wt.% loading, σ keeps constant over the whole frequency range, which means it is a pure resistor. For three-roll mill mixed composites, small plateaus of σ against frequency appear at 3 wt.% and 2 wt.% for roller gaps of 0.15 mm and 0.08 mm respectively. However, there is no pure resistor behaviour for all of the three-roll mill samples, indicating the electrical enhancement efficiency is not as high as that of the solvent-assisted samples.

6.5 Electrical Percolation Threshold

Percolation threshold is a mathematical concept related to percolation theory, which is the formation of long-range connectivity in random systems. When applied to the electrical properties of composites, it refers to a critical volume fraction of filler which will induce a dramatic increase in the electrical conductivity when incorporated into to an insulator matrix. At low filler loading, conductive fillers cause hardly any change in a composite's electrical properties because the density of the filler aggregates is too low to connect with each other. With the increase of filler weight fraction, the distribution of these aggregates start to form a connected network, allowing the electrons to travel within the composites. Above this percolation threshold, any further addition of filler only causes moderate increases in conductivity. As such, the loading range where this dramatic change occurs is important and is a common subject of investigation [23]. A low percolation threshold would be an added advantage for a polymer composite, as a high GNP content would not only increase processing difficulty, but also tend to embrittle the composites [24].

The equation derived from percolation theory that describes the connectivity of the aggregates, the dimensionality of the formed percolated network, and the conductivity of the composites above the percolation threshold is [25-26]:

$$\sigma(p) = \sigma_c(p - p_c)^t; \qquad for\ p > p_c \qquad (6.3)$$

where σ is the specific conductivity of the composite, σ_c is the proportionality constant, p_c is the critical loading (wt. %), and p is the filler loading (wt. %). In

theory, the universal constant, t, is < 2 for random 2D networks and > 2 for 3D random networks [27].

The specific conductivity, σ, plotted as a function of filler loading is shown in Figure 6.6 for both the M5 and M25 composites. It should be noted that in this work, the DC equivalent of a sample's conductivity is taken when the frequency is 5Hz. This practice of determining dc equivalence at low frequency points has been applied previously in the literature [19, 21].

A step-like transition due to the percolation phenomenon can be observed when the GNP contents change from 1 wt.% to 2 wt.% for both the M5 and M25/epoxy composites. The electrical conductivity of the composite is enhanced by two orders of magnitude in the step-like region. When the GNP loading is lower than 1 wt.%, the composites behave as insulators. With increase of GNP loading, a conductive network forms and the electrical conductivity displays a sharp increase in bulk conductivity.

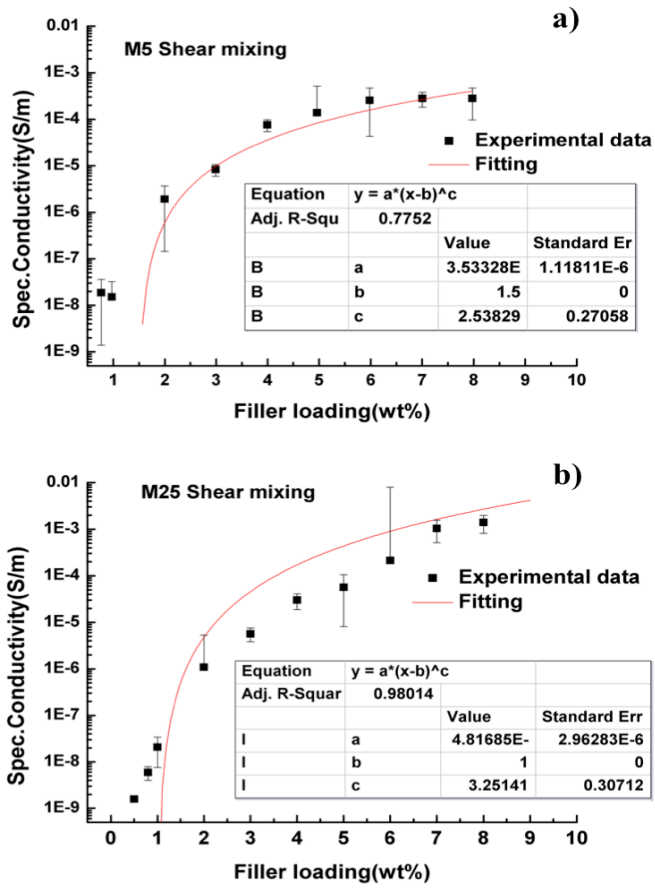

Figure 6.6 Semi log plot of the specific conductivity, σ, as a function of the filler loadings for M5 (a) and M25 (b) composites produced by shear mixing. The inset shows the fitting data used to fit percolation theory to the experimental results.

The value of p_c was first estimated from Figure 6.4 and Figure 6.5 by examining the loading at which the small plateau independent of frequency first appeared. Next, the experimental σ values were plotted against p-p_c on a log-log scale and fitted using the power law fit in the regression option in Origin™ software. After that, the values of R^2 were recorded to determine the degree of fits. (The closer R^2 is to 1, the better the fit.) The process was then repeated by varying p_c until the error in the fit was minimized. As shown in Figure 6.6, there is a steep increase in the conductivity of a few orders of magnitude in the percolation region for both GNP composites. In the case of M5/epoxy samples, the data fitting yielded p_c = 1.5 wt.% with R^2 = 0.77, which is poor due to data scattering. A p_c of 1 wt.% was obtained for the M25/epoxy samples with R^2 = 0.98.

M25 has a relatively lower electrical percolation threshold, due mainly to its high aspect ratio, which enables it to form a connected GNP network more efficiently than M5 [28]. The p_c values reported in the literature vary greatly due to the effects of processing, GNP type and matrix properties on the formation of the percolated network. Li *et al* and Zheng *et al* reported 0.5 vol% (equal to ~1 wt.%) and 1 wt.% percolation threshold for GNP epoxy composites [29-30], which are consistent with our results. It is suggested that the high aspect ratio and good distribution of GNP in the matrix contribute to the low percolation threshold of the composite [30]. However, much higher percolation threshold have also been observed with values varying from 4 wt.% ~ 14 wt.% [28, 31-32]. Green *et al.* argued that their high 6 wt.% percolation threshold was partially attributed to the different characters of the polymers, which result in different GNP dispersion qualities [28]. The main reasons laid in the aspect ratio of the nanoparticle, as affected by the sonication process. According to their experience, and based on common literature knowledge, tip sonication results in lower aspect ratios compared with bath sonication, hence, raising the percolation threshold.

t was found to be 2.66 and 3.25 for M5 and M25 composites respectively, suggesting a 3-D random dispersion of GNP in the matrix, which is consistent with observation of SEM and optical microscopy results.

From the fitting results of Figure 6.7, p_c for M25 composites prepared by solvent-assisted mixing samples and three-roll mill mixed samples (with 0.15 mm and 0.08 mm roller gap) are 0.5 wt.%, 3 wt.% and 2 wt.% respectively.

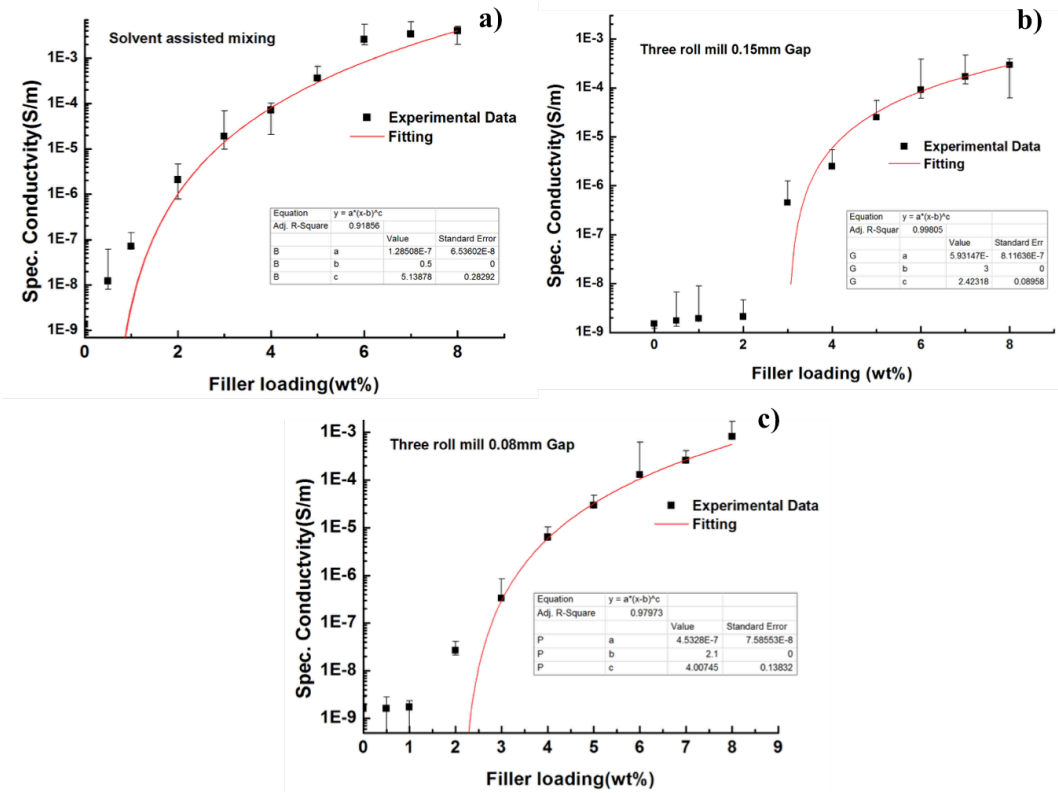

Figure 6.7 Semi log plot of the specific conductivity, σ, as a function of GNP loadings for the M25 composites produced by solvent-assisted mixing (a) and three-roll milling with 0.15 (b) and 0.08mm (c) roller gap. The inset shows the fitting data used.

Table 6.1 summaries the electrical percolation threshold, conductivity at the highest loading (8 wt.%) and conductivity exponent of the samples studied. The solvent-assisted mixed samples had the highest conductivity and the lowest percolation threshold compared to the composites produced by three-roll milling and shear mixing, which may be attributed to the relatively uniform distribution of GNP in the solvent-assisted samples. Although a perfectly uniform dispersion will increase the percolation threshold as the connecting efficiency between GNPs is low, too much aggregation can also increase the percolation threshold. Hence, the moderate degree of aggregation in the solvent-assisted mixed samples was a suitable compromise. This theory could also explain why samples of three-roll mill with 0.08mm roller gap had a lower percolation and better maximum

conductivity (at 8wt.%) than that with 0.15 mm roller gap, since smaller gap increases the degree of dispersion.

Table 6.1 Summary of electrical parameters of all samples.

Filler type	Preparation methods	Electrical percolation threshold (wt.%)	Conductivity at 8wt.% (S/m)	*t*
M5	Shear mixing	1.5	3.2×10^{-4}	2.66
M25	Shear mixing	1	1.4×10^{-3}	3.25
M25	Solvent-assisted mixing	0.5	4.0×10^{-3}	5.14
M25	Three-roll mill (0.08mm Gap)	2	8.2×10^{-4}	4.01
	Three-roll mill (0.15mm Gap)	3	2.9×10^{-4}	2.42

6.6 The Equivalent Circuit Model of Composites

Zhang *et al.* [20] developed a simple model equivalent circuit for MWCNTs in a PVA matrix. Due to the similarity of GNP and matrix type, this model was adapted for this project to study GNP/epoxy composites (Figure 6.8).

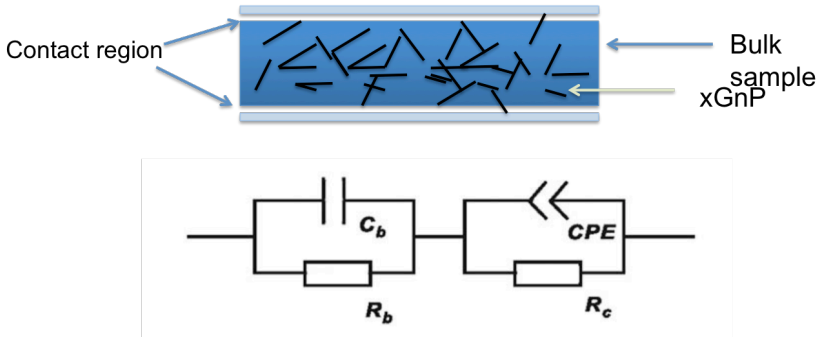

Figure 6.8 The model and equivalent circuit model used for the GNP/epoxy composites.

This equivalent circuit contains a serial arrangement of two units that represent the contribution from the bulk composite sample and the contact region of the interface between the silver paint and the sample. Each unit is depicted by a combination of two possible electrical current components, (i) a resistor (R) and a capacitor (C) or (ii) a resistor and a constant phase element (CPE) in parallel. The latter is the equivalent electrical circuit component used to model the behaviour of a double layer, that is an imperfect capacitor. In this project, the CPE is introduced to simulate and explain the electrical behaviour of the

GNP/epoxy composites. The explanation will fit experimental data so well that the deviations are due to the experimental noise and uncertainties [33-34].

Accordingly, the complex impedance of the equivalent network can be denoted as follows [20]:

$$Z = \frac{1}{i\omega C_b + \frac{1}{R_b}} + \frac{1}{i\omega C_c + \frac{1}{R_c}} \tag{6.5}$$

where *R* and *C* refer to the resistance and capacitance, respectively, in which the subscript b and c represent the bulk sample and the contact region, respectively.

The complex impedance of the equivalent circuit can be rewritten as follows upon introducing the CPE [20]:

$$Z = \frac{1}{i\omega C_b + \frac{1}{R_b}} + \frac{1}{(i\omega)^{\alpha} C_{rc} + \frac{1}{R_c}} \tag{6.6}$$

where C_{rc} is the ‘‘true’’ capacitance of the contact region. $\alpha = \varphi_{CPE} / 90°$, and the phase angle φ_{CPE} is frequency-independent, so that the CPE exponent α is a constant, independent of frequency. Since the phase angle is always less than 90°, α is less than 1.0 as well. When α is 1.0, the CPE becomes an ideal capacitor. One of the most plausible physical causes for needing to introduce the CPE is surface irregularity or interfacial roughness, and various models have been proposed to relate CPE behaviour to the fractal geometry of the sample [35-36].

In our case, due to the roughness of the abrasive paper and the soft surface of composites, it is not possible to obtain an absolutely flat surface. Accordingly, the rougher the surface of the sample is, the further the constant α deviates from 1. The values of α indicate how the contact region owing to the roughness of the surface deviates from a true capacitance. Value of the elements and α from Eq. (6.6) are listed in Table 6.2. Namely, the chaos and irregularity of the metal-semiconductor interface increase as the GNP content increases.

It should be noted that due to the superior electrical properties of M25/epoxy over M5/epoxy, only M25/epoxy composites have been made by three methods in this project. Due to the similarity of electrical behaviour of samples, only shear mixed will be discussed in detail during the following section.

Figure 6.9 shows Nyquist lines for several GNP/epoxy composites with different GNP contents. The round dots are experimental data and the solid curve is fitted equivalent circuit. The values of the corresponding parameters are listed in Table 6.2.

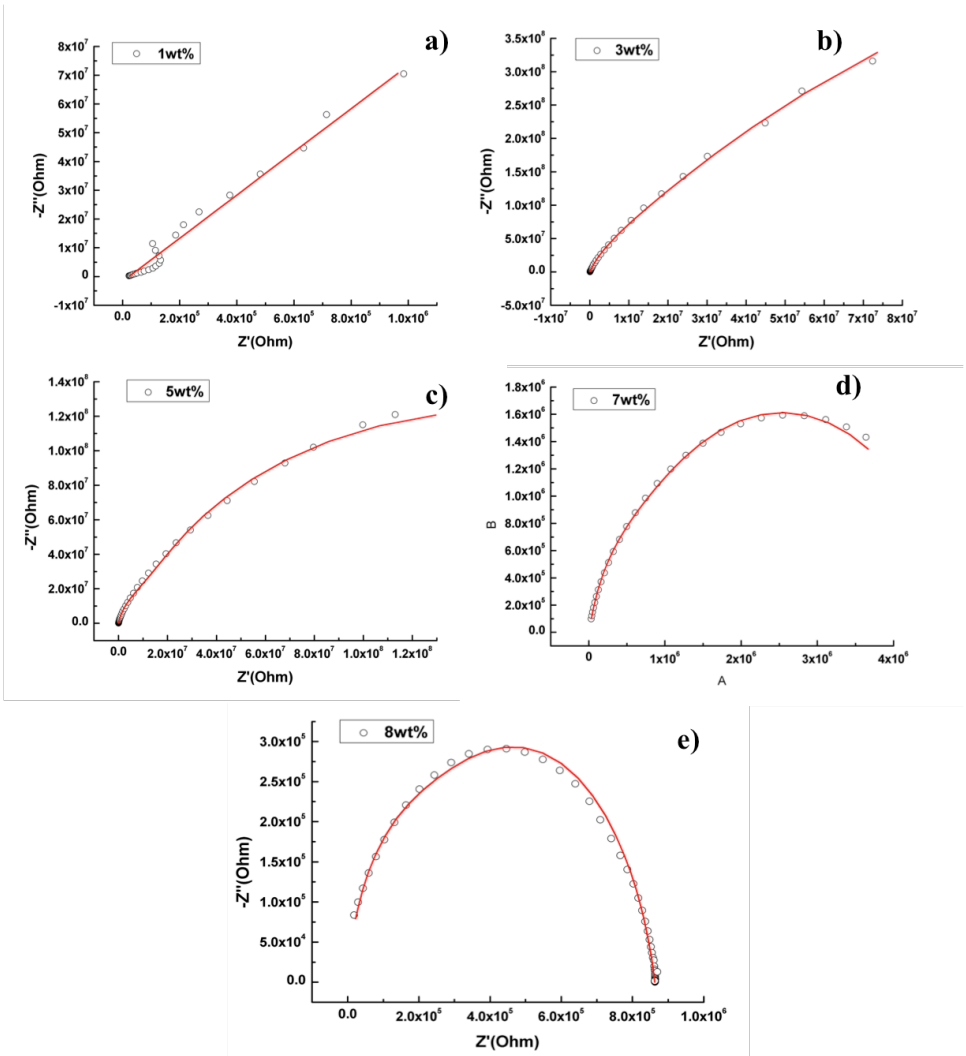

Figure 6.9 The Nyquist plots and the simulated equivalent circuit for the GNP/epoxy composites prepared by shear mixing with different GNP contents. (a) 1 wt.%; (b) 3 wt.%; (c) 5 wt.%; (d) 7wt.% and (e) 8 wt.%. The points are the experiment data, and the solid line is from the equivalent circuit.

From low to high GNP loadings, the Nyquist line changes from a straight line (Figure 6.9a) to a quarter circle (Figure 6.9c) to a semi-circle (Figure 6.9e). The radius of the Nyquist line represents resistance, thus the resistance decreases with increasing loading, which is consistent with the results in Table 6.2. The R_b

of the composite dropped two orders of magnitude as GNP content increased from 1 wt.% to 2 wt.%, indicating the formation of percolated networks.

Table 6.2 The corresponding parameters from the simulation results.

Preparation methods	Weight fraction (wt.%)	R_b (Ω)	C_b (pF)	R_c (Ω)	C_{rc} (pF)	α
High shear mixing	0	N/A	N/A	N/A	N/A	N/A
	1	2.2×10^{12}	1E-8	9.4×10^{12}	0.77	0.99
	2	3.5×10^{10}	0.03	6.6×10^{9}	3.40	0.89
	3	2.3×10^{9}	0.98	3.9×10^{7}	12.8	0.86
	4	3.3×10^{8}	0.67	4.4×10^{7}	11.3	0.85
	5	7.9×10^{6}	0.59	3.0×10^{8}	10.1	0.87
	6	3.5×10^{5}	0.79	3.8×10^{6}	34.5	0.79
	7	3.9×10^{5}	0.69	4.7×10^{6}	73.2	0.76
	8	1.7×10^{5}	0.39	6.9×10^{5}	49.3	0.83
Solvent-assisted mixing	1	3.3×10^{10}	0.34	3.7×10^{9}	1.21	0.93
	2	3.7×10^{9}	0.56	6.9×10^{8}	5.67	0.86
	3	4.9×10^{9}	0.67	1.2×10^{7}	15.3	0.85
	4	4.6×10^{8}	0.68	5.4×10^{7}	12.3	0.79
	5	7.9×10^{7}	0.63	9.0×10^{7}	25.5	0.81
	6	3.6×10^{5}	1.23	5.3×10^{6}	38.5	0.75
	7	4.9×10^{5}	1.24	4.3×10^{5}	45.2	0.73
	8	5.7×10^{5}	3.21	4.5×10^{5}	80.4	0.80
Three-roll mill (0.08 Gap)	1	N/A	N/A	N/A	N/A	N/A
	2	4.7×10^{10}	0.56	6.9×10^{9}	6.4	0.87
	3	5.3×10^{9}	0.89	4.2×10^{8}	11.8	0.86
	4	7.5×10^{8}	0.88	8.4×10^{7}	25.3	0.83
	5	9.7×10^{8}	0.96	3.3×10^{8}	26.1	0.79
	6	3.5×10^{7}	1.26	5.6×10^{8}	40.5	0.81
	7	3.9×10^{6}	2.43	7.3×10^{7}	69.2	0.74
	8	1.7×10^{6}	3.22	9.4×10^{7}	89.3	0.73

For solvent-assisted mixed and three-roll mill samples, this dramatic drop in R_b occurs at around 1 wt.% and 2 wt.% respectively, which is in good agreement with values obtained by percolation calculation.

The contact region resistance is lower than the bulk resistance, R_b, at low loadings. The GNP fillers are ridge and can stick out of the surface into the silver paint, bridging the composite-electrode interface. Thus, taking into account the numerous GNP flakes dispersed in the matrix, the total number of such points can be reasonably large even at low GNP contents. Consequently, R_C for the GNP/epoxy composite below the critical percolation threshold is lower than that of the bulk sample. As GNP contents go up, a connective network will be formed in the bulk of the composites, which leads to a dramatic drop of resistance, while R_b is still controlled by contact points and reduced linearly, sometimes even increases due to the random distribution of contact points between contact area. Therefore, above the percolation threshold loading, R_C becomes smaller than R_b. α also reduces with increasing GNP content, which means the surface of composites between contact region is becoming rougher as more and more rigid GNPs are incorporated into the matrix, namely it is further away from a perfect capacitor.

6.7 Summary

The thermal conductivity of M5 and M25/epoxy composites made by three methods was been measured as a function of GNP loading. The conductivity was found to increase linearly with GNP loading. A model based on EMA theory has been applied to study the effects of GNP aspect ratio and interfacial thermal resistance on the overall thermal transport within the GNP composites. It was found that the aspect ratio does not have expected effect on the thermal conductivity due to aggregation.

The electrical conductivity of the composites was investigated using impedance analysis and the percolation thresholds calculated. The M25 composites had a lower electrical percolation threshold (1 wt.%) than the M5 composites, (1.5 wt.%). For the three different preparation methods, the solvent-assisted mixed samples had the lowest percolation of 0.5 wt.% due to its relatively uniform GNP dispersion. Samples produced by three-roll milling using

roll gaps of 0.08 mm and 0.15 mm had higher electrical percolation threshold of around 2 wt.% and 3 wt.% respectively.

The Nyqusit lines gave information on the network structure of composites and an equivalent circuit was proposed accordingly. The circuit composed of resistor and capacitor in parallel connected in series to a resistor and constant phase element in parallel. The modeling results fitted the experimental data well, showing R_b decreased dramatically around the percolation threshold.

References

1. King, J. A.; Klimek, D. R.; Miskioglu, I.; Odegard, G. M., Mechanical properties of graphene nanoplatelet/epoxy composites. *Journal of Applied Polymer Science* **2013,** *128* (6), 4217-4223.
2. Agari, Y.; Ueda, A.; Omura, Y.; Nagai, S., Thermal diffusivity and conductivity of PMMA/PC blends. *Polymer* **1997,** *38* (4), 801-807.
3. Hu, M.; Yu, D.; Wei, J., Thermal conductivity determination of small polymer samples by differential scanning calorimetry. *Polymer Testing* **2007,** *26* (3), 333-337.
4. *Handbook of carbon, graphite, diamond and fullerenes: properties. Processing and applications* . Noyes Publications: New Jersey, **1993**.
5. *Handbook of fillers: physical properties of fillers and filled materials.* ChemTec Publishing: Toronto, **2000**.
6. Kelly, B. T., *Physics of graphite.* Applied Science Publishers: UK, **1981**.
7. Wolff, S.; Wang, M. J., *Carbon black science & technology*. Marcel Dekker: New York, **1993**.
8. Sandler, J. K. W.; Pegel, S.; Cadek, M.; Gojny, F.; van Es, M.; Lohmar, J.; Blau, W. J.; Schulte, K.; Windle, A. H.; Shaffer, M. S. P., A comparative study of melt spun polyamide-12 fibres reinforced with carbon nanotubes and nanofibres. *Polymer* **2004,** *45* (6), 2001-2015.
9. Hu, L.; Desai, T.; Keblinski, P., Thermal transport in graphene-based nano-composite. *Journal of Applied Physics* **2011,** *110* (3), 033517.
10. Chandrasekaran, S.; Seidel, C.; Schulte, K., Preparation and characterization of graphite nano-platelet (GNP)/epoxy nano-composite: Mechanical, electrical and thermal properties. *European Polymer Journal* **2013,** *49* (12), 3878-3888.
11. Pop, E.; Varshney, V.; Roy, A. K., Thermal properties of graphene: Fundamentals and applications. *MRS Bulletin* **2012,** *37* (12), 1273-1281
12. Xie, S. H.; Liu, Y. Y.; Li, J. Y., Comparison of the effective conductivity between composites reinforced by graphene nanosheets and carbon nanotubes. *Applied Physics Letters* **2008,** *92* (24), 243121.
13. Cheng-Hui, W.; Wei-Yang, L.; Zhang-Yu, J.; Keh-Chyang, L.; Chuen-Horng, T., Direct synthesis of suspended single-walled carbon

nanotubes crossing plasma sharpened carbon nanofibre tips. *Nanotechnology* **2006,** *17* (1), 1.

14. Lu-Chang, Q., Electron diffraction from carbon nanotubes. *Reports on Progress in Physics* **2006,** *69* (10), 2761.
15. Chu, K.; Li, W. S.; Dong, H. F.; Tang, F. L., Modelling the thermal conductivity of graphene nanoplatelets reinforced composites. *Epl* **2012,** *100* (3).
16. Unnikrishnan, V. U.; Banerjee, D.; Reddy, J. N., Atomistic-mesoscale interfacial resistance based thermal analysis of carbon nanotube systems. *International Journal of Thermal Sciences* **2008,** *47* (12), 1602-1609.
17. Gulotty, R.; Castellino, M.; Jagdale, P.; Tagliaferro, A.; Balandin, A. A., Effects of functionalization on thermal properties of single-wall and multi-wall carbon nanotube-polymer nano-composites. *ACS Nano* **2013,** *7* (6), 5114-21.
18. Wang, M.; Galpaya, D.; Lai, Z. B.; Xu, Y.; Yan, C., Surface functionalization on the thermal conductivity of graphene–polymer nano-composites. *International Journal of Smart and Nano Materials* **2014,** *5* (2), 123-132.
19. Sandler, J. K. W.; Kirk, J. E.; Kinloch, I. A.; Shaffer, M. S. P.; Windle, A. H., Ultra-low electrical percolation threshold in carbon-nanotube-epoxy composites. *Polymer* **2003,** *44* (19), 5893-5899.
20. Zhang, J.; Mine, M.; Zhu, D.; Matsuo, M., Electrical and dielectric behaviours and their origins in the three-dimensional polyvinyl alcohol/MWCNT composites with low percolation threshold. *Carbon* **2009,** *47* (5), 1311-1320.
21. Martin, C. A.; Sandler, J. K. W.; Shaffer, M. S. P.; Schwarz, M. K.; Bauhofer, W.; Schulte, K.; Windle, A. H., Formation of percolating networks in multi-wall carbon-nanotube-epoxy composites. *Composites Science and Technology* **2004,** *64* (15), 2309-2316.
22. Gerhardt, R. A.; *Impedance Spectroscopy and Mobility Spectra. Encyclopedia of Condensed Matter Physics*. Elsevier: London, **2005,** 350-363.
23. Bauhofer, W.; Kovacs, J. Z., A review and analysis of electrical percolation in carbon nanotube polymer composites. *Composites Science and Technology* **2009,** *69* (10), 1486-1498.
24. Shaffer, M. S. P.; Sandler, K. W.; Carbon Nanotube/Nanofibre Polymer Composites, **2006**.
25. Kilbride, B. E.; Coleman, J. N.; Fraysse, J.; Fournet, P.; Cadek, M.; Drury, A.; Hutzler, S.; Roth, S.; Blau, W. J., Experimental observation of scaling laws for alternating current and direct current conductivity in polymer-carbon nanotube composite thin films. *Journal of Applied Physics* **2002,** *92* (7), 4024-4030.
26. Jurewicz, I.; Worajittiphon, P.; King, A. A.; Sellin, P. J.; Keddie, J. L.; Dalton, A. B., Locking carbon nanotubes in confined lattice geometries--a route to low percolation in conducting composites. *J Phys Chem B* **2011,** *115* (20), 6395-400.
27. Stauffer, D. A. A.; *Introduction to percolation theory*. Taylor and Francis: London, **1994**.

28. Green, M.; Marom, G.; Li, J.; Kim, J.-K., The Electrical Conductivity of Graphite Nanoplatelet Filled Conjugated Polyacrylonitrile. *Macromolecular Rapid Communications* **2008,** *29* (14), 1254-1258.
29. Li, J.; Sham, M. L.; Kim, J. K.; Marom, G., Morphology and properties of UV/ozone treated graphite nanoplatelet/epoxy nano-composites. *Composites Science and Technology* **2007,** *67* (2), 296-305.
30. Zheng, C.; Fan, Z.; Wei, T.; Luo, G., Temperature dependence of the conductivity behaviour of graphite nanoplatelet-filled epoxy resin composites. *Journal of Applied Polymer Science* **2009,** *113* (3), 1515-1519.
31. Chen, G. H.; Chen, X. F.; Wang, H. Q.; Wu, D. J., Dispersion of graphite nanosheets in polymer resins via masterbatch technique. *Journal of Applied Polymer Science* **2007,** *103* (6), 3470-3475.
32. Du, X. S.; Xiao, M.; Meng, Y. Z.; Hay, A. S., Synthesis and properties of poly (4,4 '-oxybis (benzene)disulfide)/graphite nano-composites via in situ ring-opening polymerization of macrocyclic oligomers. *Polymer* **2004,** *45* (19), 6713-6718.
33. Grimnes, S.; Martinsen, O. G., Cole electrical impedance model--a critique and an alternative. *IEEE Trans Biomed Eng* **2005,** *52* (1), 132-5.
34. Macdonald JR; WR., K., *Impedance spectroscopy: emphasizing solid materials and systems*. John Wiley: New York, **1984**; Vol. Sect. 2.2.3.4.
35. Nyikos, L.; Pajkossy, T., Fractal dimension and fractional power frequency-dependent impedance of blocking electrodes. *Electrochimica Acta* **1985,** *30* (11), 1533-1540.
36. Sapoval, B., Fractal Electrodes and Constant Phase-Angle Response - Exact Examples and Counter Examples. *Solid State Ionics* **1987,** *23* (4), 253-259.

CHAPTER 7 WATER UPTAKE OF GNP/EPOXY COMPOSITES AND ITS EFFECTS ON MECHANICAL AND ELECTRICAL PROPERTIES

7.1 Introduction

One of the main disadvantages of using epoxy resin in applications is their tendency to absorb water when in humid environments, leading to swelling, plasticization and, in certain cases, degradation [1-4]. In this chapter, the water uptake of the unfilled epoxy and the composites reinforced with M25 made by shear mixing is investigated. (It was decided to focus on only the shear mixed samples due the similarity of filler dispersion and orientation in the composites prepared by three different methods,)

7.2 Water Uptake Measurements of Epoxy Composites

The results of the gravimetric studies for water uptake are presented in Figure 7.1. During the initial stages, the weight gain due to water uptake increased linearly with $\sqrt{t}$ for all of samples, which is consistent with Fickian diffusion. This linear region extends until $M_t / M_\infty < 0.6$, which has been reported by other researchers [1, 3, 5-7]. After that, water absorption becomes controlled by relaxation of water molecule in the matrix at long aging times, and it takes more than two months to be water saturated.

During the water diffusion process, the diffusion coefficient (D) is an important factor, which describes the mass of the substance that diffuses through a unit surface in a unit time at a concentration gradient of unity. D can be calculated by Fick's law as described in Chapter 2 (Equation 2.4) which is valid when the water percentage absorbed does not reach 60 % of saturation, and the values of D with maximum water absorbed (M_∞) at equilibrium are listed in Table 7.1.

$$D = \frac{\pi}{16}\left(\frac{L}{M_\infty}\right)^2\left(\frac{M_{t2}-M_{t1}}{\sqrt{t_2}-\sqrt{t_1}}\right)^2 \quad (2.4)$$

where t is absorbed time, M_t is the water absorption at time t, M_∞ is the equilibrium water absorption, L is the sample thickness, and D is the diffusion coefficient.

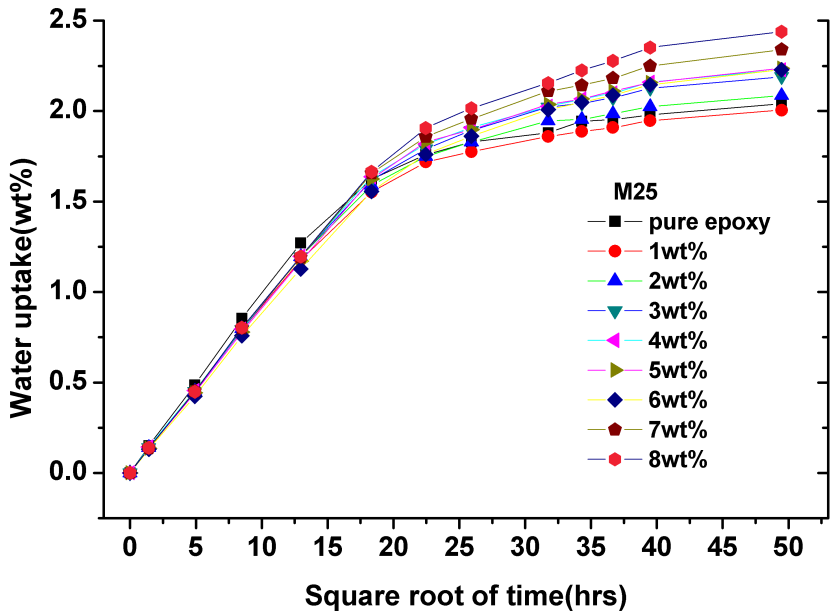

Figure 7.1 Water uptake of epoxy resin and nano-composites reinforced with M25 made by shear mixing. The lines are a guide for the eye.

Table 7.1 Parameters of water diffusion.

M25 loadings (wt.%)	M_∞ (wt.%)	D × 10^9 (cm^2/s)
0	2.04 ± 0.01	5.27 ± 0.47
1	2.01 ± 0.03	5.11 ± 0.24
2	2.09 ± 0.02	4.61 ± 0.45
3	2.19 ± 0.02	4.23 ± 0.25
4	2.23 ± 0.03	3.82 ± 0.39
5	2.24 ± 0.07	3.71 ± 0.42
6	2.23 ± 0.09	3.46 ± 0.37
7	2.34 ± 0.06	3.49 ± 0.39
8	2.44 ± 0.01	3.09 ± 0.13

M_∞: maximum water absorbed in saturation.

D : diffusion coefficient.

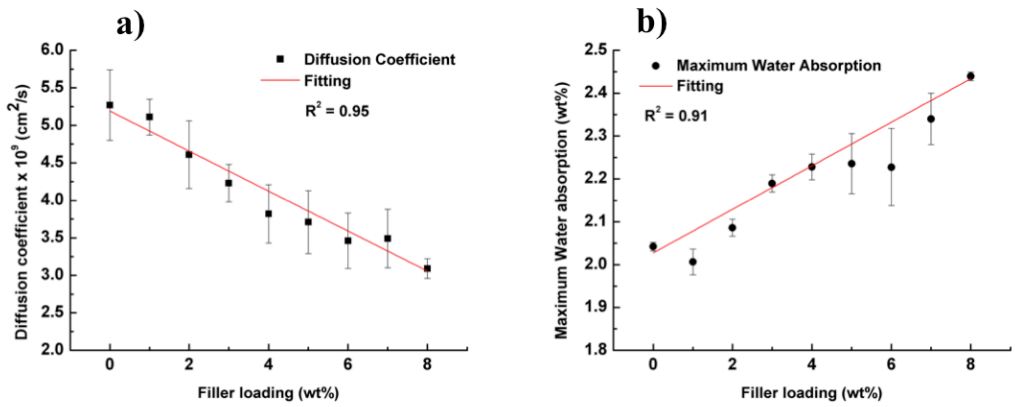

Figure 7.2 Diffusion coefficient (a) and maximum water absorption (b) as function of GNP loadings for M25 composites.

Figure 7.2 shows an interesting phenomenon, D decreases with GNP contents, while M_∞ increases. D and M_∞ are mainly controlled by the structure of composites that have a close relationship with filler loadings. Therefore, D and M_∞ are expected to change linearly with filler loadings and the results are fitted by linear fittings. A closer examination of the variation in D remains constant for low loadings, then followed by a bigger drop in the GNP loading range of 2 wt.% ~ 4 wt.%. This loading coincides with the electrical percolation threshold found earlier in the thesis. As the loading increases further above the percolation threshold, there is only a small decrease in D. This significant decrease of diffusion coefficient from pure epoxy resin to 8 wt.% composite could be attributed to high surface area of M25, which leads to significant barrier effects of GNP in epoxy matrix [8], forming tortuous paths and hindering the water progress and decreasing the diffusion rate. When a connected network has been formed, the hindering effect increases slightly. However, M_∞ goes shows opposite behaviour. Even though it is reported that the addition of a carbon nanofiller reduces the saturated water content in epoxy composites [8]. At 1 wt.% GNP content, M_∞ dropped slightly, which could be associated with the formation of strong interfaces between the epoxy matrix and the GNP and the hydrophobicity of carbon nano materials relative to the hydrophilic behaviour of epoxy resin [8]. As loading increases M_∞ also increases gradually. This can be explained by higher filler contents leading to aggregation, and the holes and cavity formed in and along aggregations (Figure 4.12 and Figure 4.13) lead to a

higher M_∞ [9-10]. Due to the high hydrophobicity of GNP, the platelet will not absorb water. Therefore, the maximum water absorbed is associated with the epoxy resin and the cracks and holes of GNP aggregations. For the pure epoxy 2.04 wt.% is the saturated water weight, which means 0.0204 wt.% is absorbed by each 1 wt.% of the epoxy matrix, which can be viewed as a constant. Thus, the water absorbed by the epoxy matrix and GNP aggregation can be calculated separately using equation 7.1 and 7.2, and values are listed in Table 7.2.

$$W_{epoxy} = \frac{(100-p)\times 0.0204}{M_\infty} \tag{7.1}$$

$$W_h = 100 - W_{epoxy} \tag{7.2}$$

where W_{epoxy} is wt.% of water absorbed by the epoxy matrix, p is GNP loading in wt.%, M_∞ is the equilibrium water absorption, and W_h is water weight percentage taken by holes and cracks.

Table 7.2 Water absorption of neat epoxy and M25 composites.

Filler loading (wt.%)	**Water absorbed by (wt.%)**	
	Epoxy	Holes and cracks
0	100	0
1	100	0
2	95.7	4.3
3	90.4	9.6
4	87.8	12.2
5	86.5	13.5
6	85.9	14.1
7	81.1	18.9
8	76.9	23.1

For 1 wt.% sample, the 99 wt.% epoxy can absorb 2.01% saturated water, which is the M_∞ of this sample, indicating holes and cracks did not take any water. Namely, there are almost no cracks or holes in composites with this low GNP content. With increase of GNP loading, the water taken by holes and cracks becomes higher, indicating more aggregates have formed, which is consistent with SEM observation.

7.3 Effects of Water Uptake on Thermal Conductivity of Composites

Two sets of samples with various M25 loadings were prepared by shear mixing to study the effects of water absorption on the thermal conductivity of composites. One sample set were saturated with water, following a long aging time, and another set were pristine, un-aged composite samples. The properties of the saturated samples were measured immediately after been taken out of water bath and the excess surface water being removed by absorbing paper. Then the saturated samples were placed in oven at 60 °C and held under vacuum for 10 days to dry it to its original weight. It was found that the absorbed water can be removed completely, which means that no chemically bound water has been formed during the long aging time period. Comparison of thermal conductivity of the two sets is plotted in Figure 7.3.

Figure 7.3 shows that the water-saturated samples had the highest thermal conductivity, which can be easily explained that water has higher thermal transfer capacity (with thermal conductivity of 0.6 W $m^{-1}K^{-1}$) than the epoxy resin, forming bridges between GNP fillers. This can also explain why higher loading composites after water-saturation display greater thermal conductivity increment because of higher M_∞. For the water desorbed samples, post-curing in water after long aging time and drying may be the reason that the samples have better thermal transfer performance over the unaged samples.

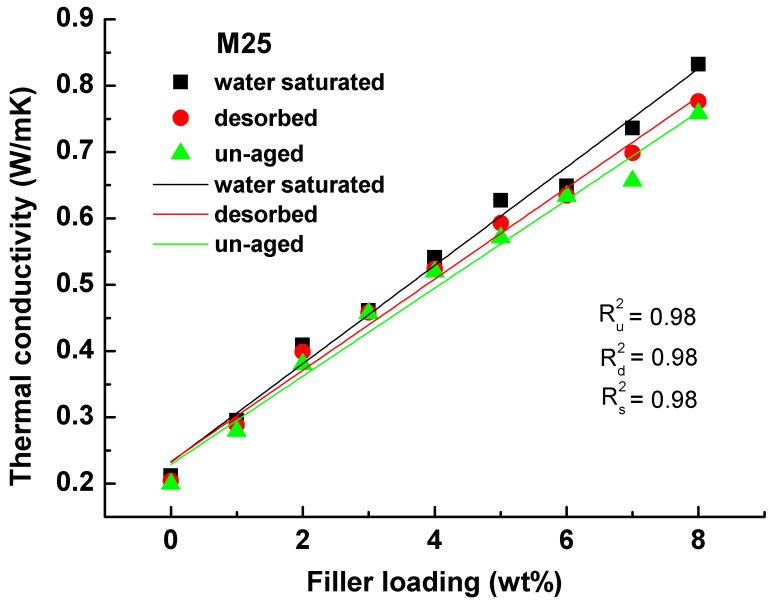

Figure 7.3 Thermal conductivity of composites as function of GNP loadings with fitting results.

7.4 Effects of Water Uptake on Thermal Mechanical Behaviour of Composites

The effects of water absorption on the dynamical mechanical properties of the composites made by shear mixing were studied by DMTA. Two sets of samples were tested. One set were water saturated, and the another was dried in an oven at 60 °C for 10 days for remove absorbed water, as confirmed by constant mass with time. The T_g was taken from the peak position of tan δ. The storage modulus and tan δ are plotted as function of temperature in Figure 7.4.

The storage moduli of both water-saturated and water-desorbed samples show almost a linear increase with addition of M25, which was observed in the previous DMTA tests reported in Chapter 5, and the increment of storage modulus (~ 40%) is similar with M25/epoxy composites made by shear mixing, suggesting effective loading transfer from matrix to GNPs was not changed by water absorption. For the T_g, the variation trends of saturated and desorbed samples are also quite like the previous shear mixing samples without water absorption. It undergoes a T_g drop at initial GNP addition stage, followed by an increase of T_g. The reason has been explained in Chapter 5.

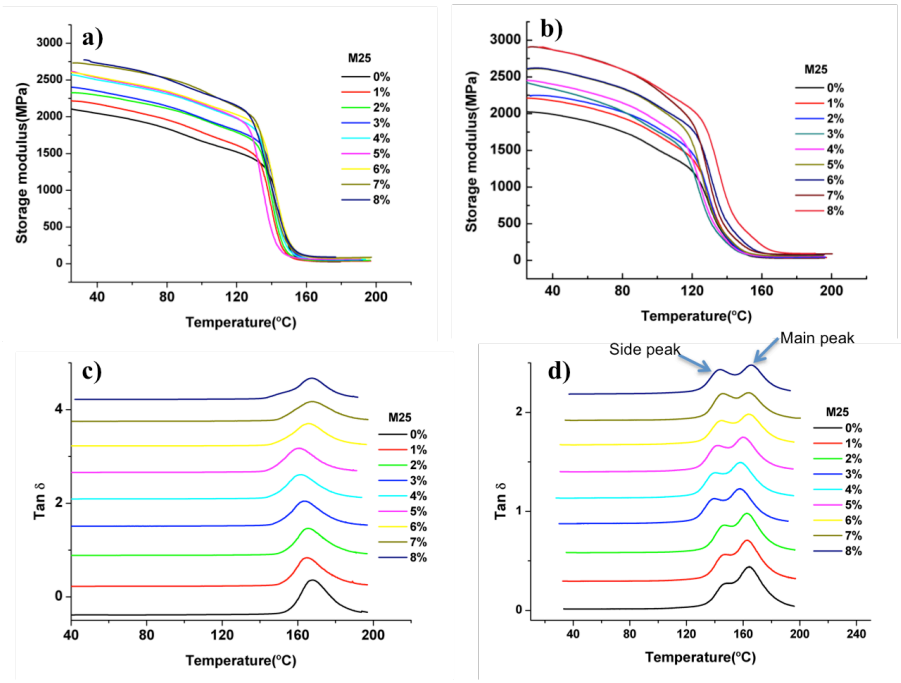

Figure 7.4 Storage modulus and loss factor of water desorbed (a, c) and water-saturated (b, d) samples versus temperature.

The interesting phenomenon for the water-saturated samples is the tan δ curve peak, which is split into two peaks, which has been observed by other researchers on epoxy systems filled with carbon and other nanofillers [1, 4, 8, 11]. The proposed explanation is that part of absorbed water is not forming a chemical link to the polymer matrix, inducing swelling effects of the composites to different extents in different areas, leading to two stage segmental movements at various temperatures. These changes are more marked in composites than in neat epoxy resin with evidence of increasing side peak heights and broadening distance between side peak and main peak. This is because the increasing content of water is absorbed for higher loading samples. The values of peak positions and peak heights are listed in Table 7.3, and are plotted with unaged samples in Figure 7.5.

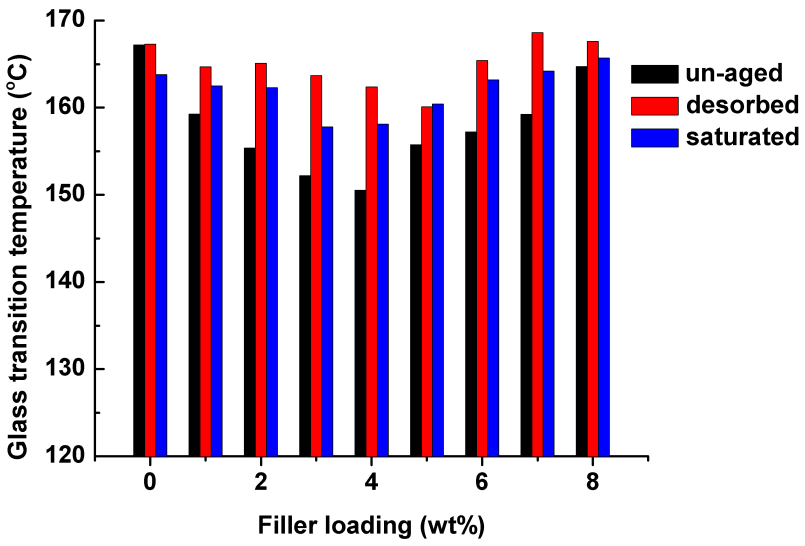

Figure 7.5 T_g of unaged, water saturated and water desorbed samples.

Table 7.3 DMTA parameters for water saturated and water desorbed neat epoxy and nano-composites.

	Water saturated samples			Water desorbed samples			Unaged samples	
Filler loading	T_g	Peak Height	Side Peak	Peak Height	T_g	Peak height	T_g	Peak height
0	163.8	0.44	147.9	0.27	167.3	0.76	167.2	0.77
1	162.5	0.43	145.1	0.27	164.7	0.63	159.3	0.69
2	162.3	0.41	145.9	0.29	165.1	0.59	155.4	0.91
3	157.8	0.37	139.4	0.27	163.7	0.55	152.2	0.78
4	158.1	0.37	139.4	0.27	162.4	0.54	150.5	0.82
5	160.4	0.36	142.6	0.28	160.1	0.53	155.7	0.72
6	163.2	0.33	144.9	0.26	165.4	0.49	157.2	0.69
7	164.2	0.3	145.8	0.29	168.6	0.44	159.2	0.75
8	165.7	0.31	143.7	0.26	167.6	0.47	164.7	0.69

When comparing the T_g values of water-saturated and water-desorbed samples, it is found that the T_g of water saturated samples drops around 2 ~ 4 °C. This is an expected behaviour and the phenomenon is known as plasticization due to interaction of the water molecules with polar groups in the matrix [2, 11]. In other words, the hydrogen bonds between the water molecules and the polar hydroxyl groups of the matrix network will disrupt inter-chain hydrogen bonding and the initial van der Waal bonds, resulting in the releasing of segmental motion, reducing the energy needed to move molecule chains. The molecular structure is thus altered, causing dimensional changes and reduction of T_g. While after drying T_g goes back to similar values as previously prepared samples in Chapter 5, or even higher than the unaged samples, which may be attributed to the extraction of sol fraction after being immersed in 50 °C water for more than two months.

7.5 Effects of Water Uptake on Electrical Conductivity of Composites

Water-saturated samples and vacuum-dried samples (60 °C, 5 days) were tested by impedance analysis. For the sake of clarity, only three comparative curves of specific conductivity versus frequency have been plotted in Figure 7.6, and the values for all samples are listed in Table 7.4.

It can be clearly seen that the specific conductivity is increased after removing the absorbed water. When the water was absorbed into the composites, it caused swelling of epoxy matrix, resulting in longer distance between conductive GNPs and larger resistance. Apart from that, the distilled water absorbed filled gaps and cracks inside and along the GNP aggregates is a near insulator, which further increases the resistance. However, in real life, the moisture absorbed by M25 composites would not be distilled water, but water containing various ions, which will benefit electrical conductivity. Therefore, the trends of electrical conductivity of composites in humid environment need to be further studied.

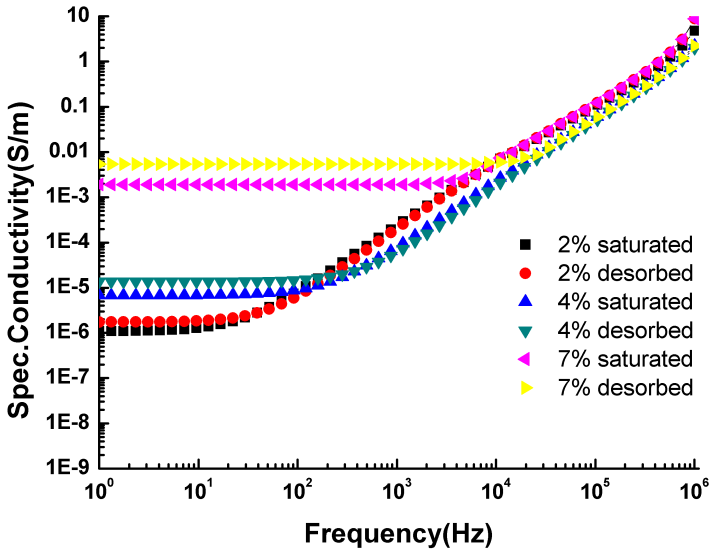

Figure 7.6 Specific conductivity of water-saturated and water-desorbed M25 composite samples.

Table 7.4 Specific conductivity of M25 composite samples.

M25 Filler loading (wt.%)	Specific Conductivity (S/m)	
	Water-saturated	Water-desorbed
0	N/A	N/A
1	2.31 E-8	5.40 E-8
2	1.10 E-6	1.74 E-6
3	3.45 E-6	7.52 E-6
4	6.82 E-6	1.37 E-5
5	5.45 E-5	1.23 E-4
6	9.23 E-5	4.52 E-4
7	1.90 E-3	5.40 E-3
8	2.30 E-3	5.60 E-3

7.6 Effects of Water Uptake on Mechanical Properties

Tensile stress–strain tests were carried out on two sets of M25 composite samples prepared by shear mixing in order to study the effects of water absorption on mechanical properties such as Young's Modulus (*E*), tensile strength (σ_t) and elongation at break (ε_t). One set samples were water saturated, while the other set was heated to remove the absorbed water (60 °C, vacuum for 10 days) from water-saturated specimens. The reference data is from previous mechanical test of composite samples fabricated by shear mixing. The resulting data of samples are listed in Table 7.5, and corresponding curves are plotted in Figure 7.7.

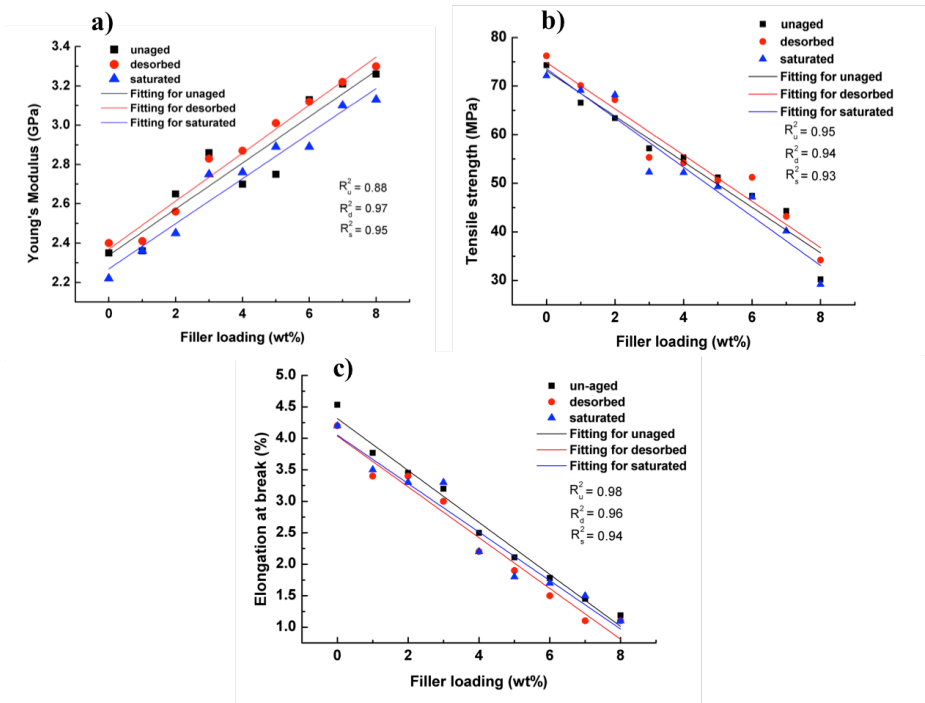

Figure 7.7 Young's modulus (a), tensile strength (b) and elongation at break (c) as function of GNP loadings of unaged, water-saturated and water-desorbed M25 composite samples.

It is found that the Young's modulus of water desorbed samples did not change significantly compared to the un-aged samples in Table 5.2. However, for the water saturated samples, *E* drops slightly, which may be attributed to the plasticization effects of absorbed water molecule forming hydrogen bonds with remainder hydroxyl groups and weakening them [12]. After having been aged for more than two months, the drop of *E* is relatively small when compared with

literature [1, 5], which is associated with a change in the mechanism of water absorption [13-14]. It is said that at the initial stage, the absorbed water linked with the epoxy matrix through van der Waals forces and hydrogen bonds, weakening the original bonds and increasing the segmental mobility. This water is named Type I bound water (only bound by one hydrogen bond), which usually is accompanied by reduction in T_g, tensile strength and elastic modulus of the materials. After long-term aging in the water bath, samples are water saturated and Type II bound water is formed from Type I bound water. Namely, water molecules begin to form multiple chemical connections with matrix groups (Type II). Type II bound water, unlike type I, will act as an enhancement for mechanical properties due to its multiple bonds. It promotes an increase of secondary crosslinking with hydrophilic groups of epoxy resin, such as hydroxyls and amines, leading to recovery of mechanical performance, which is beneficial for its application in hydrothermal environment.

Table 7.5 Mechanical properties of epoxy and composites after water absorption.

Filler loading (%)	**Water saturated**			**Water desorbed**		
	E (GPa)	$\sigma_{t\ (MPa)}$	$\varepsilon_{t\ (\%)}$	*E (GPa)*	$\sigma_{t\ (MPa)}$	$\varepsilon_{t\ (\%)}$
0	2.2 ± 0.1	72.1 ± 4.1	4.2 ± 0.5	2.4 ± 0.1	76.2 ± 5.1	4.2 ± 0.3
1	2.4 ± 0.2	69.1 ± 4.3	3.5 ± 0.6	2.4 ± 0.1	70.1 ± 6.1	3.4 ± 0.5
2	2.5 ± 0.2	68.2 ± 5.6	3.3 ± 0.3	2.6 ± 0.2	67.2 ± 3.4	3.4 ± 0.3
3	2.8 ± 0.2	52.3 ± 3.2	3.3 ± 0.2	2.8 ± 0.3	55.3 ± 4.5	3.0 ± 0.6
4	2.8 ± 0.2	52.2 ± 3.2	2.2± 0.4	2.9 ± 0.3	54.2 ± 5.3	2.2 ± 0.4
5	2.9 ± 0.2	49.3 ± 3.5	1.8 ± 0.3	3.0 ± 0.1	50.6 ± 5.6	1.9 ± 0.2
6	2.9 ± 0.2	47.2 ± 5.2	1.7 ± 0.5	3.1 ± 0.2	51.2 ± 3.2	1.5 ± 0.4
7	3.1 ± 0.3	40.2 ± 6.1	1.5 ± 0.6	3.2 ± 0.2	43.2 ± 4.2	1.1 ± 0.5
8	3.1 ± 0.2	29.2 ± 4.3	1.1 ± 0.7	3.3 ± 0.3	34.2 ± 4.1	1.1 ± 0.4

The elongation at break and tensile strength of water saturated and desorbed samples decrease slightly due to the plasticization effects and swelling caused by water absorption.

7.7 Summary

Water uptake behaviour of neat epoxy and M25/epoxy composites prepared by shear mixing has been studied. During the initial stage, water diffusion follows Fickian diffusion and the diffusion coefficient (D) was calculated. D is found to reduce with increasing filler loadings due to the tortuous path formed by the GNP. However, the maximum water absorption was found to increase with GNP content, which is associated with the voids induced by GNP aggregation as filler concentration increased.

Mechanical and dynamic mechanical properties significantly decreased with water uptake due to plasticization and swelling effects. Electrical properties were also reduced upon plasticization. However, the thermal conductivity was enhanced, which is attributed to water's better thermal properties than the epoxy matrix.

References

1. Nogueira, P.; Ramírez, C.; Torres, A.; Abad, M. J.; Cano, J.; López, J.; López-Bueno, I.; Barral, L., Effect of water sorption on the structure and mechanical properties of an epoxy resin system. *Journal of Applied Polymer Science* **2001,** *80* (1), 71-80.
2. Zhou, J.; Lucas, J. P., Hygrothermal effects of epoxy resin. Part II: variations of glass transition temperature. *Polymer* **1999,** *40* (20), 5513-5522.
3. Cabanelas, J. C.; Prolongo, S. G.; Serrano, B.; Bravo, J.; Baselga, J., Water absorption in polyaminosiloxane-epoxy thermosetting polymers. *Journal of Materials Processing Technology* **2003,** *143–144*, 311-315.
4. Xiao, G. Z.; Shanahan, M. E. R., Swelling of DGEBA/DDA epoxy resin during hygrothermal ageing. *Polymer* **1998,** *39* (14), 3253-3260.
5. Kotrotsos, A.; Vavouliotis, A.; Tsantzalis, S.; Kostopoulos, V., Effect of CNT modified matrix of epoxy CFRPs on hydrothermal behaviour of material. Evaluation of water uptake using electrical resistance

measurements. *Plastics, Rubber and Composites* **2014,** *43* (4), 122-129.

6. Loos, A. C.; Springer, G. S., Moisture Absorption of Graphite-Epoxy Composites Immersed in Liquids and in Humid Air. *Journal of Composite Materials* **1979,** *13* (2), 131-147.
7. Mazor, A.; Broutman, L. J.; Eckstein, B. H., Effect of long-term water exposure on properties of carbon and graphite fiber reinforced epoxies. *Polymer Engineering & Science* **1978,** *18* (5), 341-349.
8. Prolongo, S. G.; Gude, M. R.; Ureña, A., Water uptake of epoxy composites reinforced with carbon nanofillers. *Composites Part A: Applied Science and Manufacturing* **2012,** *43* (12), 2169-2175.
9. Prolongo, S. G.; Gude, M. R.; Urena, A., Synthesis and characterisation of epoxy resins reinforced with carbon nanotubes and nanofibers. *J Nanosci Nanotechnol* **2009,** *9* (10), 6181-7.
10. Prolongo, S. G.; Gude, M. R.; Ureña, A., Improving the flexural and thermomechanical properties of amino-functionalized carbon nanotube/epoxy composites by using a pre-curing treatment. *Composites Science and Technology* **2011,** *71* (5), 765-771.
11. Ivanova, K. I.; Pethrick, R. A.; Affrossman, S., Investigation of hydrothermal ageing of a filled rubber toughened epoxy resin using dynamic mechanical thermal analysis and dielectric spectroscopy. *Polymer* **2000,** *41* (18), 6787-6796.
12. John, S. J.; Kinloch, A. J.; Matthews, F. L., Measuring and Predicting the Durability of Bonded Carbon-Fiber Epoxy Composite Joints. *Composites* **1991,** *22* (2), 121-127.
13. Carter, H. G.; Kibler, K. G., Langmuir-Type Model for Anomalous Moisture Diffusion in Composite Resins. *Journal of Composite Materials* **1978,** *12* (Apr), 118-131.
14. Popineau, S.; Rondeau-Mouro, C.; Sulpice-Gaillet, C.; Shanahan, M. E. R., Free/bound water absorption in an epoxy adhesive. *Polymer* **2005,** *46* (24), 10733-10740.

CHAPTER 8 CONCLUSIONS AND FUTURE WORK

8.1 Conclusions

- Dispersion and orientation of GNPs in shear mixed samples

XRD shows that the GNP in the matrix was still in its original state and hasn't exfoliated even when fabricated by solvent-assisted compounding. Rheology test demonstrated that the resin viscosity increased by almost four orders of magnitude rising from the neat epoxy to the 8 wt.% loading composites, with the 8 wt.% sample showing some elastic behaviour. Optical microscopy and SEM images indicate that the GNP starts to aggregate at loadings > 2 wt.%, and severe aggregation and poor interaction between GNP and matrix were observed, which significantly reduces the aspect ratio and has a great impact on the mechanical properties.

Also four types of GNP aggregates have been formed in composites and have various stress-transfer efficiency. Polarised Raman spectroscopy of M25/ epoxy composites showed that I_G is independent of θ_Z and θ_X, whether the direction of laser propagation is parallel to the Z-axis or X-axis, indicating that there is no preferred orientation for GNPs in epoxy matrix, which was confirmed by the same values of electrical conductivity along different directions.

- Mechanical properties of shear mixed samples

The 2D band in M25/ epoxy composites shows no apparent shift in the Raman spectra upon deformation of the sample, with an apparent random scatter in the 2D band's position, meaning the load transfer between enhancement and matrix is quite poor. The reason would be the weak interfacial adhesion and slippage between graphene layers in the GNP stacks.

After adding M5 and M25 GNPs, T_g drops slightly after initial incorporation, which is attributed to the uneven distribution of the hardener caused by GNP aggregations, affecting the extent of cure, and consequently

lowers T_g. T_g then increases on further GNP addition due to the pin effects of GNP aggregates.

The elastic modulus increased almost linearly with incorporation of GNPs, for both M5 and M25 epoxy composites. While the tensile strength and elongation at break drop significantly, partially due to severe aggregation of the GNPs and poor interfacial adhesion. Halpin-Tsai model for 3D randomly dispersed fits well with experimental data, confirming the GNP's non-preferred orientation. Overall, M25/epoxy composites have slightly better performance over that of M5, due possibly to its higher aspect ratio.

- Thermal conductivity of shear mixed samples

Both the M5 and M25 composite samples had an almost linear increase in thermal conductivity with GNP loading. The biggest improvement was achieved by solvent-assisted mixed M25/epoxy sample at 8 wt.% loading, with thermal conductivity enhanced from 0.20 W $m^{-1}K^{-1}$ (neat epoxy) to 0.76 W $m^{-1}K^{-1}$. Considering the high thermal conductivity of GNP, the improvement seems relatively poor, mainly attributed to the poor thermal coupling of the GNP with the polymer matrix leading to a high interfacial thermal resistance, and high interfacial phonon scattering caused by high surface area of GNP. No obvious percolation threshold was observed on thermal conductivity.

- Electrical conductivity of shear mixed samples

Percolation thresholds of M5 and M25/epoxy composites were 1.5 wt.% and 1 wt.% respectively. M25 has higher aspect ratio, which enables it to form a connected GNP distribution more efficiently than M5. According to Nyquist line diagram, an equivalent circuit was proposed containing a serial arrangement of two units that represent the contribution from the bulk composite sample and the contact region of the interface between the silver paint and the sample. Each unit is depicted by a combination of two possible electrical current components, (i) a resistor (R) and a capacitor (C) or (ii) a resistor and a constant phase element (CPE) in parallel. Fitting results show resistance of bulk composite drops significantly at percolation limit.

- Effects of preparation methods on composite properties

Solvent compounded samples achieved the lowest electrical percolation (0.5 wt.%) in this project, relating to its relatively uniform GNP distribution assisted by the solvent. In addition, the mechanical performance was also superior to that of the other two methods. The percolation thresholds for three-roll mill mixed and shear mixed M25 samples were 2 wt.% and 1 wt.% respectively. In terms of mechanical properties, there is no big difference between these two fabrication routes.

- Water uptake and its effects on composite performance

Diffusion coefficient of composites decreased greatly with increasing loading. This significant decrease of diffusion coefficient could be attributed to the high surface area of M25, which leads to greater barrier effects in the epoxy matrix, forming tortuous paths to hinder water diffusion and decreasing the diffusion rate. On the other hand, the maximum water absorbed goes through an opposite behaviour due to the formation of holes and cracks along GNP aggregates. With increase of GNP loading, the water taken by holes and cracks becomes increasingly high, indicating more aggregates have formed, consistent with SEM observation.

DMTA results show the tan δ curve peak of water-saturated samples is split into two peaks due to another interface formed by water and matrix. Water saturated samples show a slight drop in T_g compared with water-desorbed samples associated with water plasticizing effects. Thermal conductivity increases moderately, while electrical and mechanical properties are compromised by water absorption. The swelling effect of epoxy induced by water absorption expands the distance between conductive GNPs, leading to increasing electrical resistance.

8.2 Suggestions for Future Work

- **Preparation of composites with aligned fillers to improve thermal and mechanical properties**

  Halpin-Tsai model shows that composites with 2D filler alignment give better mechanical properties. Therefore, it would be interesting to fabricate composites with aligned fillers by hot pressing or applying electrical field to study the changes of thermal and mechanical properties.

- **Effects of processing parameters on the structure and properties**

  Due to the great effects of preparation methods on composite properties, it is necessary to control one processing parameter of shear mixing and solvent-assisted compounding, like rotating rate, mixing temperature, solvent type, to study their influence on structure and properties of composites.

- **Raman mapping to determine the distribution of fillers in epoxy resin matrix**

  In this work, only SEM has been carried out for filler dispersion in composites, which is focusing on a relatively small area. Raman mapping could measure a much lager area to give information of GNP fillers in epoxy composites and help to study the relationships between filler dispersion and composite properties.